

Studies beyond the neutron dripline using Quasifree (p,2p) reactions: The case of ^{13}Be

Estudios más allá de la línea de goteo de neutrones usando reacciones (p,2p) cuasi-libres: El caso del ^{13}Be

Guillermo Ribeiro Jiménez

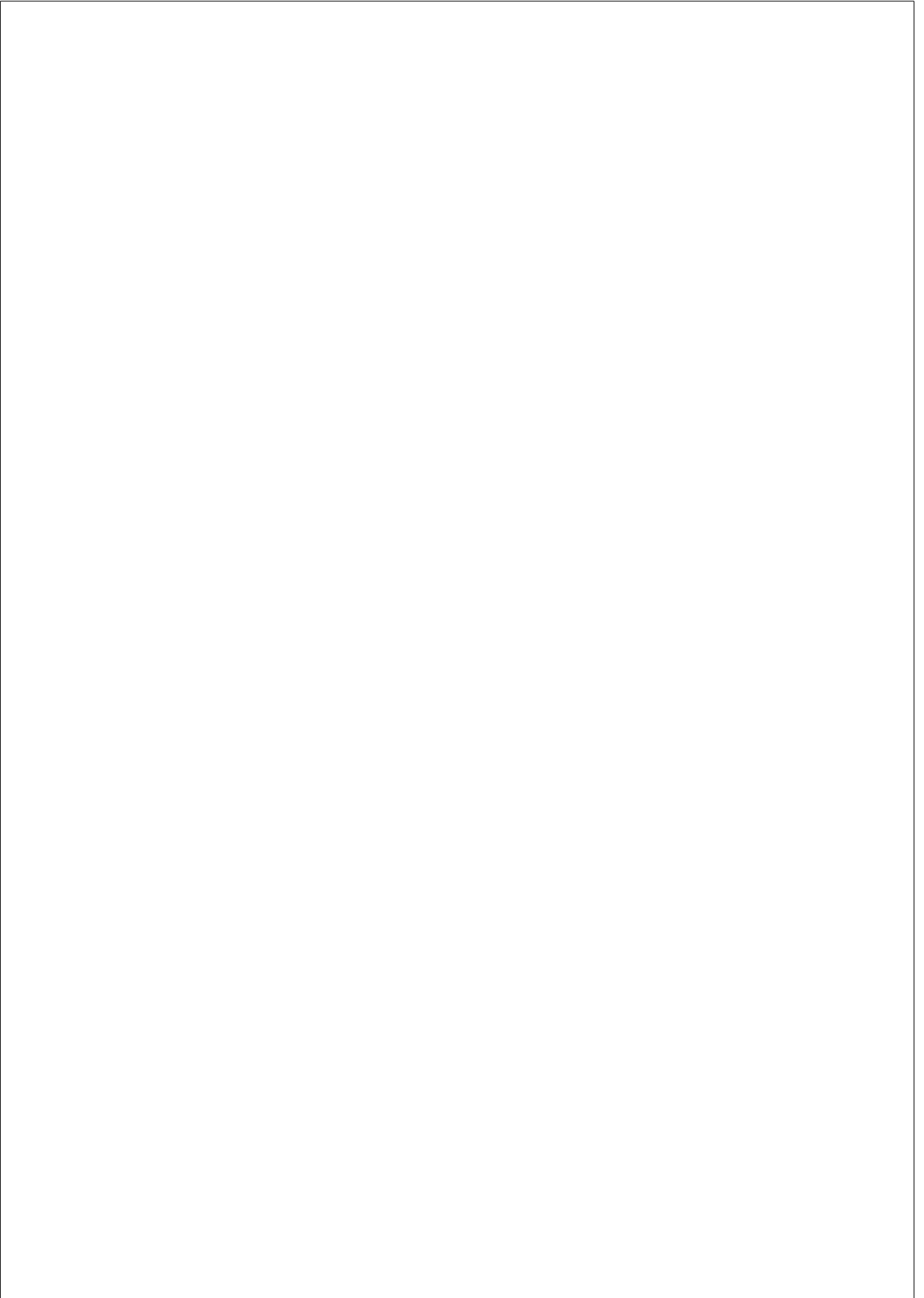
TESIS PRESENTADA PARA LA OBTENCIÓN DEL
TÍTULO DE DOCTOR EN FÍSICA POR LA U.C.M.

Junio 2015

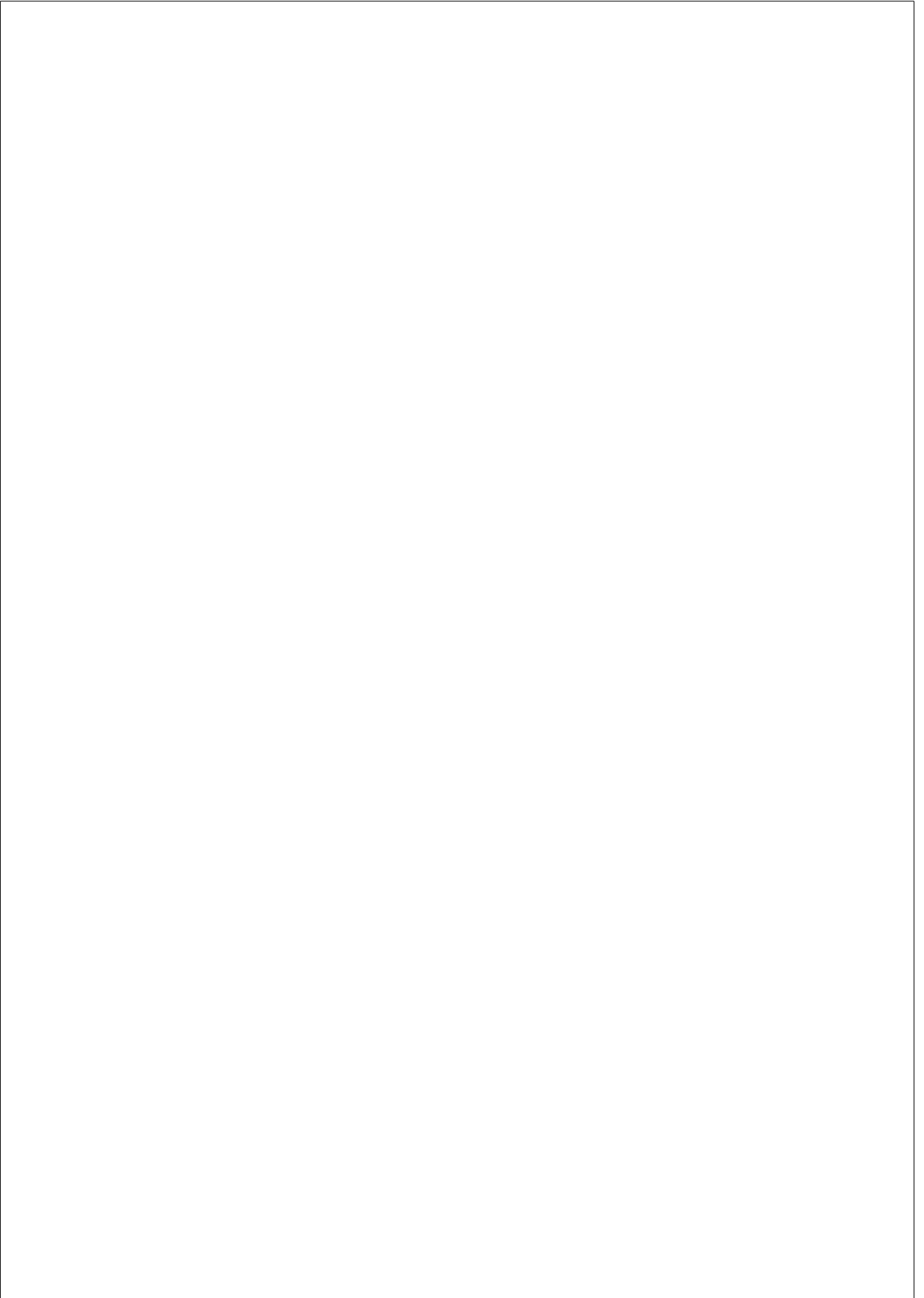
Directores:

Profesor Olof Tengblad
Instituto de Estructura de la Materia(CSIC)

Doctor Enrique Nácher González
Instituto de Estructura de la Materia(CSIC)



A mis padres, Jose y Rocío.



Contents

Contents	i
List of figures	v
List of tables	ix
Acknowledgements	xi
1 Introduction	1
1.1 The Nuclear Physics through a telescope	1
1.2 Going from the stability line to the dripline	4
1.3 The dripline fauna: Halos and unbound nuclei	7
1.3.1 Halos	7
1.3.2 Unbound nuclei	10
1.3.3 ^{13}Be	11
1.3.4 Resonances or quasi-stationary states.	14
1.4 Direct Reactions: Knockout	15
1.4.1 Quasifree scattering	17
2 Experiment & Detector setup	19
2.1 The experiment	19
2.2 GSI Helmholtzzentrum für Schwerionen-forschung GmbH	19
2.2.1 Ion sources	21
2.2.2 UNILAC	22
2.2.3 SIS(SchwerIonenSynchrotron) 18	22
2.2.4 FRS	22
2.3 Cave C: R3B Setup	25
2.3.1 Incoming beam detectors	25
2.3.2 Around the target detectors	28
2.3.3 Outgoing fragment detectors	32

CONTENTS

3	Detector calibrations	37
3.1	Introduction to Land02	37
3.2	General remarks about calibrating with land02	40
3.3	Triggers	40
3.4	Raw → TCAL	42
3.5	Incoming beam identification calibration	43
3.6	Calibration of the detectors around the target	45
3.6.1	Double Sided Silicon Strip Detectors (DSSDs)	45
3.6.2	Crystal Ball (XB)	47
3.7	Calibration of the outgoing fragments detectors	51
3.7.1	Fiber Detectors (GFI)	51
3.7.2	Time-of-Flight-Walls (TFW)	53
3.7.3	LAND	54
3.8	Tracker	55
4	Analysis	57
4.1	Incoming isotope identification	57
4.2	Detector alignment	58
4.3	Fragment and neutron selection	59
4.4	Invariant mass and relative energy	61
4.5	Breit-Wigner fit	65
4.6	Detection of ^{12}Be gamma rays	67
4.7	Looking at the protons of the (p,2p) reaction	71
5	Results & Discussion	75
5.1	Preliminaries	75
5.1.1	Folding	76
5.1.2	Non Resonant Background	77
5.2	Results	78
5.2.1	Initial parameters	78
5.2.2	Considering two resonances	80
5.2.3	Considering three resonances	82
5.2.4	Considering Quasifree Scattering	87
5.3	Discussion	90
5.4	Conclusions	95
5.5	Future prospects	95
	Appendix A Error calculations	97

CONTENTS

Appendix B Summary	99
B.1 Introduction	99
B.2 Experimental setup	100
B.3 Analysis method	102
B.4 Results	104
B.4.1 Considering two resonances	104
B.4.2 Considering three resonances	106
B.4.3 Considering Quasifree Scattering	108
B.5 Discussion	109
B.6 Conclusions	112
B.7 Future prospects	112
Appendix C Resumen en castellano	115
C.1 Introducción	115
C.2 Montaje experimental	116
C.3 Métodos de análisis	118
C.4 Resultados	121
C.4.1 Considerando dos resonancias	121
C.4.2 Considerando tres resonancias	122
C.4.3 Considerando reacción (p,2p) de dispersión cuasi-libre	124
C.5 Discusión	125
C.6 Conclusiones	128
C.7 Desarrollos futuros	129
Bibliography	131

CONTENTS

List of Figures

1.1	Thomson and Rutherford atomic model	2
1.2	Production Methods	5
1.3	Nuclear chart	6
1.4	Nuclear chart zoomed to the light neutron-rich nuclei area	7
1.5	Comparison of nuclear radii	8
1.6	Halo nucleus ^{11}Li size comparison	9
1.7	^{13}Be Relative energy from Kondo et al	12
1.8	^{13}Be Relative energy from Aksyutina et al	13
1.9	^{13}Be Relative energy from Randisi et al	14
1.10	Wavefunction internal and external region and the resonance case	15
1.11	Knockout scheme	17
1.12	Quasifree scattering signatures	18
2.1	GSI Facility	20
2.2	Ion Sources	21
2.3	Scheme of the UNILAC	21
2.4	FRS overview	23
2.5	R3B Setup overview	24
2.6	Schematic view of POS	26
2.7	Scheme of the ROLU	26
2.8	Schematic view of the PSP	27
2.9	Target wheel	28
2.10	DSSD around the target wheel	29
2.11	Picture of one Micro-Strip Double Sided Silicon Detector(DSSD)	30
2.12	Crystal ball picture	31
2.13	Schematic view of the GFI	33
2.14	TFW picture	34
2.15	Scheme of the TFW paddles	35
2.16	Scheme of LAND	36
2.17	Scheme and picture of LAND paddles	36

LIST OF FIGURES

3.1	Land02 Data levels flow chart	39
3.2	Pedestal subtraction example	42
3.3	Time calibration plot	43
3.4	RAW PSP energy loss in the cathode	43
3.5	Example of IDentification figure	45
3.6	DSSD η calibration	47
3.7	Source peaks for XB Calibration	48
3.8	Linear calibration fit for XB	49
3.9	XB Slope vs angles	49
3.10	Addback algorithm	50
3.11	GFI charge distribution	52
3.12	Result of the gainmatching for GFI	52
3.13	GFI Correlations	53
3.14	Energy in the TFW	54
3.15	LAND Velocity calibration	55
4.1	Fragment Identification for the analysis	58
4.2	Charge identification	60
4.3	Tracked mass spectrum	61
4.4	Fragment-neutron angular distribution	63
4.5	Neutron β	64
4.6	Fragment β	64
4.7	^{12}Be +neutron Relative energy spectrum	65
4.8	Crystal Ball gamma spectrum of the ^{13}Be	67
4.9	^{12}Be energy levels structure	68
4.10	Gamma ray spectrum after background subtraction	69
4.11	^{13}Be Relative energy gated on the gamma ray	70
4.12	^{13}Be Relative energy spectrum after subtracting uncorrelated events	70
4.13	Four (p, 2p) angular distribution	72
4.14	Four (p, 2p) angular distribution non including one neutron in LAND	73
5.1	Channel Radius comparison	76
5.2	Folding σ function	77
5.3	Non-Resonant background fitted to get parameters $A_{2,3}$	78
5.4	Single fits to each three resonances with $l=0,2$	79
5.5	Visualization of the fit considering two resonances $l=0,2$ without Non resonant background	80
5.6	Visualization of the fit considering two resonances $l=0,2$ with Non resonant background	82
5.7	Visualization of the fit considering three resonances with $l=0,0,2$ and without Non Resonant background	83

LIST OF FIGURES

5.8	Visualization of the fit considering three resonances with $l=0,2,2$ and without Non Resonant background	84
5.9	Visualization of the fit considering three resonances with $l=0,0,2$ and with Non Resonant background	85
5.10	Visualization of the fit considering three resonances of $l=0,2,2$ and with Non-Resonant background	86
5.11	Visualization of the fit considering three resonances with $l=0,0,2$ in coincidence with QFS scattering	88
5.12	Visualization of the fit with $l=0,2,2$ in coincidence with QFS scattering	89
5.13	Comparison with important previous results	91
5.14	^{13}Be structure proposed by this work	94
A.1	$\beta_{fragment}$ distribution inside the target	98
A.2	Relative energy error calculation	98
B.1	Summary: Schematic view of the S393 setup	101
B.2	Summary: ^{13}Be Relative energy spectrum after subtracting uncorrelated events	104
B.3	Summary: Visualization of the fits considering two resonances	105
B.4	Summary: Visualization of the fits considering three resonances	107
B.5	Summary: Visualization of the fit considering three resonances with QFS conditions	108
B.6	^{13}Be structure proposed by this work	111
C.1	Resumen: Esquema del montaje experimental del experimento S393	117
C.2	Resumen: Espectro de energía relativa del ^{13}Be tras sustracción	120
C.3	Resumen: Ajustes considerando dos resonancias	122
C.4	Resumen: Visualización del ajuste considerando tres resonancias	123
C.5	Resumen: Visualización del ajuste considerando tres resonancias con condiciones de DCL	125
C.6	Resumen: Estructura del ^{13}Be propuesta por este trabajo.	128

LIST OF FIGURES

List of Tables

3.1	Trigger table	41
3.2	Calibration sources	48
5.1	Table of results considering two resonances without Non Resonant Background and $l=0,2$	81
5.2	Table of results considering two resonances with Non Resonant Background and $l=0,2$	81
5.3	Table of results considering three resonances with $l=0,0,2$ and without Non-Resonant Background	83
5.4	Table of results considering three resonances with $l=0,2,2$ and without Non-Resonant Background	84
5.5	Table of results considering three resonances with Non-Resonant Background and $l=0,0,2$	85
5.6	Table of results considering three resonances with Non-Resonant Background and $l=0,2,2$	86
5.7	Table of fit results in coincidence with QFS using three resonances and $l=0,0,2$	88
5.8	Table of results of the fit in coincidence with QFS using three resonances and $l=0,2,2$	90
B.1	Summary: Table of results considering two resonances	105
B.2	Summary: Table of results considering three resonances	106
B.3	Summary: Table of results considering three resonances with QFS conditions	109
C.1	Resumen: Tabla de resultados del ajuste considerando dos resonancias	122
C.2	Resumen: Tabla de resultados del ajuste considerando tres resonancias	124
C.3	Resumen: Tabla de resultados considerando tres resonancias con condiciones DCL.	126

LIST OF TABLES

Acknowledgements/Agradecimientos

Son las 3 de la madrugada del día 4 de Mayo de 2015, apunto la fecha porque estoy seguro de que querré recordarla, hoy a una hora razonable, entrego *la tesis*. Parece que fue ayer cuando entré en el grupo de Física Nuclear Experimental del IEM-CSIC, pero no, he estado trabajando ahí desde el 1 de Septiembre de 2010, es decir, casi cinco años. Este texto es la conclusión de varios años de trabajo, aprendizaje, buenos y malos ratos, cambios y muchos viajes. Muy poco de lo que ha sido este tiempo está realmente condensando en este documento, sólo se refleja una parte. De entre todas las cosas que se podrían quedar fuera hay una en concreto que no debe hacerlo: Las personas que me han ayudado, que son muchas. Que menos que dedicar un rato a agradecerlo.

It is 3 in the morning of May 4, 2015, I write down the date because I am sure I will want to remember, today at a reasonable hour, I am handing in *the thesis*. It seems like yesterday when I started at the group of Experimental Nuclear Physics IEM-CSIC, but I have been working there since September 1, 2010, almost five years. This text is the conclusion of several years of work, learning, good and bad times, changes, and many travels. Very little of what has been this time is actually condensed in this document, only a portion is reflected. Of all the things that could be left out there is one in particular that should not: People who have helped me, which are many. This is time to be grateful.

La primera persona a la que tengo que agradecerle su contribución, es sin duda, mi director de tesis, Olof Tengblad. Desde el momento en que me escogiste para la beca FPI, hasta el último e-mail con correcciones sobre la tesis (aunque siempre sean parcos en palabras), por todas la discusiones que acaban bien y por supuesto por toda la oportunidad, los consejos y las historias. También estoy muy agradecido a María Jose y a Andrea, por ayudarme siempre que lo he necesitado.

Por supuesto, una de las mejores cosas que me han dado estos años en la física nuclear es conocer a los que han sido todos mis compañeros en el grupo, ahora amigos, sin los que estos años valdrían bastante menos.

A Kike, por haber sido un amigo además de un director de tesis, por responder siempre a cualquier problema y poder hablar contigo de cualquier cosa. A Mariano, por toda la ayuda que has sido, tanto en lo personal como en lo profesional, por las gilipolleces que me dijiste el día de la fiesta de la cerveza y por supuesto, por las discusiones, tan inacabables como inmejorables. A Vicente, por hablar de todo y no cortarte un pelo (sobretudo del bigote) y por las discusiones inmejorables (pero acabables). A Briz, por el buen rollo SIEMPRE y por los triples. A Andrés, por todo el azúcar, por ayudar siempre que puede y por Gallagher y Jäckel. A Jose, por ser el primero en echarme una mano ahí en GSI en 2010, por que una noche (o un día) contigo es una montaña rusa y por que pidas los cafés. A Riccardo, por ser la alegría del grupo durante mucho tiempo y por supuesto también por las discusiones. A Alejandro porque parece que llevas con nosotros desde que empecé y eso es difícil. A Jan, por aguantar nuestras discusiones en castellano y ser siempre un gran tío. A Ángel, por todas las discusiones en los viajes, impagables y tener siempre otro punto de vista. A Mario, por aquel ron en tu casa, por tu vehemencia y por estar algo en la parra. A Irene, por venir con tanta energía. A Jorge, por los FIFA y haberme acogido siempre genial en Darmstadt. A Ana, porque fue una pena que sólo estuvieras un año aquí, por el buenísimo tequila que nos diste, y por el experimento del CERN, que en el fondo lo pasamos bien. A Carlos y a Ricardo, por ser los primeros en echarme una mano en todo cuando entré en el grupo.

These last years have involved a lot of traveling and people from GSI, Santiago, Chalmers, Aarhus and plenty of other places have been a major support, help and fun.

I have to be very grateful to the people of Chalmers and Göteborg which spent their time helping me in my first long-time staying abroad. Anna for helping so much with the renting and living, Björn, Göran, Ronja and Andreas for their help with the physics, Håkan for the same and the pizzas and specially Thomas for everything. I would like also to say thank you to Jim, for all the talks and beers.

I also spent three intense months at GSI, Darmstadt. There were so many people that I will forget some of them for sure, thank you all in advance. First I have to say thank you to Tom, Konstanze and Haik, for always helping a lot when I have been able to find them, to Ralf, for the same and answering my annoying e-mails, to Valerii for the travels, the beers, the discussions and the strange Ukrainian tale that you told me at Dresden, to Igor for the beers and the talks, to all the other guys like Christoph, Felix, Alina, Leyla, Dominic, Togano or Sebastian for the coffees and all the good times. I have to be specially grateful to my office mates at GSI for welcoming me so easily, being friends and for the gummy bears, thanks Phillip for the fun, the discussions and being with me in the cave my first month there, thanks Marcel for all the trips, the strange stories and the barbecues, thanks Matthias for ALWAYS helping, the fun and for always have good conversations. I cannot avoid to mention my Steinhaus colleague those months, Antonio, for all the fun too.

There is also a lot of people from the R3B Collaboration that I have to men-

tion here. Like before I will probably forget a lot of them, I am sorry, not be mad to me! This work would have been very much harder without Paloma, which helped more than anyone when I started, thank you for that and for all the other talks(Dexter obviously) and good times. Thanks to Magdalena for all the time at Darmstadt, trying to help each other and having fun. Thanks to Tobi for the beers and thanks to Lola, Hector, Dani, Matthew, Simon, Ana and Paulo for always being nice and helpful.

From Aarhus I have to be specially grateful to Karsten, for taking very seriously helping me, the jokes and all the interesting discussions. Thanks to Oliver,Jonas, Gunvor, Kasper, Morten, Hans, Oleksandr, Aksel and Dmitry for discussions, beers, and all my time there.

There are other people from elsewhere that I also need to mention without any special order. AJ for the really good time and beers at Berkeley, Diego for being tireless at Zakopane. I have to give very special thanks to Nara Singh for being always so nice and helpful with me. Thank you to Franco for the great times in Madrid. To Carlos for the good time at Italy. A Bruno, Jacobo y Lay, por todos los buenos ratos.

Hay mucha gente de Madrid (bueno, muchos ya no son de aquí), a los que quiero agradecer estos años de apoyo, diversión y de aguantarme.

Quiero empezar agradeciendo su contribución a mis tres compañeros *originales* de piso y amigos, puesto que no puedo separar mis inicios en la física nuclear con entrar con ellos en La Mansión en Diciembre 2011. Gracias a los tres por animaros a dar el salto. Gracias a Álvaro, por intentar ser comprensivo, por salir de la ducha y por el viaje a EEUU, increíble. Gracias a Pablo por los 2K, por los FIFA y sobretodo porque gracias a la casa volvemos a ser muy buenos amigos. Gracias a Toni por aguantarme cosas, por no morirse por su intestino, por el viaje a Alemania y por las cervezas siempre.

Los compañeros de piso se han cambiado por otros y ya hace más de un año de eso! Muchas gracias a los dos por imponer las cenas comunes, de lo mejor que le ha pasado al piso. A Alvarito por haber estado siempre disponible, por los juegos a medias, por que hay pan con hostias y queda poco pan, por tantos años. A Tati por animar el cotarro, por intentar ser siempre la alegría en el día a día, que al menos para mi, es imposible, por la fruta gratis y sobretodo por las inexistentes paellas.

A Rorro, por ser amigo desde siempre en todas partes, por haber estado cuando lo he necesitado, por todas las charlas de absolutamente cualquier cosa, por la ansiedad y por que viajes algo menos y nos veamos más. A Javi, por todos los años de la carrera y muchos más, por venir a Gothenburg y a Suiza, por ser comprensivo, por las discusiones y por los personajes chungos de rol. A Gabo, porque montamos un equipo juntos, por dejarme participar tanto en la boda(y a Haizea), que fue genial, por que aunque hablemos poco, al final sacamos un rato. A Edu por hablar de cosas raras, porque cuando vienes parece que no ha pasado el tiempo, por la ayuda con la física hace años y mira ahora y porque feliz navidad. A Toño por el

oso maloso, por acogerme en San Francisco y porque le he echado mucho de menos estos años. A Paula porque se duerme y haberme ayudado siempre que se lo he pedido. A Susana porque siempre quiere salir y que la liemos y porque estemos de acuerdo a donde. A Inés por el cariño y por llegar tarde. A Lara por que quiero verla más días que en nuestro cumple. A Javi por la gran acogida en Londres y por los años buenos incluso antes de que yo llegase a Pozuelo.

A María, porque siempre ha estado ahí a pesar de todo, por la sal, los buenos ratos y el teatro. A Santi y Auro porque es difícil separarlos, por Sherlock Holmes, por la comida India, por las charlas en serio y por el oso panda que me ha acompañado en este último tramo de escritura. A Emilio por haberme echado una mano a retomar el rol, por los cochinitos y por las charlas molonas. A Isa por ser inescrutable y por lo del CERN. A Artemi y a Ali por tantos años. A Joserra, por seguir ahí y por todas las charlas.

A Jorge-Cels, por los emails largos geniales derrepente y por que deberíamos hablar más.

No quiero olvidarme de agradecer la contribución de Javier Coronas, Javier Cansado y Pepe Colubi que con mi reciente descubrimiento de *Ilustres Ignorantes* me han acompañado estos últimos meses de encierro y escritura.

This is a thesis about Nuclear physics, therefore I would like to say thank you to Alexei Ananenko, Valeri Bezpálov and Boris Baranov. They gave it all, saying thanks from here is the least I can do.

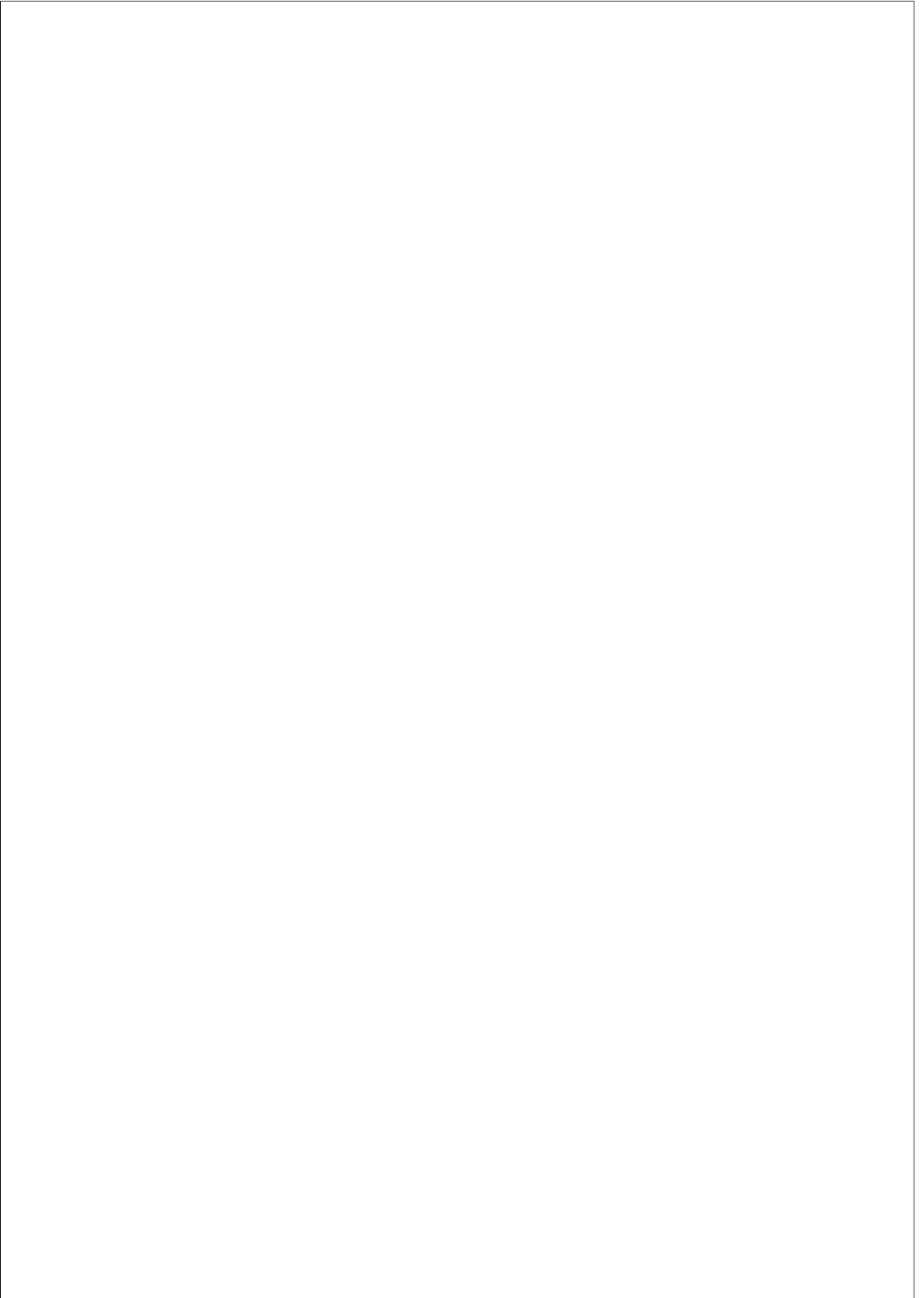
A la caféina, que sin ella tampoco habría podido acabar.

Por supuesto tengo que acabar dando las gracias a toda mi familia, que siempre ha estado conmigo estos años. A mi padre, Jose, por venir siempre a comer al VIPS durante casi cinco años, por ser tan generoso y por enseñarme a ser tan crítico. A mi madre, Rocío, por comprenderme, por todo el cariño y por haber confiado siempre en mí. A Ana y a Luís, por tantas cosas, por las charlas, por el apoyo continuo que tanto se nota y por la comida genial, claro. A Marisa por que siempre me ha apoyado, a David y Julie (y Lea) por esperarme siempre con los brazos abiertos, a los cuatro por el recibimiento en Bruselas en 2012 y por vernos más. A Claire, por las peleas de antaño, por el buen rollo, porque siento mucho no haber ido a Granada y también por vernos más. A Álvaro Y Mariluz, por la ensalada de salsa rosa, por el día 6 de Enero que montáis en vuestra casa y siempre por el afecto. A Julia, María, Inés y Sara, porque ya ninguna sois mis primas pequeñas, por el video, por el buen rollo y para/por lo que queráis. A Ricardo y Paula, por las enormes cenas en su casa, por la moneda esa que me quedé y de la que todavía me acuerdo y por todo el afecto. A Chity y Carmen, por los regalos geniales, y por toda la ayuda cuando la he necesitado. Y no me olvido de Toño, Merche y Diego, que aunque nos veamos mucho menos, les tengo que agradecer muchos años de vacaciones en inmejorable compañía y les echo de menos.

Sólo me queda una persona por agradecer, Natalia, gracias por todo, por la ayuda con algunos dibujos, por las comidas y cenas que he necesitado, por llevarme

en coche, por tanta comprensión, por los silencios, por despreocuparme y por preocuparme y por todo el cariño día a día, que es lo más importante.

Por último, todo este trabajo no habría sido posible sin la ayuda y la necesaria financiación y apoyo del Ministerio de Ciencia e Innovación así como el Ministerio de Economía a través de los proyectos FPA2009-07387 y FPA2012-32443, así como la beca FPI que disfruté entre Septiembre 2010 y Agosto 2014 BES-2010-042262.



“- Algebra forces your mind to solve problems logically. It's one of the only perfect sciences...

- You think the world runs on logic? Come on. Open your eyes”

1x07 Brotherhood, Six Feet Under

1 Introduction

1.1 The Nuclear Physics through a telescope

In the late nineteenth century scientists were looking for new elements to add to the 83 at that time known; 50 of these had only been found in the last hundred years [1]. The atom was defined as the most basic form of matter and every element was regarded as a completely different particle. The elements were classified just following their atomic mass, but Dmitri Mendeleev (1834-1907) noted that certain chemical properties emerged with fixed periodicity which led him to postulate the periodic table in his textbook Principles of Chemistry (1869). In 1815 William Prout (1785-1850) published the hypothesis that all the atomic weights were an integer multiple of the Hydrogen weight, considering it as the basic compound of all the elements. Despite the fact that this idea was very close to reality, it was wrongly discarded as soon as it was obvious that several atoms did not follow that trend. The atom was considered as a particle impossible to break or divide.

The discovery of radioactivity revealed that atoms were not just a simple particle but they were compound of several smaller pieces. In November 1895 Wilhelm Conrad Röntgen discovered the X-rays as a result of the fluorescence produced by cathode rays in a cathode ray tube. Henri Becquerel (1852 - 1908) heard about these results in a conference, and wondered if luminescence was a precondition for the observation of X-rays. He performed several experiments illuminating Uranium salts with sunlight causing the material to glow by phosphorescence, but he ended up realizing that Uranium emits certain rays with similar penetration power to the X-rays naturally without previous exposure to sunlight. This conclusion is the discovery of radioactivity by Becquerel in 1896. Marie Skłodowska-Curie (1867 - 1934) and her husband Pierre Curie (1859 - 1906) thought that these rays might be coming from a new element within the Uranium salts different from the compounds Thorium and Uranium. As a result of their work to isolate the source of the rays they discovered two new elements: Polonium and Radium.

1. Introduction

Ernst Rutherford (1871-1937) would be the man who became the father of Nuclear Physics for his discovery of the atomic nucleus in 1913. He was working at McGill University in Montreal (Canada) when he discovered the alpha (α) and beta (β) radiation [2]. The rays emitted by the Uranium salts had different penetration powers, thus working with different materials to measure the penetration as well as with magnetic fields in order to bend them, led him to discover the difference between two types of rays to which he assigned the Greek letters α and β in 1899. Almost at the same time, Paul Villard (1860-1934) at France studied the emitted radiation from Radium, a different kind of radioactivity more powerful that ended up named by Rutherford in 1903 [3] as gamma (γ) rays. Years later in 1908, Rutherford in collaboration with Thomas Royds (1884-1955) at Manchester (United Kingdom) found that the alpha particles were indeed helium nuclei [4].

In 1901 William Thomson, Lord Kelvin (1824-1907) proposed the first model of the atom structure. It was known as the “Plum pudding model” because it consists in a sphere of positive charge with the electrons embedded like plums in a pudding, where the total charge was cancel out (see figure 1.1). The model was improved by J.J Thomson (1856-1940) in 1904, making the electrons move in concentric circles in the sphere.

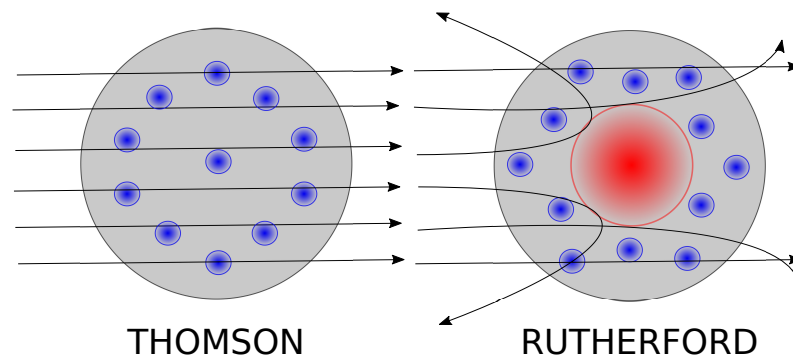


Figure 1.1: Basic atomic model schemes with their expected behaviour against the Geiger and Marsden experiment. *Left:* The “Plum pudding model” of Thomson. The blue dots are electrons within a positive charged sphere-like structure. In such a case, the alpha particles would go through straight, just deflected by a very small degree because of the electric field. *Right:* The Rutherford model, a nucleus with high density and positive charge surrounded by electrons in circular orbits. In such a case, the alpha particles would be scattered strongly whenever they interact with the heavy nucleus, which happens seldom due to the small size of it.

1.1. The Nuclear Physics through a telescope

Rutherford in 1911, in contrast to the Thomson model, postulated that the positive charge was concentrated in the center of system in a very small nucleus, while the electrons were orbiting the nucleus in a similar way of planets orbiting around the Sun [5] (see figure 1.1). His idea was supported by an experiment performed in 1913 [6] by Geiger (1882-1945) and Marsden (1889-1970) where a thin gold foil was hit by alpha particles from a Polonium source. If the Rutherford model was correct, most of the particles must go through the gold foil while some of them would be scattered even to the opposite direction. This contribution started within the science of Physics a new field to study the nucleus inside the atom: Nuclear Physics.

Proposing the existence of the nucleus was not the last important contribution of Rutherford to this new field of science. In 1919 he reported about an experiment where an alpha particle was projected against Nitrogen, one Hydrogen nucleus was knocked out and an Oxygen-17 was produced in the reaction ${}^{14}\text{N} + \alpha \rightarrow {}^{17}\text{O} + {}^1\text{H}$. The obvious conclusion was that the Hydrogen nucleus was a component of the Nitrogen nucleus. Hence this result validated the William Proud hypothesis that the Hydrogen nucleus was the mass unit that form all nuclei. Rutherford named the Hydrogen nucleus, proton.

Rutherford model of the atom was afterwards extended by Bohr and Sommerfeld, solving some of the problems that the atom model had. Still, there was a big problem in the structure of the nucleus, how could that positive charge be held together in such a small area? Rutherford himself proposed another particle composed by an electron and a proton together in 1920. Years later (1932), James Chadwick (1891-1974) found the neutron, a particle with the same mass as the proton but without any charge. This discovery allowed to explain the difference between the mass and the atomic number.

Nevertheless the new particle did not explain why the nucleus was compact and did not break-up due to the Coulomb repulsion, especially in the case of the heavier nuclei. In 1935 Hideki Yukawa (1907-1981) proposed a new force 100 times stronger than the Electromagnetic Force that only acted at very small distances of 10^{-12} cm: The Nuclear Strong Force. He proposed that in the same way the photons are exchanged in the Electromagnetic Force, the strong force exchange a heavy particle called meson with a mass between the proton and the electron. Years later in 1947 the pion (π) meson was found in cosmic ray research, which is the primary force carrier for the nuclei force in atomic nuclei.

In 1933, Enrico Fermi (1901-1954) proposed an explanation to the beta decay, following the previous ideas from Heisenberg presenting this decay as transformation from a neutron to a proton, emitting an electron. This process was better clarified by Fermi, introducing the neutrino (ν_e), in order to conserve the spin within the decay and to explain the continuous energy spectrum of the emitted β particles. A new force, called Weak Force was introduced, 10,000 times weaker than the Electromagnetic force and responsible to keep these particles together before decaying

1. Introduction

by emitting an electron.

The basic foundations of Nuclear Physics appeared at the beginning of the XX century, although they continue to be developed fast through the later years. It was boosted by the funding related to the new energy production opportunities and unfortunately, to the different conflicts of the same century.

1.2 Going from the stability line to the dripline

Since the 1920s a new tool to further study the sub-atomic particle properties has been in constant development: The Particle Accelerators. These devices allow to accelerate charged particles for colliding against another particles or a certain target, in order to produce a nuclear reaction or break up in order to probe the structure of the involved particles and nuclei.

There are two main types of accelerators:

- Electrostatic accelerators, using static electrical fields like the Cockcroft-Walton and Van de Graaff
- Oscillating field accelerators, which use radio frequency electromagnetic fields such as cyclotrons and linacs.

The latter is the main method used by the current large-scale particle accelerators like the LHC or the accelerators at GSI. Throughout the XX century all stable or long-lived isotopes have been accelerated and used in hundreds of experiments. Such a scientific work has allowed developing new applications for these machines like implanting ions for material modification, carbon dating, cancer treatment or medical imaging.

Not many years ago, in the 1980s, new nuclei production methods were developed opening a new landscape of nuclei available to accelerate, therefore giving the opportunity to reach certain isotopes that were out of range before, plenty of unstable nuclei called exotic nuclei close to the limits of the nuclear force.

On the one hand, the first way to reach exotic nuclei is the ISOL method (Isotope Separation On Line). The process start with a previous acceleration of protons or heavy ions which are let to impinge on a thick target where the radioactive nuclei is produced. The produced nuclei diffuse through the thick target held at high temperatures towards the Ion-source, where it is ionized and extracted usually by applying an extraction voltage in the range of 30-60 KV. The outgoing beam is mass-charge selected by a magnet separation, after the process the beam can be further accelerated by injection into a post-acceleration stage or used directly for decay experiments. This method produces high quality beams which are comparable to stable beams, although the most exotic and short-lived isotopes are hard to produce because the extraction time from the ion source can be too long for these nuclei to survive.

1.2. Going from the stability line to the dripline

On the other hand, the In-Flight fragmentation method can produce more exotic isotopes but the beam is worse in energy precision and beam focus as well as purity. In this case a heavy ion is accelerated until the desired velocity, it is let to impinge on a thin target producing a cocktail beam of several ions, which continues with a similar velocity through a magnetic fragment separator for selection before reaching a secondary target where the experiment is performed. This latter method only relies on tagging electronically the bunch of isotopes that reach the experimental hall contrary to the high-purity beams of the ISOL method. A scheme of both methods can be seen in figure 1.2. The first production and identification of relativistic radioactive beams was at Berkeley in 1979 [7][8] using ^{40}Ar and ^{48}Ca as primary beams using the fragmentation method.

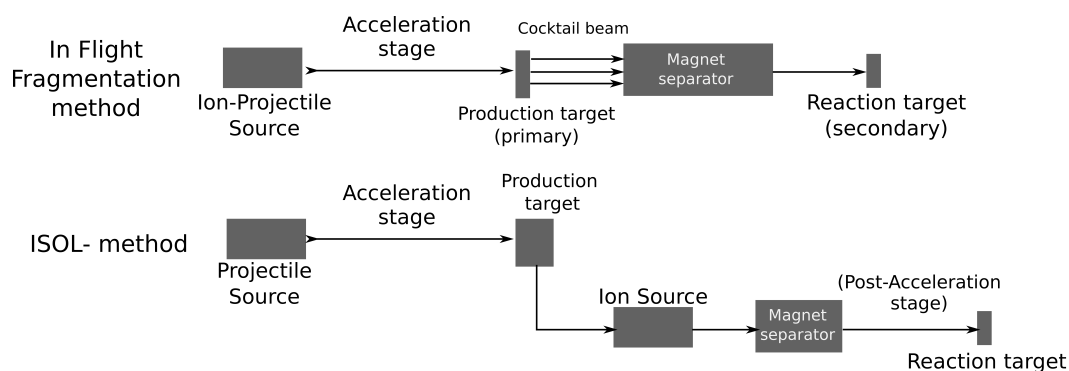


Figure 1.2: ISOL and In-Flight fragmentation method to produce exotic nuclei in particle accelerators. The ISOL method pre-accelerates a light ion that is shot to a thick target, producing a bunch of radioactive nuclei that continue towards the ion source. After the isotope of interest is extracted from the source, it goes through an electromagnetic separator delivering it directly to decay experiments or to second acceleration. The In-Flight fragmentation method accelerates a beam of heavy nuclei and makes it collide with a light target to produce a cocktail beam. The process ends up with the nuclei species separated following the mass/charge ratio in an electromagnetic separator.

The known isotopes are organized on the nuclear chart (see figure 1.3) in a similar way the atoms were organized in the Mendeleev periodic table. This table arranges the nuclei in colors and positions following the stability and their amount of protons and neutrons. The limits of the nuclei chart are regarded as the dripline, but it does not have an obvious definition (a deeper discussion can be found in [9]). The dripline can be regarded as the boundaries where the nuclei cannot keep

1. Introduction

more neutrons or protons within them [10], in a more theoretical approach it can be referred to as where the separation energy of the nucleons goes to zero [11], the definition can also point to the nuclei whose last nucleon is not bound and has decay times within the strong force interaction times, 10^{-22} s or faster [12]. The definition of [11] gives an interpretation for the limits of the dripline to be at the lightest isotope for the proton-rich nuclei and the lightest isotone for the neutron-rich nuclei, in that case ${}^6\text{Li}$, ${}^6\text{He}$, ${}^8\text{Li}$, ${}^8\text{He}$, ${}^{11}\text{Be}$, ${}^{11}\text{Li}$, ${}^{14}\text{B}$, ${}^{14}\text{Be}$, ${}^{17}\text{C}$, ${}^{17}\text{B}$, ${}^{19}\text{C}$, ${}^{19}\text{B}$, ${}^{22}\text{N}$, ${}^{22}\text{C}$ and ${}^{26}\text{F}$ would be the limits for the light neutron-rich nuclei. The green nuclei of figure 1.4 have a negative separation energy $S_{n,p} < 0$ and decay by proton or neutron emission, they do not even have a bound energy level, thus they are usually regarded as unbound nuclei or nuclei beyond the dripline.

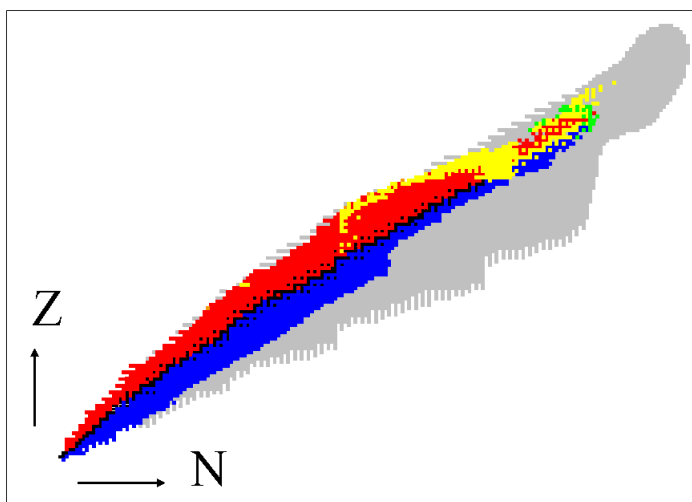


Figure 1.3: Nuclear chart. It increases in neutron number from left to right, and increases in proton number from top to bottom. Black color isotopes are stables. Red colored are proton rich, thus promoting β^+ decaying. Blue colored nuclei are neutron rich and promote the β^- emission. The grey-colored part are still unmeasured but predicted isotopes.

1. Introduction

neighbours and much stronger than the commonly observed trend $R \sim 1.18 \cdot A^{1/3}$ for the stable nuclei (see figure 1.5). This data suggested a deformation or a matter distribution tail.

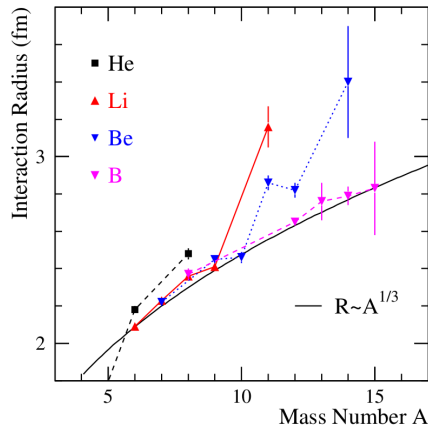


Figure 1.5: Comparison of nuclear radii between the stable nuclei trend of $R \sim A^{1/3}$ and several isotopes of Helium, Lithium, Beryllium and Boron. The size increase of ${}^6\text{He}$, ${}^8\text{He}$, ${}^{11}\text{Li}$, ${}^{11}\text{Be}$ and ${}^{14}\text{Be}$ is pronounced. Image taken from [22].

This feature was defined by Hansen and Jonson in 1987 [23] as Halo structure, it was understood as an extension of the size of the nucleus caused by one or two nucleons tunneling out of the classical forbidden region of the nuclear core potential, therefore certain loosely bound nucleons increase the size of the system leading to an escalation of the interaction cross-section. This phenomenon only occurs with a weak Coulomb or centrifugal barrier, causing that the only measured halo nuclei in the neutron deficient side of the nuclei chart are ${}^8\text{B}$, ${}^{17}\text{F}$, ${}^{17}\text{Ne}$ and deuteron if it is considered as such, whereas neutron halos are more than 10 isotopes (considered from [24] in 2013).

The large space distribution can be correlated using the Heisenberg principle to a very narrow momentum distribution which is another signature of the halo structure. In the same way, a small binding energy and low relative angular momentum of the valence nucleons (s or p states) are also conditions for the formation of halo states.

Within the halo structure it is worth considering two different cases, the two-body halos, like ${}^{11}\text{Be}$ or ${}^8\text{B}$ that only have one loosely bound nucleon in the last orbit and the three-body halos, like ${}^{11}\text{Li}$ and ${}^{14}\text{Be}$ which have two nucleons instead. This

1.3. The dripline fauna: Halos and unbound nuclei

latter kind is widely known as *Borromean nuclei* [25] and have certain special properties. The name comes from the coat of arms of the Borromeo family from Italy, three linked rings such as if one of them is removed the others would disentangle. The relationship of the symbol with the three-body halo structure comes from the fact that such a structure is bound while the two possible subsystems, isotope + nucleon or nucleon + nucleon are unbound. Hence, this produces certain pairs of isotopes that the odd neutron-numbered is unbound while the even neutron-numbered is bound.

^{11}Li was the first identified halo and still is the prototype for comparison. Its ground state has a binding energy around 300 keV [10] with a total matter radius of 3.53 (10) fm for the interaction cross-section [24] (see figure 1.6 to compare it with Calcium and Lead). For the purposes of this thesis, the halo nuclei ^{14}Be has special interest, it has a binding energy of above 1 MeV and a matter radius of 3.10(15) fm [24] from interaction cross-section. The core of this nuclei is ^{12}Be which is easily polarizable and it is known to have four bound states 0^+ , 2^+ , 0^+ and 1^- . It has the $N=8$ shell closure suppressed (as well as ^{11}Li), making it show parallel properties to the ^8He , thus it is closer to a $^{10}\text{Be}+n+n+n+n$ system than a $^{12}\text{Be}+n+n$. The unbound nuclei ^{13}Be , in the middle ground between the core isotope ^{12}Be and the borromean ^{14}Be needs to be studied to have a deeper knowledge of this area of the nuclei chart.

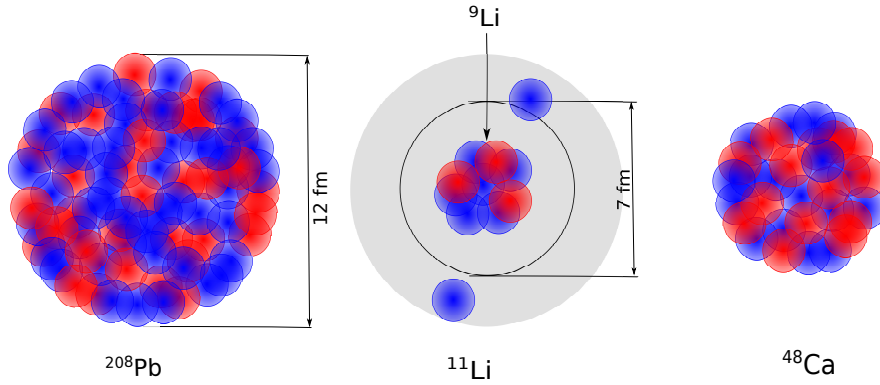


Figure 1.6: Size comparison between the schemes of the stable nuclei ^{208}Pb and ^{48}Ca and the two neutron halo nuclei ^{11}Li (middle of figure). The size of the nucleus with $R_{rms} \sim 3.53(10)$ fm [24] is comparable to the ^{48}Ca , whereas the distance between the two neutrons can reach the size of the ^{208}Pb $R_{nn}^{rms} \sim 6.6(1.5)$ fm [10].

1. Introduction

1.3.2 Unbound nuclei

Light nuclei close to the dripline are marginally bound, thus they usually do not have particle-bound excited states, nevertheless it is possible to feed excitations in the continuum. As has been mentioned before in the text and it is clearly stressed in figure 1.4, it is possible to produce and observe certain combinations of protons and neutron that are beyond the dripline, such systems without bound states are known as unbound nuclei.

It is common to refer to these non-bound states as resonances, not as nuclei. Therefore, the prime question that should be asked upon approaching unbound nuclei is *what is defined as a nucleus?*. Unfortunately there is not a satisfactory agreement around this subject. The main criterion that can be followed to achieve a conclusion is the lifetime of the potential nucleus. As explained for the halo nuclei, the two barriers that must be overcome by a nucleon to tunnel out of the nuclear core potential is the Coulomb barrier and the centrifugal barrier due to the angular momentum, thus the lifetimes of the neutron-deficient isotopes can be longer and usually increasing with Z (due to the Coulomb barrier), even longer than the \sim ms scale of the beta decay. On the other hand, the neutron-rich isotope neutron emission is just hindered by the angular momentum, hence they usually have lifetimes shorter than picoseconds. The IUPAC (International Union of Pure and Applied Chemistry), which is the world authority on naming of chemical elements, set a constraint on the lifetime of at least 10^{-14} s [26] for considering it as a new element, based in the time needed for a nucleus to acquire its outer electrons, as an element can not be considered as such without electrons. Such a guideline would be an applicable criterion following a similar reasoning, however the time-scale for nuclear phenomenon (as mentioned at the end of section 1.2 about the dripline) is in the order of 10^{-22} s, therefore such a lower limit would be more consistent. However, this reference threshold is just not clearly defined (more about this discussion can be found in [9]).

The first measured neutron-rich unbound nucleus was ^5He in 1937 by Williams et al [27] and it was not until 1965 [28] with the study of the di-neutron scattering length that another resonance was found. Since then, and more insistently after the development of the radioactive beams, a wide variety of these neutron unbound nuclei have been identified. Figure 1.4 shows the variety of these resonances that have been found in the last years, making obvious that in order to have a deep understanding of the boundaries of nuclear structure it is mandatory to investigate them. The bound nuclei with the highest ratio $\frac{N}{Z} = 3$ is ^8He , whereas the unbound systems are able to reach much higher limits like ^7H and ^{10}He with $\frac{N}{Z} = 7$ and 4, therefore with a ratio difference with the last bound isotope of $\Delta\frac{N}{Z} = 4$ and 1. The theoretical nuclear models, due to the difficulties of the many-body problem, are still not able to describe in a general way the nuclear force. The unbound systems are laboratories to test the theoretical models for the interaction between a core and single neutron (in the case discussed here) above or on the limits of the nuclear force.

1.3. The dripline fauna: Halos and unbound nuclei

Recent summaries and updates in unbound nuclei research have been published by Tanihata et al [29], Simon et al [13] in 2013 and Baumann et al [30] in 2012. Some of the most recent results for neutron rich unbound nuclei, involve assigning a ground state 0^+ and a excited state 2^+ for the ^{10}He [31][32]. The $^{25-26}\text{O}$ resonances have also been subject of research lately [18][17] finding a ground state $3/2^+$ for the first, and a 0^+ ground state and a 2^+ excited state for the latter. The Oxygen neutron-rich chain has been the subject of special attention due to the intention to reach the double magic nuclei ^{28}O .

1.3.3 ^{13}Be

The aim of this work is the study of the unbound nucleus ^{13}Be in the context of an experiment that populates it via the reaction $^{14}\text{B}(p,2p)^{13}\text{Be}$ using a CH_2 target, including Quasifree scattering conditions. The experiment was performed at GSI in 2010 by the R3B Collaboration and featured a gamma-ray detector, which only has been included before in one work [33]. This exotic Beryllium isotope has been controversial over the last years, being the target of several studies. The following will be a brief report of the existing published results.

The first observation was in 1983 by Aleksandrov et al [34] using the reaction $^{14}\text{C}(^7\text{Li},^8\text{B})$ finding a state at 1.8 MeV above the $^{12}\text{Be} + n$ threshold, with $\Gamma=0.9\pm 0.5$ MeV, using the missing mass method. Almost ten years passed until the next measurement was made by Ostrowski et al in 1992 [35] at VICKSI (Berlin) using a double-exchange reaction $^{13}\text{C}(^{14}\text{C},^{14}\text{O})^{13}\text{Be}$ at $E_{lab}=337$ MeV, determining that the ground state was at 2.01(5) MeV against one neutron emission with $\Gamma=0.3(2)$ MeV and one excited state at 5.13(7)MeV with $\Gamma=0.4(2)$ MeV, even finding indications of another excited state around 7.51 MeV. In 1995 Korshennikov et al [36] with $d(^{12}\text{Be},p)$, observed the same state around 2 MeV as well as suggesting three excited states at $\sim 5, 7$ and 10 MeV. At the same time, von Oertzen et al [37] published a measurement at 24 MeV/u for the reaction $^{13}\text{C}(^{14}\text{C},^{14}\text{O})$ producing a strong resonance at 2.01 MeV which they attributed to a $d_{5/2}$ state, and another at 5.13 MeV. Belozyorov et al [38] in 1998 used the reaction $^{14}\text{C}(^{11}\text{B},^{12}\text{N})$ at 190 MeV/u, they assigned a $J=1/2$ character tentatively to a ground state settled to the lower energy of 0.80(9) MeV, and reported about several additional states at 2.02(10), 2.90(16), 4.94(12), 5.89(14) and 7.8(2) MeV. The next important observation was published in 2000 by Thoennesen et al [39] using a 80 MeV/u beam of ^{18}O fragmented on a ^9Be target, reporting a low-lying (<200 keV) virtual s-state with $a_s < -10$ fm scattering length. In 2004 Simon et al [40] published results from GSI using a ^{14}Be beam of 250 MeV/u impinging on a carbon target which produces two p and d wave resonances. That same year Lecouey et al [41] reported about a one proton knockout experiment at GANIL using a 41 MeV/u beam of ^{14}B impinging on a Carbon target and used the invariant mass method to find a low-lying s-state at about 0.7 MeV and d-state at around 2 MeV. Haik Simon et al [42] performed another experiment in 2007 with

1. Introduction

a 287 MeV/u beam of ^{14}Be , reporting a virtual s-state with a scattering length of $a_s < -3.2$ fm, as well as three states at 2, 3 and 5 MeV.

In 2010, Kondo et al [33] published the results from an experiment performed at RIKEN using the invariant mass method with a one-neutron removal reaction of $^1\text{H}(^{14}\text{Be}, ^{12}\text{Be}+n)$ with 69 MeV/u energy, it was the first experiment that measured the γ rays emitted by the ^{12}Be daughter in coincidence with ^{13}Be . The authors found one virtual s-state with $a_s = -3.4(6)$ fm and two resonances at 0.51(1)MeV and 2.39(5)MeV with p and d character. The relative energy spectrum extracted in that experiment is in figure 1.7.

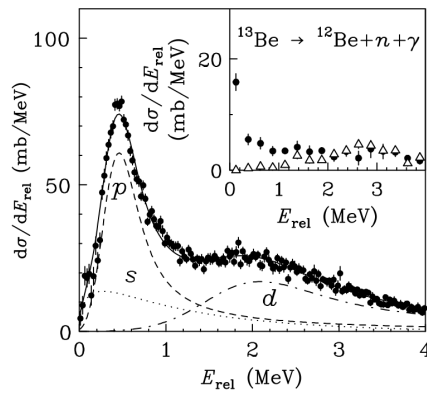


Figure 1.7: ^{13}Be relative energy from the paper of Kondo et al [33]. The spectrum is fitted to one virtual s-state and two resonances p and d, further information in the text. The inset shows superimposed the relative energy of ^{13}Be in coincidence with two γ rays from the ^{12}Be . Black circles with the 2.1 MeV and white triangles with the 2.7 MeV gamma ray.

In 2013, Aksyutina and the R3B Collaboration [43] published new results coming from an experiment performed at GSI with 304 MeV/u using ^{14}Be neutron knockout impinging on a Hydrogen target. Additionally to the analysis of that data they adopted an holistic approach including in the interpretation of the results the data coming from Kondo [33], and taking into account the previously published results of the ^{13}Be . They assumed for the analysis that as the structure of ^{14}B has the main configuration $^{13}\text{B}(3/2^-) \otimes (sd)$ [44], meaning that only s and d states should be populated significantly in ^{13}Be whereas with neutron knockout p states can be populated. The investigation used the invariant mass method to get the relative energy of the system $^{12}\text{Be} + n$, whereas in order to extract the momentum interpretation of the resonances they used the momentum profile method (previously explained

1.3. The dripline fauna: Halos and unbound nuclei

also by Aksyutina [45] that same year), taking advantage from the assumption that the knocked out neutron inside the projectile (^{14}Be , a two neutron halo nuclei) has the same momentum as the $^{12}\text{Be} + n$ system. They performed a previous fit of the data considering the ground state to be $1/2^+$ at 0.81(6) MeV, the momentum profile analysis reported about a complication in the interpretation in this state, which seemed like a combination of $1/2^+$ and $1/2^-$ character. In order to solve this latter complication they introduced the possibility of destructive interference between two s-states, performing a new fit. The conclusions they reached included settling the ground state at 0.46 MeV as an s-state interfering with an excited s-state at 2.9 MeV, one $1/2^-$ state at 3.02 MeV and one $5/2^+$ state at 1.95 MeV as well as one final state at 5.2 MeV with $J=5/2^+/3/2^-$ character. They left open the possibility of another state around 1 MeV with $l \neq 0$. In figure 1.8 the relative energy spectrum of Aksyutina is shown [43].

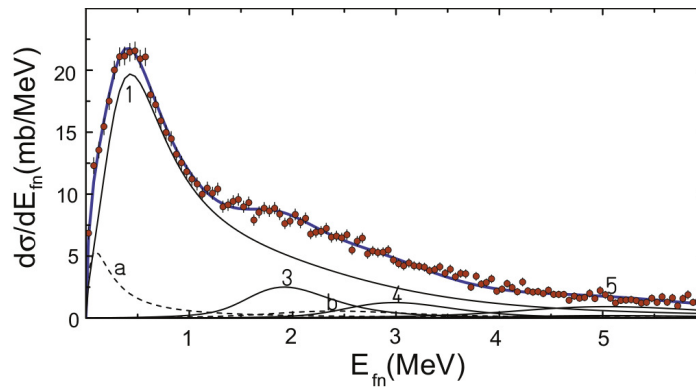


Figure 1.8: ^{13}Be relative energy from the published paper of Aksyutina et al [43]. The resonance number 1 describes the contribution from the two $l=0$ resonances with destructive interference. a and b are the cross-section of the relative energy in coincidence with gammas coming out of ^{12}Be found by Kondo (see figure 1.7). The component 3 have 1.95 MeV whereas the component 4 is at 3.02 MeV, the state at 5.2 MeV is the component 5.

1. Introduction

The last experimental result was published by Randisi et al [46] in 2014 from GANIL (figure 1.9 display the final result of decay energy). The investigation was carried out using a $^{14-15}\text{B}$ beam of 35 MeV/u via breakup in a Carbon target. The invariant mass method was used to extract three resonances at $E_r=0.4, 0.85$ and 2.35 MeV with an angular momentum of $J=1/2^+, 5/2^+$ and $5/2^+$.

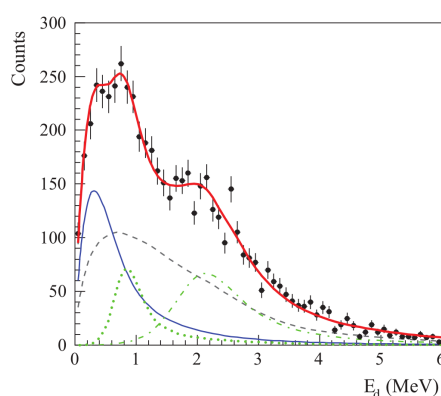


Figure 1.9: ^{13}Be decay energy from the paper of Randisi et al [46]. The blue solid line is the ground s-state at 0.40(3) MeV whereas the dotted green line is a d-wave resonance with 0.85(13) MeV and the dot-dashed green line is a another d-wave resonance with 2.35(14) MeV. The gray dashed line is a nonresonant continuum.

1.3.4 Resonances or quasi-stationary states.

As the main subject of this work are the previously mentioned unbound or resonance states, its formal interpretation will be briefly introduced.

A simple interpretation of the resonances [47] could be understood taking into account the square-well potential model with a particle inside. It is well-known that in a such a case the wave-function will only be solved by a finite number of negative energies within the potential and the particle will be classically confined inside. The wave that represents the particle needs to be in phase whenever it reaches the boundaries to the potential, this only happens in a finite number of energies. However outside the square-well the wave can adopt any energy, although it must be taken into account that the discontinuity of the potential provokes reflection to particles with energies close to the boundaries, therefore close to the potential frontier there are certain favoured energies, that keep the particle at least partially confined. Such energies are called resonances or quasi-stationary states. This is a quan-

1.4. Direct Reactions: Knockout

tum phenomenon that does not happen in the classical world. These resonances emerge as prominent peaks of the excitation spectrum (i.e. in the relative energy for the unbound system studied in this work), giving a hint that there is a kind of state at that energy position.

The resonance can also be understood with the wavefunction properties. In a simple case just considering elastic scattering, the wave number of the wavefunction inside the nucleus potential is $k_i = \sqrt{2m(E_0 - V_0)}/\hbar$ while the external part is $k_e = \sqrt{2mE_0}/\hbar$, therefore for a small energy E_0 , and considering a negative potential with absolute value $V_0 \gg E_0$, the internal part of the wavefunction will have a higher frequency than the external. At $r=R$ both parts must join with continuous function and derivatives but due to the difference in frequency, the amplitude of the internal part is going to be much smaller than the external part. The resonance energy is the one that produces that both amplitudes are the same and the first derivative of the function at $r=R$ is very close to zero (see figure 1.10).

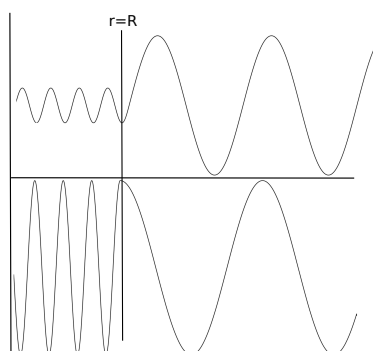


Figure 1.10: Two cases of wavefunction with different E_0 . The second case, where the amplitude of the internal and the external part of the wavefunction are the same as well as the first derivate of the function is close to zero, it is a resonance.

1.4 Direct Reactions: Knockout

Since the times of Rutherford, nuclear reactions have been widely used to probe the atomic nucleus. The collision of subatomic particles or nuclei breaks them up in their inner components or change them in a fundamental way. The reaction outcome is greatly determined by the energies of the projectiles, such energy selection can be achieved using particle accelerators.

1. Introduction

The nuclear reactions are usually divided in two different types [48][47]. If the interacting components form a compound system which stays together long enough to share the energy uniformly, then at some point that energy is accumulated in one component which makes the system to decay, this is called Compound Reaction. On the other hand if the interaction is glancing between both particles and rapid in the nuclear force order of magnitude ($\sim 10^{-22}$ s) (which can be up to six order of magnitude faster than the compounds reactions), it is regarded as a Direct Reaction. The latter is favoured at higher energies of the projectile and taking into account the De Broglie hypothesis ($\lambda = \frac{h}{p}$), the wavelength of the particle would decrease with increasing the energy, making it easier to penetrate inside the nucleus and probe deeper into the nuclei of interest.

There are three main types of Direct Reactions, besides elastic scattering where there is no modification of the nucleus. The first case is when the incident particle suffers inelastic scattering and the received energy is spent on exciting rotational and vibrational modes of the nucleus. The second case includes modifications in the nuclei composition, such reaction involves the transfer of one or several nucleons from either the target to the projectile (Pick-up reaction) or the opposite (Stripping Reaction). The last type of reaction is regarded as Knockout Reaction, and the interaction of the projectile with the target, provokes the ejection of one nucleon or light fragment from the target.

Knockout reactions have been used as a powerful tool to probe deeply bound nuclear shell structures [11], mainly using high energy beams (above 100 MeV/u). As this kind of reaction involves at least three outgoing particles, due to the momentum conservation, in order to understand the whole picture one needs to sum all the outgoing momenta. The figure 1.11 shows an scheme of a typical knockout reaction with an incoming proton impinging on a nucleon inside a Target of mass number A. The momentum conservation is indicated in equation 1.1, considering the Target to be at rest whereas the nucleon inside the Target has certain momentum.

$$p_P + p_N = p_{T(A-1)} + p'_P + p'_N \quad (1.1)$$

At the modern accelerators of heavy particles, the *Inverse Kinematics* method is used to investigate the exotic nuclei provided by their radioactive beams (see section 1.2). This technique involves colliding unstable nuclei with any mass against light stable targets, therefore the object of interest of the experiment is the beam nuclei not the target as it usually was with stable beams. Such an approach inverts the intention of Knockout reactions to knocking-out a nucleon from the beam not from the target. Using this method it is possible to populate and to study very short lived nuclei such as unbound resonances that would not survive the flight through a fragment separator.

1.4. Direct Reactions: Knockout

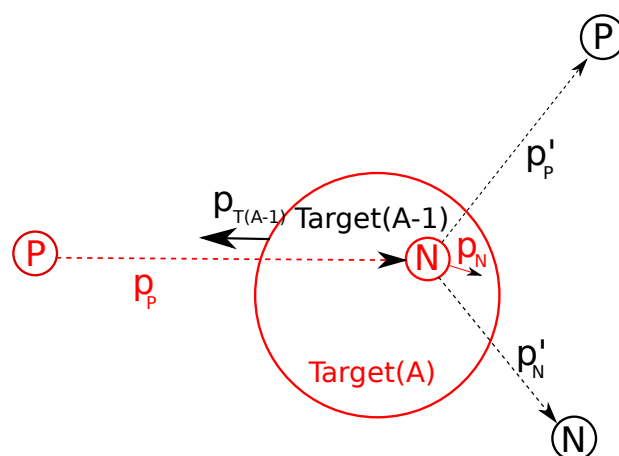


Figure 1.11: Scheme of a Knockout Reaction of a proton (P) impinging on a Target(T) with mass number A , knocking out a nucleon (N). p are the linear momenta, **red color** indicates the situation before the reaction whereas the black colored lines and spheres indicates the outcome of the reaction. Dashed lines indicates the moving nucleons. The opening angle between particles of the same mass in a Knockout Reaction is $\sim 90^\circ$.

1.4.1 Quasifree scattering

The Quasifree scattering (QFS) reaction is a particular type of knockout reaction that fulfill certain conditions. The projectile must be simple, usually a proton or an electron, which can be single or within a nucleus. The key condition is that the rest of the projectile is not involved in the reaction process, acting as a spectator. Therefore the interaction can be considered as Quasifree, in first approximation the other kind of interactions do not need to be taken into account. The typical reactions are $(e,e'p)$, $(p,2p)$ or (p,pn) , although this work is going to focus in the $(p,2p)$ reaction. This type of reaction has been a primal interest of the R3B Collaboration as a tool to investigate the single particle structure or the cluster structure of nuclei. Several works have been carried out studying this kind of reaction e.g. [49][50][51][52].

In reactions like $(p, 2p)$ or (p, pn) a proton from the target knocks-out a nucleon from the beam in inverse kinematics. Both particles are emitted in the same plane, and as both have the same mass, with an opening angle of $\sim 90^\circ$ in the laboratory frame. The coplanar condition translates to $\Delta\phi \approx 180^\circ$, whereas the high energies in inverse kinematics produce an opening angle of $\Delta\theta \approx 80^\circ$, such a degra-

1. Introduction

ation in the opening angle is because of the mass increase of the incoming nucleon due to the relativistic velocities ($\beta \approx 0.7$). Both angular trends can be used as signatures of the presence of this kind of reaction. The signatures can be seen in figure 1.12. A good summary with further explanation of this kind of reaction can be found in [53].

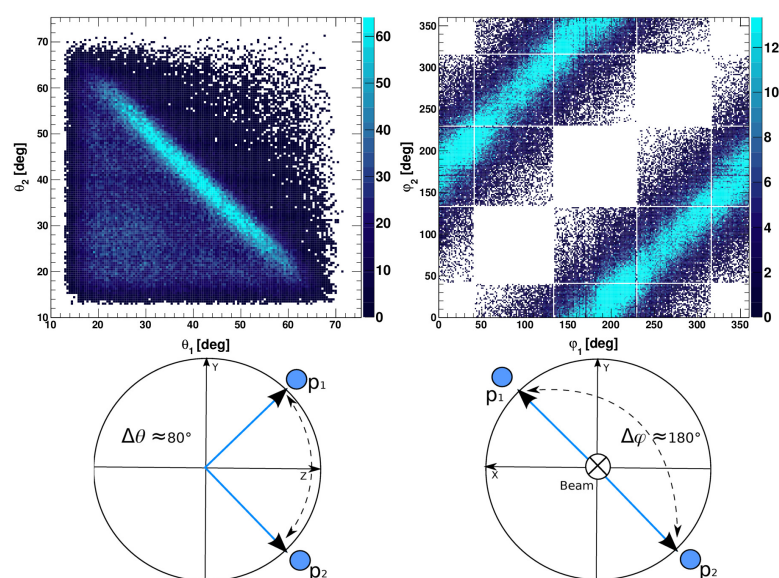


Figure 1.12: Quasifree scattering signatures for a $(p, 2p)$ reaction with CH_2 target. *Left:* It is shown the opening angle correlation $\Delta\theta \approx 80^\circ$ for a high energy QFS reaction in inverse kinematics in the laboratory framework. *Right:* It is shown the $\Delta\phi \approx 180^\circ$ coplanar correlation of the QFS reactions. Angular correlations taken from [50].

“ There is nothing like looking, if you want to find something.
You certainly usually find something, if you look,
but it is not always quite the something you were after. ”

J.R.R Tolkien, *The Hobbit*

2 Experiment & Detector setup

2.1 The experiment

The data analyzed in this thesis were taken during the S393 experiment [54] performed in the late summer of 2010 at GSI Helmholtzzentrum für Schwerionenforschung GmbH by the R3B Collaboration. The experiment was focused on two main tasks, the study of astrophysical reactions ratios relevant for the r-process nucleosynthesis and the use of Quasifree knockout reactions to study the evolution of shell and cluster structures close and beyond the neutron-dripline. In order to reach the channels of interest, six different settings of mass-to-charge ratios were used for the fragment separator.

The experiment had 21 days of beam time and a large amount of collaborators were involved along the preparation and run of the experiment, the information that might be of relevance was written in the elog [55]. As the dataset was huge, more than ten thesis have results based on this experiment, and the interaction between the PhD students and the professors involved is done through a second analysis elog [56].

The aim of this work is the study of the shell structure of ^{13}Be , a neutron-rich unbound nucleus at the dripline, this was done using $(p, 2p)$ reactions knocking out deeply bound protons from the incoming beam ^{14}B .

2.2 GSI Helmholtzzentrum für Schwerionenforschung GmbH

GSI [57] is a facility built in Darmstadt (Germany) in the year of 1969 and since then has been dedicated to the production and acceleration of heavy ions, currently it cooperates with hundreds of institutes around the world on research in different areas like material, biophysics, medical science, plasma, atomic and of course nuclear physics. Several of the super-heavy elements have been discovered at GSI, including Bohrium-107, Meitnerium-108, Roentgenium-111, Copernicium-

2. Experiment & Detector setup

112 and Hassium-108 named after the German state of Hesse, and Darmstadtium-110 named after the location of the research center.

Currently a major upgrade is being performed in the facility, thus it is not in operation at this time. The future installation FAIR (Facility of Antiproton and Ion Research) will be one of the largest research projects worldwide, providing ion and antiproton beams of high intensity and quality.

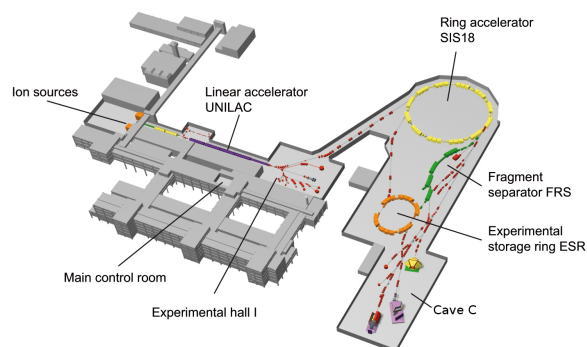


Figure 2.1: Overview of the GSI accelerator facility and the experimental beam production technique followed for the R3B Collaboration experiments. The ion source produces the primary beam, which is accelerated in the UNILAC and sent to the SIS18 in order to reach the higher energies. When the beam is extracted from the accelerator it is let to impinge on a light target that produces a cocktail of isotopes which go through the FRS that separates the different species before reaching the R3B experimental hall: Cave C, where is situated the detector setup.

2.2. GSI Helmholtzzentrum für Schwerionen-forschung GmbH

2.2.1 Ion sources

There are several ion sources in GSI for the production of a wide variety of ions with different intensities and ionizations, but in order to produce Argon as primary beam there were two sources (see figure 2.2) on operation during 2010, when the experiment was carried out:

- PIG (Penning Ionization Gauge) ion source
This source generates plasma inside a strong magnetic dipole field, producing gaseous and metallic ions.
- MUCIS (MULTI Cusp Ion Source)
This ion source has three spiral tantalum filaments placed simmetrically relatively to the beam axis. 60 SmCo-magnets creates the multi-cusp field of 1.8 T for producing all types of ion gases.



Figure 2.2: Pictures of the sources PIG(left) and MUCIS (right). From [57]

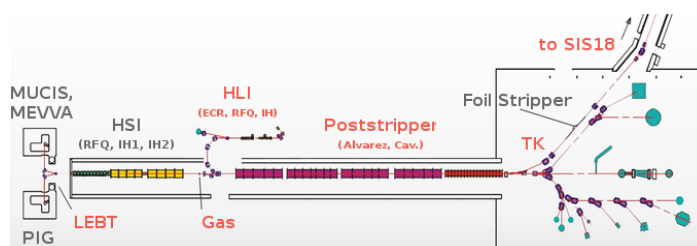


Figure 2.3: Scheme of the UNILAC, the connection with the ion sources at the left and the transfer line to the SIS 18 at the right.

2. Experiment & Detector setup

2.2.2 UNILAC

The UNIversal Linear ACcelerator [58] is the first acceleration stage, able to reach beam energies up to 11.4 MeV/u for elements from hydrogen to uranium.

From the ion source, the beam goes through the High Current Injector (HSI) which consists of a low energy beam transport system (LEBT), the 36 MHz IH-RFQ accelerating the ion beam from 2.2 to 120 keV/u and RFQ adapter matching to the IH-DTL consisting of two separate tanks accelerating the beam up to the HSI maximum energy of 1.4 MeV/u. The beam is stripped in a gas and one charge state is selected before injection to the DTL section where is accelerated to 11.4 MeV/u. Before the transfer to the SIS18, there is a foil stripper to increase the charge state of the ion followed by a charge state separator in order to chose the best charge state for the acceleration.

2.2.3 SIS(SchwerIonenSynchrotron) 18

The pre-accelerated ion beam coming from the linear accelerator is further accelerated in the heavy-ion synchrotron up to 90% of the speed of light. The ring has a 216 m circumference with a maximum bending power of 18 Tm. A proton beam can be accelerated up to 4.5 GeV while an Uranium beam can reach 1 GeV/u, the beam emmitances can go from 5x8 to 30x8 mm mrad.

The beam in a synchrotron needs different time periods to be accelerated before extraction, this causes that the beam goes forward in ion bunches with pauses in-between. The acceleration cycles are called spills.

When the beam is extracted from the SIS it is let to impinge in a thin primary target with low Z , producing the secondary beam of a wide variety of lighter elements which are injected in to the FRS. During the S393 experiment this primary target was Beryllium of 4.011 g/cm². In this experiment the Argon (⁴⁰Ar) primary beam was accelerated to 490 MeV/u.

2.2.4 FRS

The FRagment Separator [59] [60] is an achromatic magnetic forward spectrometer with a momentum resolving power of 1500 for an emittance of 20π mm mrad. It is composed of four stages each of them consisting in 30° dipole magnets and a set of quadrupoles before and after the dipole in order to focus the beam (see figure 2.4).

After the primary target the species of the secondary beam are selected using a method involving the energy loss of the isotopes and the magnetic rigidity. First the ions are separated according to their mass-to-charge ratio, this is done based in the Lorentz force which equals the centripetal force on a circular radius ρ keeping the ratio between the charge (Z) and the mass (A) of the isotope, see equation 2.1,

2.2. GSI Helmholtzzentrum für Schwerionen-forschung GmbH

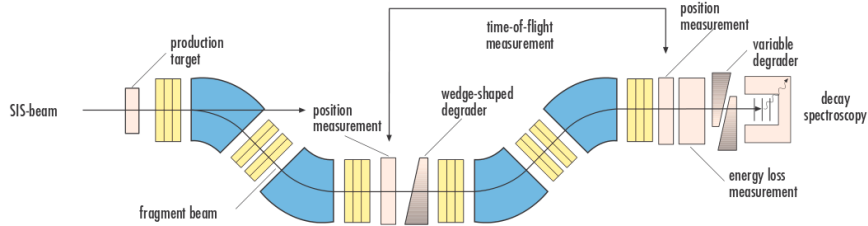


Figure 2.4: Overview of the fragment separator. The blue dipoles bend the beam and separates the cocktail beam according to A/Q , and the wedge degraders in pink-grey assure a specific energy loss. The yellow colored parts are quadrupoles for focusing purposes and the scintillators for measurements are shown in pink. Image taken from [60].

where K is a constant, B is the magnetic field intensity, β is the ratio of the velocity of the isotope and the speed of light and γ is the lorentz factor. The latter equation is only valid for high energies, fully stripped beams like the ones used in this facility. Therefore what this equation means is that for a specific ratio $\frac{A}{Z}$ a certain magnetic rigidity ($B\rho$) is fixed, thus only those ions will pass through and follow a unique trajectory(ρ) for a given magnetic field(B).

$$B\rho = K \cdot \frac{A}{Z} \cdot \beta \cdot \gamma \quad (2.1)$$

A wide variety of ions will have the same mass-to-charge ratio so in order to select a specific ratio one uses wedge-shaped degraders as shown in figure 2.4. The energy loss of heavy charged particles follows the Bethe-Bloch formula (equation 2.2), which states that the energy loss is higher according to the amount of interacting material. The wedge degraders have different widths depending on how far they are inserted into the beam line, thus it will cause different energy loss depending on the trajectory of the fragments through the separator. However, this also causes a loss of beam intensity, so in some cases it is necessary to avoid this last ion-selection process.

$$-\frac{dE}{dx} = \frac{4\pi n Z^2 e^4}{m_e v^2} \left\{ \ln \frac{2m_e v^2}{I \left[1 - \left(\frac{v}{c} \right)^2 \right]} - \left(\frac{v}{c} \right)^2 \right\} \quad (2.2)$$

Along the FRS there are up to eight different 3 mm thick scintillators, called from S1 to S8, used to perform time-of-flight, position and energy loss measurements, which are needed to monitor the beam.

2. Experiment & Detector setup

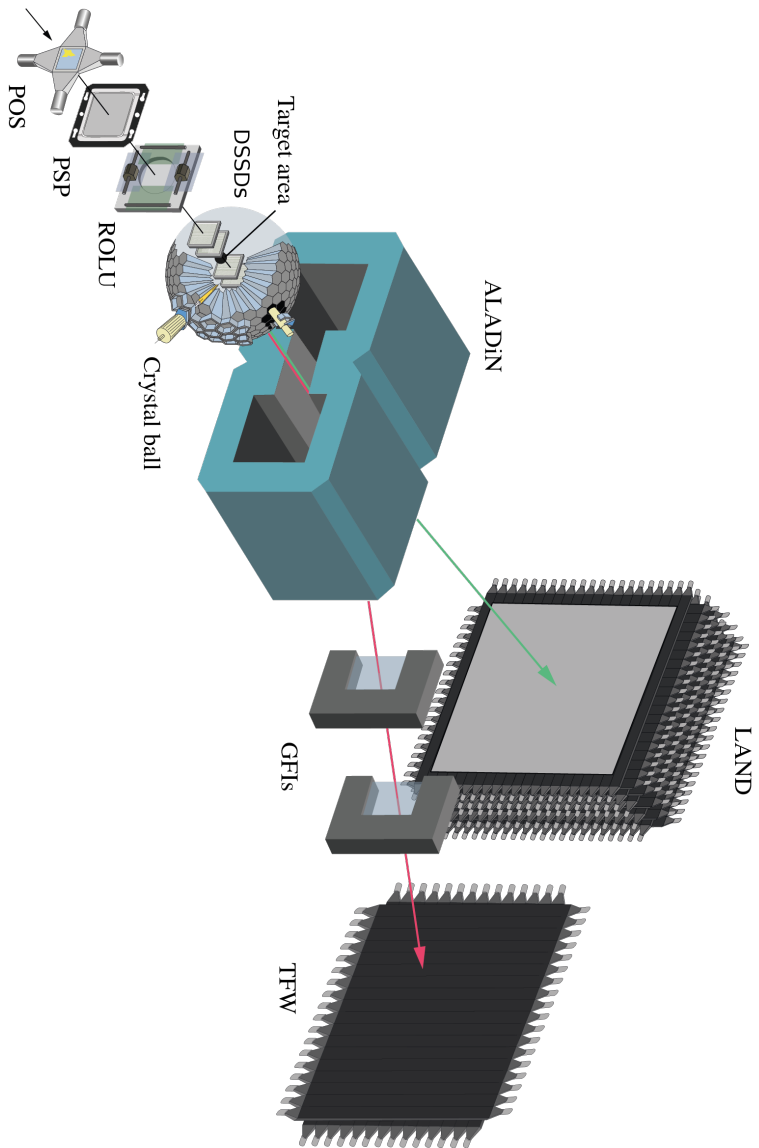


Figure 2.5: Setup overview. The important detectors are shown, and the three different setup stages are indicated as well, the incoming, around the target and outgoing, the latter is divided in three branches based on the purpose: neutrons, fragments and protons. The proton branch is not included because it is not used in this work. Imagen taken from [61].

2.3. Cave C: R3B Setup

2.3 Cave C: R3B Setup

Once the beam has passed the fragment separator it ends up in Cave C, where the R3B setup (with small changes) has been producing data for many experimental campaigns, in this document just the S393 configuration will be explained. An overview of the setup is shown in figure 2.5.

The main feature of this detector setup is being capable to make complete kinematic measurements, this means that it is able to record all the information including energy, mass and charge from the different incoming isotopes and the outgoing reaction products. To accomplish this it is equipped with a large variety of plastic scintillators, stripped and non-stripped silicons, fiber detectors and a strong electromagnet.

The setup can be divided in three different stages following the position and purpose of the detectors: Incoming, around the target and outgoing.

2.3.1 Incoming beam detectors

S8 and POS

In order to make time-of-flight measurements two scintillators are used, S8 is the last one from the FRagment Separator, it consists in a plastic paddle with two photomultipliers (PMTs) at both ends.

The POS is located in the incoming beam pipe of the Cave C setup, it consists in a square shaped plastic of $5.5 \times 5.5 \text{ cm}^2$ with four PMTs attached to the sides, it is generally used as the start-stop of the time-of-flight measurements with a resolution of 470 ps, it also can give information of the energy loss of the beam, although this latter possibility was not used in the present experiment. A schematic view of the detector is shown in figure 2.6.

ROLU

The ROLU device allows to define the beam size before reaching the reaction target, using four remotely controlled scintillators. Any particle that does not go through the defined hole made by the disposition of the four scintillators as can be seen in figure 2.7 will hit one of them and produce a signal which can be used as a veto trigger for the Data Acquisition System.

2. Experiment & Detector setup

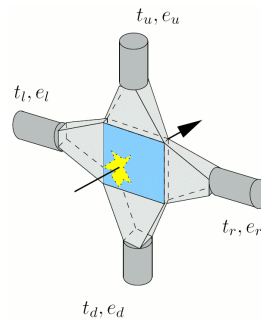


Figure 2.6: Schematic view of the POS. When the beam hits the plastic, the scintillation light is produced, reaching the four photomultipliers. The four signals collected in the PMTs give time, energy and position information of the beam, although nowadays this detector is primarily used only for the time-of-flight.

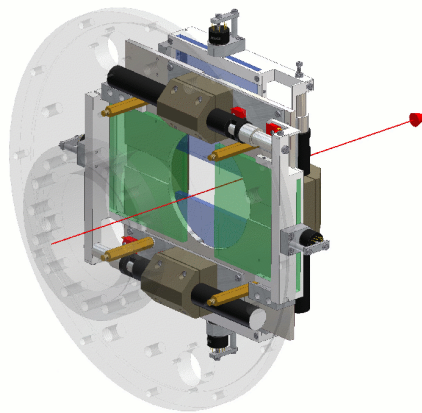


Figure 2.7: The ROLU name comes from the four scintillators in German: Rechts (Right), Oben (Above), Links (Left), Unten (Below). The paddles have the size of $95 \times 100 \text{ mm}^2$ and a thickness of 5 mm.

2.3. Cave C: R3B Setup

PSP

The Position Sensitive silicon Pin diode (PSP) is a square plate of high resist- ing n-type silicon with a thickness of $300\ \mu\text{m}$ and an active area of $4.5 \times 4.5\ \text{cm}^2$. This detector is used for tracking the beam position and for identification of the isotopes charge by energy loss. The front side of the plate has Boron ions implanted, forming a p-n junction, making this side the anode and the other side the cathode.

As can be seen in figure 2.8, there are four independent readouts in the cor- ners of the anode, in order to collect the charge for position reconstruction purposes. As the charge fraction collected in each different readout is proportional to the po- sition of the charge deposition it is possible to extract that information using the equations 2.3 & 2.4. The cathode has also one charge collector which allows to know the energy loss in the detector.

$$X_{pos} = \frac{(Q_2 + Q_3) - (Q_4 + Q_1)}{(Q_1 + Q_2 + Q_3 + Q_4)} \quad (2.3)$$

$$Y_{pos} = \frac{(Q_1 + Q_2) - (Q_3 + Q_4)}{(Q_1 + Q_2 + Q_3 + Q_4)} \quad (2.4)$$

The PSP has a position resolution of approximately $200\ \mu\text{m}$ and an energy resolution of 1%. In the present experiment this detector was not used for position measurements, only for the incoming nuclei charge determinations.

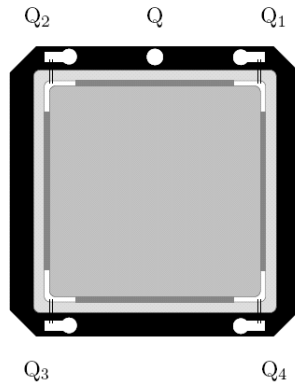


Figure 2.8: Schematic view of the PSP. The anode holds the 4 position detection charge readouts while the cathode have one single contact for charge collection to detect the total energy loss of the incident nuclei in the detector.

2. Experiment & Detector setup

2.3.2 Around the target detectors

Target

Of course the target is not a detector but it is used to select the reaction channel and is a main part of the setup as well and that is why it is included in this section.

The target holder is a wheel with several square-shaped locations around the border to keep a variety of targets (see figure 2.9). It is remote controlled from outside the experimental hall, which allows to change the desired target without opening the cave.

In the experiment S393, three different targets were used:

- Polyethylene (CH_2) 922 mg/cm^2 : It was used to produce the (p, 2p) reactions. As an alternative a liquid Hydrogen target can be used, but it was not possible in this experiment.
- Carbon (C) of 935 mg/cm^2 : In order to extract the carbon contribution from the polyethylene target, some runs with a Carbon target were performed.
- Lead (Pb) of 2145 mg/cm^2 : This heavy target was necessary for the Coulomb excitation part of the experiment.

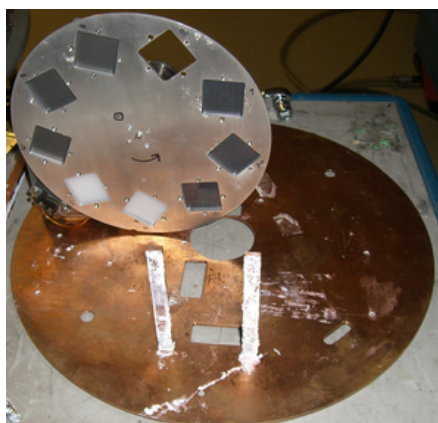


Figure 2.9: Target wheel picture taken before being installed for an experiment.

2.3. Cave C: R3B Setup

DSSDs

The Double-Sided Silicon Strip Detectors (DSSDs) box is composed of 8 micro-stripped silicon detectors with the main objective of tracking the beam before and after the reaction and the protons coming out from the (p, 2p) reactions, as the energies involved are high the isotopes goes very forward-oriented, thus high resolution and segmentation is needed.

The orientation of the different detectors is shown in the figure 2.10. The four off-beam silicons (that were boxing the target out of the beam trajectory) failed to work properly during the experiment so are not used neither on this work nor in any of the of the analysis of this experiment, so from now on I will only focus on the four on-beam silicon detectors that actually were capable to produce data.

Each of the silicon sensors is $72 \times 40 \text{ mm}^2$ and 0.3 mm thick. Every sensor has an implantation pitch on the junction side (S-side or p-side) of the sensor of $27.5 \mu\text{m}$ with a corresponding readout pitch of $110 \mu\text{m}$, every fourth strip is connected to a single readout channel whereas the others are left floating. The strips are capacitive coupled, which allows to improve the resolution getting information from them. The K-side (n-side) of the sensor has a readout pitch of $104 \mu\text{m}$ in this case every strip is readout. The result is 640 strips on the S-side (X) and 384 on the K-side (Y) for a total of 1024 channels in each detector. The resolution in both sides of the detector is $50 \mu\text{m}$, whereas the angular resolution that can be obtained is close to 1 mrad. The detectors are rather slow to digitize all the channels every event, with times in the order of μs .

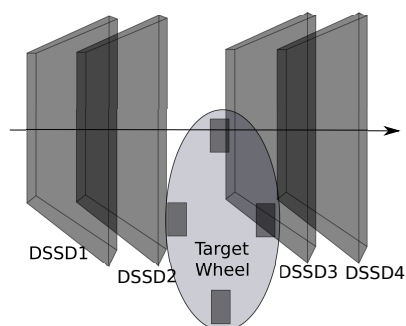


Figure 2.10: DSSD disposition around the target wheel. A scheme of the four working silicons detectors on-beam close to the target. Although there were four more boxing the target wheel as they failed to work in the experiment they have not been included.

2. Experiment & Detector setup



Figure 2.11: Photograph of a Micro-Strip Double Sided Silicon Detector (DSSD), showing the 0.3 mm thick sensor and with two pictures zoomed to the readout area, indicating the readout pitch which is 110μ and $104 \mu\text{m}$ for the S-side and K-side respectively. Image taken from [50].

Crystal Ball

Surrounding the target and the silicon box, there is a sphere of 162 NaI scintillator crystals assembly called Crystal Ball with an inner radius of 25 cm and a crystal length of 20 cm (see figure 2.12). This geometry follows the requirement of each crystal covering the same solid angle of 77 msr with four different crystals shapes: Regular pentagon (12), and three kinds of hexagons (60+60+33).

This detector has two main purposes: Detection of the gamma rays emitted from the nuclear reaction produced in the target, and detection of the knocked out protons, specially for the (p,2p) reactions. The energy resolution of the gamma branch is 6% in each crystal at 1 MeV, whereas the uncertainty due to the angular coverage of the detectors is 7.5° . The gamma efficiency has been reported to be in average 35%[62].

The relatively high segmentation of Crystal Ball permits to perform Doppler correction for the high energy gammas emitted in-flight from fragments moving at relativistic energies. In order to be able to detect the high energy protons with the same scintillator crystals the readout of the most forward oriented photomultipliers was modified. 64 of the PMTs had two readouts, one from the dynode, and another one from the anode with less amplification allowing to record the energy loss up to 274 MeV for high-energy protons, otherwise this high energy particles would have saturated the readout.

2.3. Cave C: R3B Setup

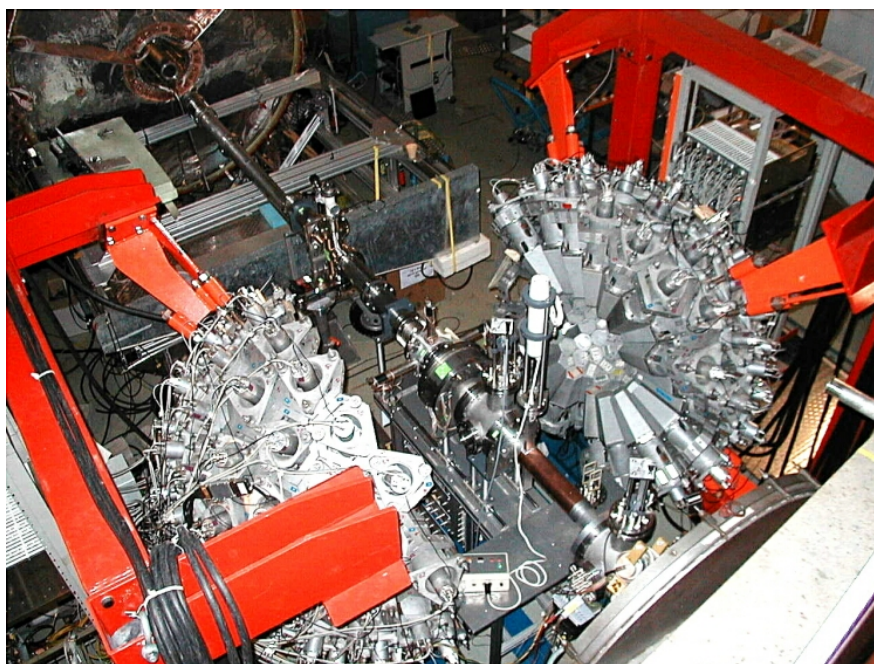


Figure 2.12: Photograph of Crystal Ball opened. There are two holders, one for each side of the ball, so it can be kept completely opened in order to work close to the target. When the ball is closed most of the 4π of solid angle is covered except from three crystals, one in the bottom for the target holder and two for the beam pipe coming in and out.

ALADIN

Approximately two meters away downstream of the Crystal Ball, the most important “member” of the R3B setup is found, the A Large Acceptance Dipole magnet (ALADIN). Its purpose is bending the reaction products to the three different branches of detectors with an angular acceptance of ± 60 mrad and a maximum magnetic field strength of 1.5 T. The parameter used to control the magnetic field in each run is the current of the magnet which can go up to 2500 A, although after 1900 A the correlation between the current and the magnetic field strength becomes nonlinear.

2. Experiment & Detector setup

2.3.3 Outgoing fragment detectors

Proton Branch

The protons are the reaction products that are most bended by ALADIN, thus at 30° from the forward direction two groups of detectors were placed to detect them. Two drift chambers for tracking and one time of flight wall at the end of the branch. As the proton branch is not used for the analysis of this document, is not going to be detailed.

Fragment Branch: GFI

The called Fragment Branch is at an angle of 15° from the forward direction of the setup after the ALADIN magnet. The first detectors are two fiber detectors, the GFIs (Gross-Fiber detektor) used for tracking the fragments and identification of the different masses.

These detectors are $50 \times 50 \text{ cm}^2$ consisting of 500 parallel fibers (see figure 2.13). Each fiber has $1 \times 1 \text{ mm}^2$ and is coated by a material of lower refraction index in order to guide the light, furthermore the cross-talk between neighbouring fibers is avoided by an additional white coating. The consequence of this covering is a reduction on the geometrical efficiency, going down slightly below 90%.

One end of the fibers have Position-Sensitive PhotoMultiplier (PSPM) for the identification of the hit fiber, and in the other end a common PMT is coupled in order to get timing information. The PSPM is a Hamamatsu R3941 with a rectangular photocathode of $64 \times 58 \text{ mm}^2$ and 16 mesh-type dynodes, while the anode has a rectangular grid of 18 wires in the X direction and 16 wires in the Y having a distance of 3.7 mm between them. In this way the charge distribution on the anode grid is correlated with the position of the light in the photocathode, using a mask as it is shown in the figure 2.13. The position resolution is $650 \mu\text{m}$.

Fragment Branch: TFW

At the end of the fragment branch there is a Time-of-Flight Wall (TFW) very similar to the one located in the proton branch. This detector gives the stop for the time-of-flight measurement after the reaction but it is also used as an energy loss detector able to identify charge differences of the fragments.

This wall is built on 32 plastic scintillators paddles of 5 mm depth, 18 are vertical with 10 cm width and length of 1.4 m, on the horizontal direction there are 14 paddles also 10 cm wide but 1.8 m long. At each end of the paddles there are a PMT able to detect the scintillation light and the timing. The time resolution is 0.5 ns and the position resolution is 5 cm.

The interaction on the scintillation paddles produce light that goes in both directions through the paddle until reaching the photomultipliers on each end. In

2.3. Cave C: R3B Setup

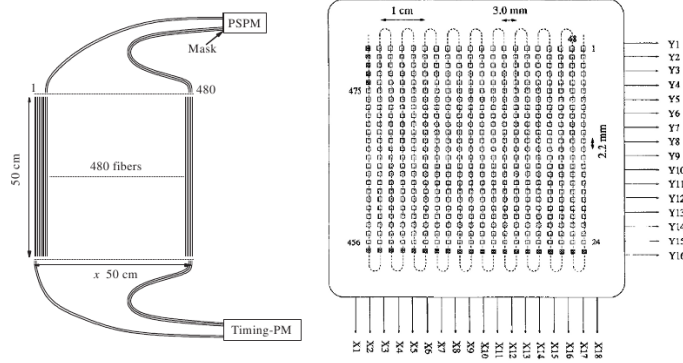


Figure 2.13: Schematic view of the GFI from [63]. The left picture display a scheme of the side of the GFI showing how the fibers and the PMTs are positioned and where the mask is situated. The second picture on the right, is the mask, showing the holes where the fibers are located and the coordinate system for the position correlation. Dark squares indicate unused holes and the relative position of the anode wires are indicated as well.

order to extract the interaction information like time, position and energy loss, calculations have to be done.

The time detected on each paddle are given by the equations 2.5, where T is the absolute time of the interaction and C is the velocity of light in the paddle material.

$$t_1 = T + \frac{s_1}{C} \quad t_2 = T + \frac{s_2}{C} \quad (2.5)$$

Adding the previous equations, the absolute time of the interaction is calculated using the equation 2.6, where L is the length of the paddle and $x_{1,2}$ are the distance the light goes through which are related following $L = x_1 + x_2$. The constants L and C can be treated as offsets for the calibration.

$$T = \frac{t_1 + t_2}{2} - \frac{x_1 + x_2}{2C} = \frac{1}{2}(t_1 + t_2 - \frac{L}{C}) \simeq \frac{1}{2}(t_1 + t_2) \quad (2.6)$$

The position of the interaction can be calculated using the time difference of the signals as shown by the equation 2.7, where λ is the attenuation length.

$$X = \frac{1}{2}[(x_1 - \frac{L}{2}) + (\frac{L}{2} - x_2)] = \frac{C(t_1 - T) - C(t_2 - T)}{2} = \frac{C}{2}(t_1 - t_2) = CT \quad (2.7)$$

2. Experiment & Detector setup

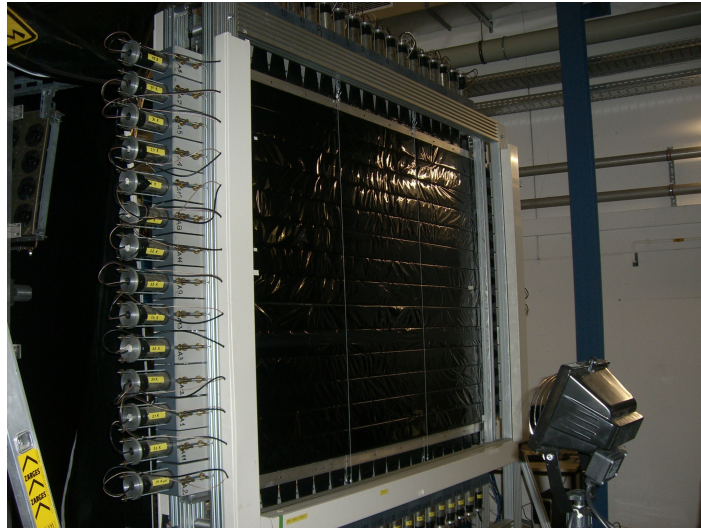


Figure 2.14: TFW picture from the setup of the S393 experiment. It can be seen the 18x14 paddle distribution and the PMTs on both ends of the paddles. The scintillator material is wrapped in black plastic in order to minimize the contamination from outside photons.

For the energy loss, the light attenuation of the paddles has to be taken into account using equations 2.8

$$e_i = E \cdot e^{-\frac{x_i}{\lambda}} \quad i = 1, 2 \quad (2.8)$$

These equations leads us to equation 2.9 where the parameter $e^{\frac{L}{2\lambda}}$ can be taken as a constant and is moved to the gain in the calibration.

$$E = \sqrt{e_1 e_2 \cdot e^{\frac{x_1}{\lambda} + \frac{x_2}{\lambda}}} = \sqrt{e_1 e_2} \cdot e^{\frac{L}{2\lambda}} \simeq \sqrt{e_1 e_2} \quad (2.9)$$

These equations are applied for all the scintillator paddles based detectors of the setup like POS and LAND.

2.3. Cave C: R3B Setup

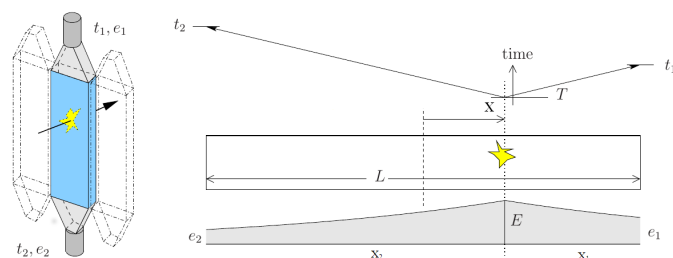


Figure 2.15: Schematic view of a TFW paddle and a drawing of the main interaction points and variables. E , X and T are the energy, position and time of the interaction, L is the longitude of the paddle, $x_{1,2}$ are the distance of the interaction from each PMT, $t_{1,2}$ are the times and $e_{1,2}$ the measured energy. Image taken from [64]

Neutron Branch: LAND

The Large Area Neutron Detector (LAND) [65] is the detector of the neutron branch, located 13 meters away straight ahead of the target center. The full detector is $2 \times 2 \text{ m}^2$ with 1 m depth (see figure 2.16), it was designed to measure time of flight and position of fast neutrons with energies above 150 MeV, giving excellent three momentum resolution.

LAND consists on 200 paddles, each covering an area of $200 \times 10 \text{ cm}^2$ with 10 cm depth. An example paddle can be seen in figure 2.17. Each paddle has a sandwich structure with 11 sheets of iron (the two outer ones are 2.5 mm thick, the others are twice that thickness) and 10 scintillator plastic sheets of 5 mm thickness. The detector is divided in 10 layers, each with 20 paddles. Every layer is perpendicular to the adjacent (see again figure 2.16), in such a way that it is possible to determine the vertical and horizontal position by the detection of the scintillation light. The paddles are equipped with light guides wich direct the light to the PMTs on each side. By the difference in arrival time of the signals, the particle hit position within the paddle is determined. The intrinsic time resolution is 370 ps whereas the position resolution is 5 cm. The efficiency for one neutron detection is around 90%.

Often a VETO detector is setup in front of LAND in order to reject charged particles before reaching the neutron detector, but this was not used in the case of the S393 experiment.

2. Experiment & Detector setup

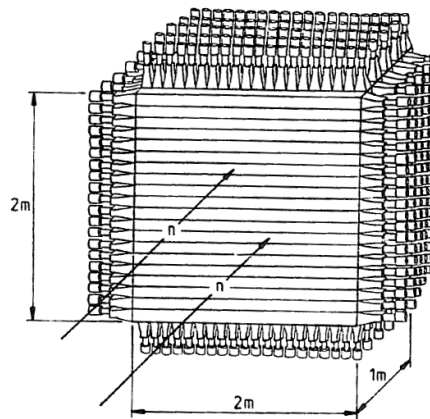


Figure 2.16: Schematic view of the detector. As it is explained in the text, there are 10 layers all of them perpendicular to their adjacent ones, every layer is equipped with 20 paddles of 10 cm width.

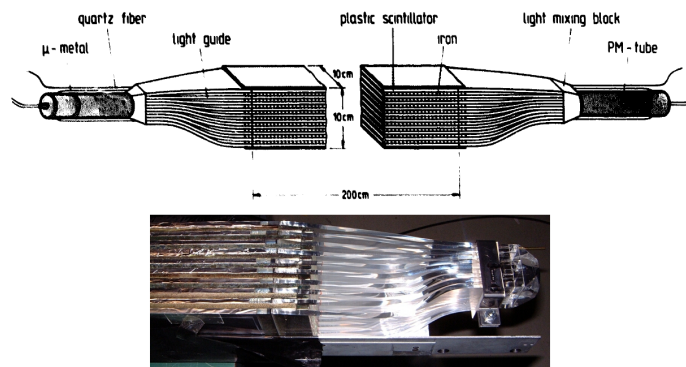


Figure 2.17: On the top there is a scheme of the sandwich structure of one paddle, showing the plastic and iron layers. The bottom picture is a photograph of the sandwich.

“You’ll find truth in your looking glass, not on the tongues of men ”

George RR Martin, *A feast for crows*

3 Detector calibrations

In nuclear physics experiments the data are usually organized on an event-by-event basis. In this context, one event is the set of physical phenomena and detector signals produced within the time window opened when a nuclear reaction with the target fulfill certain conditions. The data acquisition modules produce signals coded as bits that are stored together with the label-channel information that are preceded by the module identification. All these data from every module is packed with a unique identification per event. Thus the collection of thousands of this data packs make up usually the ListMode Data (lmd) files.

The signals produced in the detectors described in the previous chapter are processed and recorded using a Data AcQuisition system (DAQ) known as Multi Branch System (MBS) designed originally by Nicolaus Kurz et al [66]. This framework used at several facilities was developed at GSI. The MBS system access the CPU of the VME and fastbus crates where the different electronics like ADCs and TDCs are situated and transport the data via TCP/IP further up the DAQ line. Furthermore it handles the trigger synchronization of the different detector systems, as well as combining these different data into *events*. As a result the data is saved in several lmd files of sizes close to 1 Gb.

3.1 Introduction to Land02

In the description of the analysis procedure of an R3B experiment it is compulsory to mention land02 [67]. Land02¹ is the software package used by the collaboration for calibration and data analysis of the GSI experiments.

Land02 consists in a group of individual programs that guide the data from the lmd files collected by the acquisition program through the calibration of the

¹It was originally developed by Håkan T. Johansson but it has been extended and supported by a lot of members of the collaboration, primarily by Ralf Plag.

3. Detector calibrations

different detectors in Cave C until the particles are tracked through the setup at the end of the process.

Figure 3.1 shows a flow chart of the stages the data follows under the analysis of an experiment.

- **lmd**

As explained before, the data coming from the data acquisition is compressed in lmd files containing the information delivered by every module per event.

- **raw**

The raw data is here understood as the first step after the unpacking of the lmd file, thus it is the same data but in read-friendly way for a specific analysis program, in this case the ROOT Data Analysis Framework [68].

- **tcal**

This is the first level of calibration of every detector system where an initial internal time-calibration has been performed and the base line of the signal is settled, for instance subtracting the pedestals in the relevant detector channel.

- **sync**

After this second-level of calibration the data starts to reflect the physics. All the time signals are related to a common zero and the corresponding gain is assigned to each energy channel.

- **dhit**

This calibration stage is where the hits on the detector are physically mapped in space using the detector internal coordinate system.

- **hit**

The hit positions are translated to a common unit with the origin usually selected as the center of the detector where the beam goes through in the ideal case of a perfect alignment, therefore the calibration can contain positive as well as negative lengths.

It is important to emphasize that in land02 every detector is finally calibrated using the same units, nano-seconds (ns), centimeters (cm) and Megaelectron Volts (MeV) for time, distance and energy respectively.

- **track**

This is the higher level of data treatment, where the correlation between the different detectors of the setup is settled and some physical values are calculated directly from the combination of them, like the Atomic Mass (A) or the

3.1. Introduction to Land02

Atomic Number (Z) as determined by the Time of Flight and energy loss in the incoming detectors.

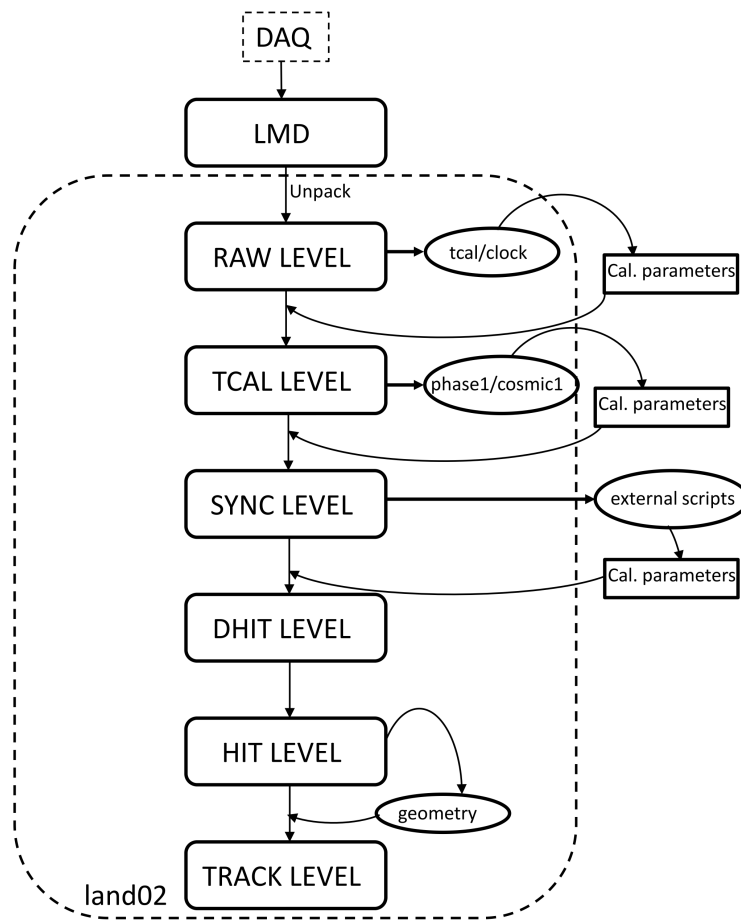


Figure 3.1: Flow chart of the different Land02 data levels (see text for further explanation). The connection between the calibration parameters and the land02 scripts used for calibration is detailed.

3. Detector calibrations

3.2 General remarks about calibrating with land02

The first and most important program to get a good calibration is of course, the unpacker, named *paw.ntuple* in Land02 for historical reasons. It allows to unpack the data in the previously explained calibration levels, reading the parameters and producing calibrated ROOT[68] files ready to be analyzed.

Is important to stress that in an experiment like the S393 which lasts several weeks the calibration parameters can change throughout the experiment due to temperature and humidity variations, also because there were six different fragment separator settings, therefore several parameters associated with specific detectors like the amplification stages had to be adjusted accordingly.

3.3 Triggers

In experimental nuclear physics, a “trigger” is usually a system of logical signals used to activate the data acquisition to record the signals produced within that event. It can be quite simple, from just recording every signal above a certain threshold, to a very complex system that includes several conditions on every detector. Because of the size of the setup and the broad range of research topics to study, in this kind of experiment the trigger system is of the latter kind, allowing to change the priorities according to the beam time and the setting.

The logical signals are combined to produce a trigger pattern (Tpat) which consist in 16 bits of data which is added to every event in order to be able to classify it following the conditions that were fulfilled. Some triggers are fired more often than others, this would lead to an excess of redundant data, that is why it is usual to downscale these triggers, saving data space. As an example, if a trigger is downscaled by 64, one every 64 events meeting that specific trigger conditions, will be recorded.

The S393 experiment used the trigger pattern of table 3.1. The basic Tpat is called “Minimum bias” and fulfills the conditions of “Good Beam” i.e. coincidence of Spill On (incoming spill from the accelerator), a signal in POS and anti-coincidence with a ROLU signal (POS.!ROLU), meaning that a centered beam is coming in. The Good Beam conditions are used very often in coincidence with a signal in the Fragment Wall (TFW), meaning a centered beam reaching the end of the setup, named as Fragment Tpat in table 3.1. All the Tpat with an anti-coincidence with the Spill On signal are used for calibration (cosmic rays). The Id is related with the bit number (n) saved to the lmd file with $Id = 2^{n-1}$.

3.3. Triggers

Id	Tpat \Raw signal	trictl tracer	late-trigger kill	Early pile-up	Spill on	CB L+R	NTF	pix	S8	CB sum delayed	CB sum	CB OR delayed	CB OR	proton wall delayed	proton wall	fragment wall delayed	fragment wall	land cosm	land mult	POS	POS:ROLU
1	Minimum bias Good Beam(CB)				Green																Green
2	Fragment GB + TFW			Red	Green												Green				
4	FRS S8 Hit end FRS				Green			Green	Green												
8	CBSUM Fragment + CB Energy		Red	Red	Green					Green							Green				Green
16	Proton Fragment + DTF			Red	Green									Green							Green
32	GB-pileup Discard Pile-up			Red	Green																Green
64	Pix GB + pix for calibration				Green			Green													Green
128	Neutron GB + TFW + hit in LAND			Red	Green												Green				Green
256	CB muon No Beam + CB high energy				Green					Green											Green
512	Land Cosm No Beam + hit in LAND				Green													Green			Green
1024	TFW Cosm No Beam + TFW				Green																Green
2048	CB Gamma No Beam + CB				Green							Green									Green
4096	DTF Cosm No Beam + DTF				Green																Green
8192	NTF Cosm No Beam + NTF				Green																Green
16384	CB L+R muon No Beam + CB both sides				Green	Green															Green

Table 3.1: Relationship between the raw trigger signals (horizontal order) and the trigger patterns (vertical order) in the S393 experiment. The green squares means a coincidence signal and red squares an anti-coincidence signal.

3. Detector calibrations

3.4 Raw → TCAL

Most of the detectors have a QDC (Charge to Digital Converter) at the end of their electronic chain. Whenever the timing gate is open the voltage on an internal capacitor is integrated to produce a digital value that is recorded. This capacitor is charged by the signal from the detector and a small current supplied by the QDC, thus the read value will always have a certain off-set produced by the module called Pedestal. In order to go from the raw level to the TCAL pedestals must be subtracted. Land02 has a script called *clock* which goes through off-spill data looking for a certain time trigger (clock) coming at regular intervals. The recurrent size of the signal in these kind of events is subtracted in each channel. The Crystal Ball modules are different and instead of using the *clock* program, the pedestals are calculated in a calibration run with a standard radioactive source. As a result of this calibration, all channels within a detector have the same base line (zero) value.

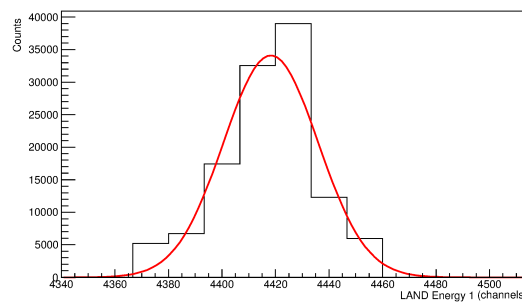


Figure 3.2: Standard pedestal fitted by the *clock* program on one of the PMTs signals from LAND. Looking at the coincidences with the clock trigger signal the pedestal signal position that must be subtracted is obtained. It is fitted to a Gaussian function to get the mean position value.

Also the time calibration within the detector is performed at this level. The TDC’s (Time to Digital Converter) have a certain gain value which can change along the time of the experiment, thus it has to be measured at different moments using a time calibration module. This module sends two delayed signals, one to the DAQ and another to all the electronic channels, hence recording such events allows us to keep on check the gain of each module. *tcal* program in Land02 goes over the raw data and produce a correction factor for the time signal. This calibration correlates all times between the detectors and in the common unit of nano-seconds, although every detector time is still uncorrelated with the global time of the setup. Further information can be found in [69][70].

3.5. Incoming beam identification calibration

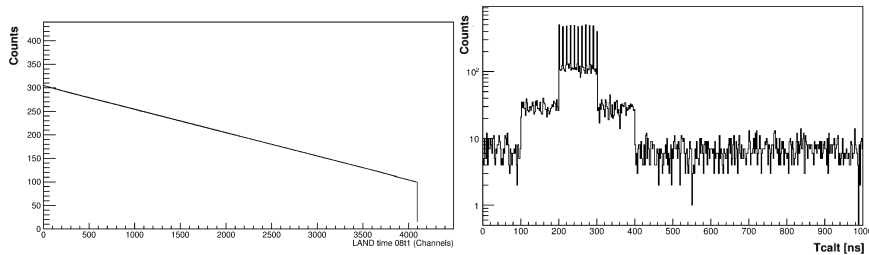


Figure 3.3: *Left:* Standard calibration plot of the *tcal* program. The correlation of the *tcal* time with the time measurements from one LAND PMT can be seen. *Right:* Typical output from the time calibrator. It has to cover the TDC range of all detectors that require calibration.

3.5 Incoming beam identification calibration

What is usually understood as the “incoming” detectors consist in the PSP, POS and S8 (see section 2.3.1). These detectors give Particle IDentification by charge and time of flight measurement of the incoming beam.

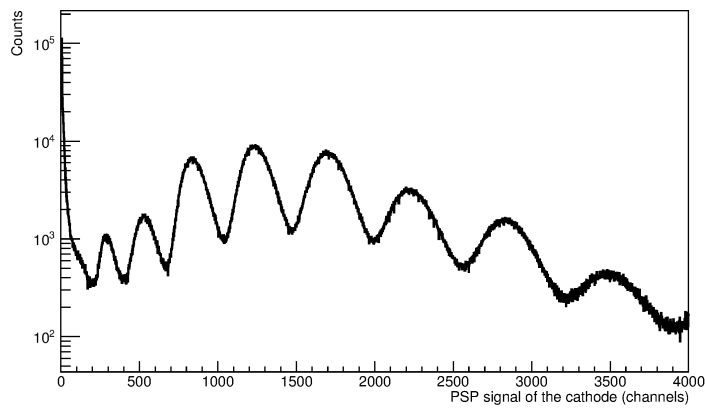


Figure 3.4: Different energy loss deposition in PSP detector of nuclei with different Z . Each peak is fitted to a Gaussian function to get a mean for the value of the energy loss for every isotope (which can be correlated to a certain charge Z).

3. Detector calibrations

The PSP usually provides energy loss and position information. Unfortunately the latter was not possible in the S393 experiment due to the lack of calibration runs (called “Pixel runs”). This kind of detector requires the use of an active mask with a grid of hundreds of small square pixels that allows to have a reference for position calibration, but the amount of data with the pixel mask on was too low. The PSP have certain position dependency of the energy deposition, that could not be corrected due to the lack of statistics, however the resolution of the mass-to-charge ratio is enough for a good separation of the incoming beam.

The energy loss is provided by the cathode in the detector that can be calibrated using several different ions (different energy losses) by fitting the data to Gaussian (see figure 3.4). The energy values corresponding to each curve can be estimated using ATIMA [71] (or similar program). The channel and the energy loss values are correlated using a linear fit, providing slope and offset as parameters. Therefore each channel is directly related to a certain energy loss value, which corresponds to a certain charge Z .

The scintillators S8 and POS, provide the time of flight for the ion identification.

$$\beta = \frac{\Delta X_{FlightPath}}{c \cdot ToF} \quad (3.1)$$

Equation 3.1 shows the relationship between the beta (β), flight path ($\Delta X_{FlightPath}$) and Time of Flight (ToF) of an isotope. The equation 3.2 is the time difference between S8 and POS which is the result of the time of flight and the electronics involved.

$$\Delta T = ToF + T_{offset} \quad (3.2)$$

Combining these equations results in equation 3.3, thus making a linear fit of the time difference (ΔT) against the velocity (β), it is obtained the time offset and the flightpath which is considered as a parameter of the fit. The velocity of the incoming isotopes can be calculated from the beam energy using the SHARP calculator [72].

$$\beta \cdot \Delta T = \frac{\Delta X_{FlightPath}}{c} + \beta \cdot T_{offset} \quad (3.3)$$

Once the charge and the flight path are calibrated, it must be related to the mass-to-charge ratio for particle identification. This is done with the equation 3.4, calculating the $B\rho$ with the SHARP calculator. The result can be seen in figure 3.5.

$$\frac{A}{Z} = K \cdot \frac{B\rho}{\beta\gamma} \quad (3.4)$$

3.6. Calibration of the detectors around the target

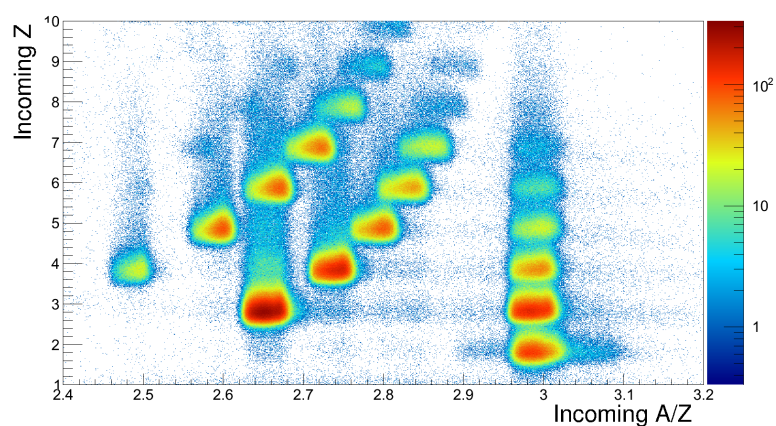


Figure 3.5: Example of Particle Identification for the setting 5. The Y axis holds the charge(Z) of the incoming nuclei whereas the X axis represents the mass/charge (A/Z) ratio of that nuclei.

3.6 Calibration of the detectors around the target

3.6.1 Double Sided Silicon Strip Detectors (DSSDs)

Due to the importance of measuring the outgoing angle of the fragment, the position calibration of the Double Sided Silicon Strip Detectors (DSSDs) is crucial in this research. The calibration from the TCAL level to the HIT level has been performed with some routines made by Valerii Panin and Matthias Holl, hence a more detailed explanation can be found in their respective Thesis [50][51]. This calibration is charge dependent, thus the Z of the isotope of interest must be previously selected by the incoming detectors, and an empty run or the non-reaction part of the beam has to be used in order to calibrate the silicons located after the target.

The energy signal of a particle punching through the DSSD is shared over several neighbour strips. A Carbon nucleus activate on average 5.4 strips on the K-Side and 8.3 on the S-Side. Therefore the positions and energy of these detectors is driven by clusters of neighbouring strips with signals over a certain threshold.

In order to assign a position to a cluster, it is calculated using a center-of-gravity approach, weighting with the energy signal in every strip,

3. Detector calibrations

$$X_{cog} = \frac{\sum_i^k E_i n_i}{\sum_i^k E_i}. \quad (3.5)$$

In the equation 3.5 n_i is the strip number and E_i the energy signal, and the sum goes through all the strips of the cluster $\{i...k\}$. That determination of the position within a cluster permits to calculate a position in the detector with the equation 3.6,

$$X = P \cdot X_{cog} \quad (3.6)$$

Where P is the value of the readout pitch size, $110\mu\text{m}$ and $104\mu\text{m}$ for the S-Side and the K-Side.

This method produces positions distributions with obvious patterns favouring the positions of the strips in the center of the clusters. This affect no only to the measured positions but the energy as well. In order to avoid this effect, an impact parameter η is defined (see equation 3.7) to represent the inter-strip signal distribution. The $Integer(X_{cog})$ value usually is the number of the central strip of the cluster, therefore if $\eta=0$ the hit is in the central strip, while with $\eta=1$ is in the next strip with a readout. Hence this parameter allow us to represent the inter-strip area for both S- and K-side of the DSSD.

$$\eta = X_{cog} - Integer(X_{cog}) \quad (3.7)$$

In order to correct the position to have a continuous distribution in the inter-strip region the distribution of the η parameter must be integrated using the equation 3.8,

$$X_N = Integer(X_{cog}) + P \int_0^k f(\eta) d\eta. \quad (3.8)$$

The change from a pre-smoothing of the η parameter to the result after the integration can be seen in figure 3.6.

Every broken or wrongly coupled strip will continuously fire a signal or not deliver it, thus the strip has to be flagged as “dead” and not included in the calibration in order to avoid miss-identification of the clusters.

After the position calibration is finished, a similar approach has to be followed in order to correct for the gainmatching of the clusters. The gain in every strip is different, so every cluster energy-distribution is divided in three bins and fitted to a Gaussian function for correction. The energy is also gainmatched to a certain value thus all the clusters within a K-side/S-side have the same energy value.

3.6. Calibration of the detectors around the target

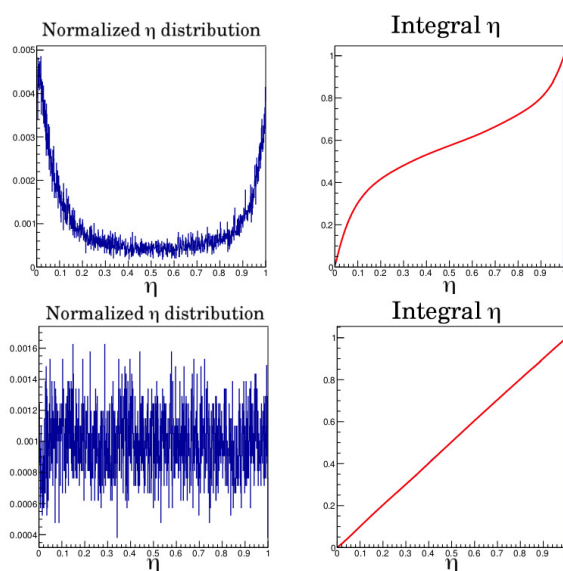


Figure 3.6: (a) η Distribution before calibration. It can be seen that the values where η is close to 0 and 1 are clearly favoured because is where the real strips readout are located. (b) Result after the integration, the distribution is continuous and smooth. Is important to notice the very small range of the Y axis in the left plot, it is showing a very flat η distribution.

The energy resolution obtained in this experiment for the case of Boron was around 7%.

3.6.2 Crystal Ball (XB)

The calibration of the Crystal Ball is divided in two separate branches, due to the fact that the pulses coming from the forward crystals are split in two signals for different amplification stages in order to fulfill the different dynamic ranges of gamma rays and protons.

Gamma branch

Along the experiments we took advantage of the beam stops to make calibration runs with sources (see table 3.2) which are used to perform the energy cal-

3. Detector calibrations

Source	Calibration peaks
^{60}Co	1173 keV
	1332 keV
^{22}Na	511 keV
	1275 keV
^{56}Co	2598 keV
	3253 keV

Table 3.2: The three different standard sources used for the calibration. ^{60}Co and ^{22}Na sources were used in the S393 experiment but the ^{56}Co was used in the experiment S389 that followed directly after the S393 and was using the same setup. For the ^{56}Co is only detailed the used peaks.

ibration of the gamma branch. F. Wamers [49] developed several useful scripts to help in the process. To produce the energy calibration consists in identifying the peaks of each source (see figure 3.7) and making a linear fit to correlate the channels with the energies (see figure 3.8). Due to the fact that along the experiment the sources used were ^{60}Co and ^{22}Na the calibration is only reliable over a small region, thus it is complemented with the source ^{56}Co of the S389 experiment, carried out in October 2010 just after the S393. The prompt reaction gammas suffers an important Doppler correction due to the high beam energies, the consequence of this are the very different amplitude gains, determined by their position in the sphere. The most forward angles receive much higher energies than the backwards (see figure 3.9).

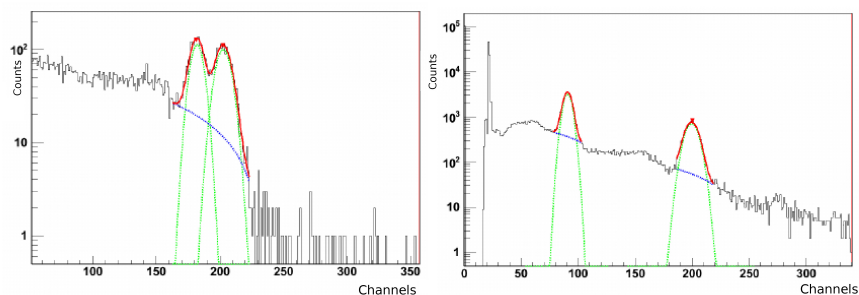


Figure 3.7: Calibration peaks for the crystal 42. (a) Using ^{60}Co the energies are at 1173 and 1332 keV (b) Using ^{22}Na the energies are at 511 and 1275 keV.

3.6. Calibration of the detectors around the target

At the beginning of the analysis I developed my own gamma calibration using the two sources of the S393 experiment as it was reported in my Master Thesis [73]. Later on I have used the calibration performed by R.Thies for the experiment. The efficiency calibration of the detector is used in order to measure cross-sections, as it is not need in this work it was not included, although more information can be found in reference [62].

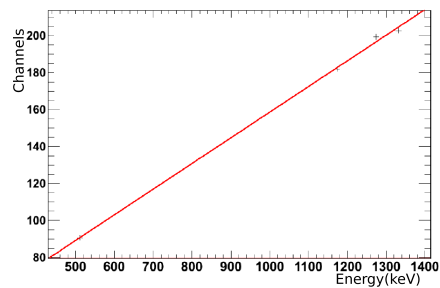


Figure 3.8: Linear fit to correlate channels with energy for the Crystal Ball

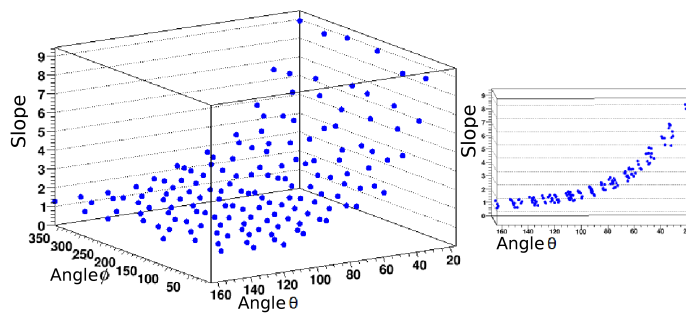


Figure 3.9: Calibration slope (KeV/ch) against the crystals angles. The slope grows when θ go down, because the scintillators in the forward angles will measure the highest energies. The electronic amplification is higher for the scintillators with angles closer to 180° due to their lower dynamic range.

3. Detector calibrations

Addback and Doppler correction for the gamma branch

Gamma rays have an important probability of leaving their energy in several Crystal Ball detectors, hence is needed to take into account this possibility and include an Addback algorithm to improve the detection efficiency. The algorithm used is the “closer-neighbours algorithm”(see figure 3.10), there are other several options, but none of them have proven to be better[74].

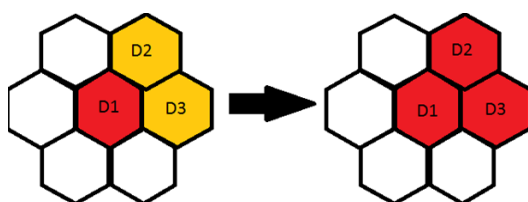


Figure 3.10: Closer-neighbour algorithm. After sorting and ordering the crystals by the energy in an event, starting with the highest (D1), the energy deposited in the surrounding crystals is added making a cluster. All crystals of the cluster are taken away from the crystal lists, and starts again with the following. The angle used for the Doppler correction is from the detector which starts the cluster.

The last step before being able to analyze the gamma data from the Crystal Ball is applying a Doppler correction to every event in each crystal. It is determined by the equation 3.9, where β is the ratio of the isotope velocity in middle of the target and the light speed, γ is the Lorentz factor and $\theta_{crystal}$ angle is from the cluster. This correction can be applied after the DHIT calibration level.

$$E_{CM} = E_{lab} \cdot \gamma(1 - \beta \cdot \cos\theta_{crystal}) \quad (3.9)$$

Due to the Doppler boost the gamma energies can reach up to 15 MeV but the source peaks used in the calibration are at 2.5 MeV maximum, thus the calibration procedure could be largely improved.

Proton branch

This branch is crucial for the detection of the knock-out protons from the (p, 2p) reaction. The calibration was performed by Ronja Thies [62].

Muons and protons have very similar masses and the same absolute charge, therefore they have a similar energy deposition, thus this calibration is performed using cosmic muons from the atmosphere. A land02 program named *gamma2* is used to look for two different kinds of trajectories: (a) Across two opposite crystals and (b) Crossing the shell, going through several crystals. The atmospheric

3.7. Calibration of the outgoing fragments detectors

muons have enormous energies, hence as charged particles are in the low-loss energy regime (not reaching the Bragg peak), the simulations [49] shows that in the (a) case you are sure of the direction so the muon goes through the full length of two crystals leading to an energy loss of 90 MeV, whereas for the (b) case the muon traverse sideways through the shell leading to 45 MeV energy deposit.

Using both different kinds of flight paths and their different energy loss, a linear fit is performed to correlate the channels and the energies of the 64 crystals with high energy regime in the PMTs. More information can be found in [75].

Time calibration

The internal time calibration in Crystal Ball uses the *gamma2* script as well. Event by event, it looks for two crystals that have detected the full energy of the two peaks from the sources ^{22}Na or ^{60}Co in the same event, as these gamma ray pairs can be considered to be emitted at the same time, they are used to calibrate the time difference of the crystals. After collecting a considerable amount of statistics this time difference is fitted to a Gaussian curve in order to obtain a mean time difference. The obtained data is used to solve an equation system to get a time offset for every crystal such as all summed give zero. These offset provide the time correlation between all crystals times, afterwards the Crystal Ball is correlated with the full detector setup.

3.7 Calibration of the outgoing fragments detectors

3.7.1 Fiber Detectors (GFI)

In order to calibrate the GFI it is needed to perform a *sweep run*, in this kind of run the target is empty and the magnet current is changed continuously to illuminate the full area of the outgoing detectors. The GFIs are used to track the masses of the outgoing fragments, thus the energy loss is not necessary but the position, although due to the different gains of the anode wires is mandatory to gainmatch them before the position calibration. There are 34 wires, 18 in the horizontal direction (u) and 16 in the vertical direction (v). An isotope hitting the GFI produces scintillation light which is guided through the fibers to the Position-Sensitive-Photomultiplier (PSPM), generating electrical signals in around seven anode wires. Fitting the distribution to a function gives the gainmatching parameters (see figure 3.11). As the process includes resolving an equation system which starts from the best previous fit, it should be repeated usually around three times to get stable parameters (see figure 3.12).

The position calibration needs to correlate every fiber with a position in the PSPM coordinate system (u,v). To project the fiber signals into this coordinates, a two-dimensional histogram is used. Every cluster is fitted to a Gaussian distribution

3. Detector calibrations

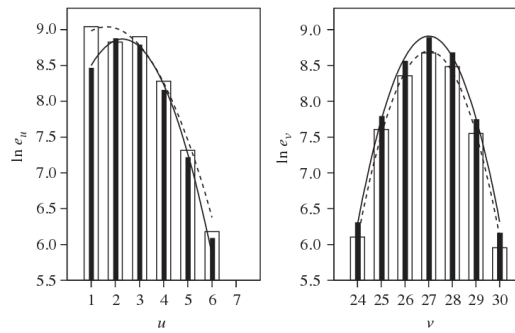


Figure 3.11: Example of charge distribution in the anode wires. The open and filled vertical bars are the electrical signal of each wire before and after gainmatching. The dotted and filled line are the fit functions, before and after gainmatching. Taken from [63].

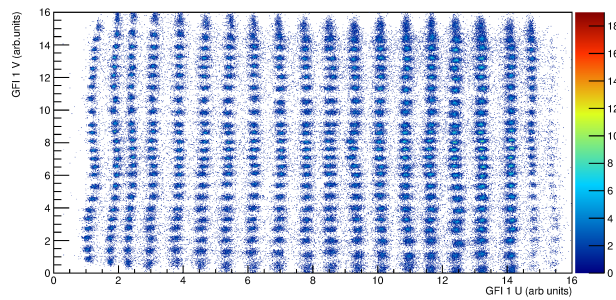


Figure 3.12: Calibration result of the GFI. Every point clusters represents one fiber, three iterations of gainmatching has been performed. All the clusters as well as the fiber mask boundary is good resolved and defined.

to provide a mean value (and the associated deviation) for the cluster position in the wires coordinate system. The next step is determining their neighbours which is done using the angles and lengths of the vectors of the grid, indexing this data to produce a grid which relates the fibers with their PSPM coordinates and the position of fiber in the detector (x). This grid easily assign signals to positions if the hit is within the width of a fiber (cluster), in such a case that a hit signal is between

3.7. Calibration of the outgoing fragments detectors

clusters, the probability of belong to one of them is calculated assigning different weights and including a randomization. For further details about the calibration see [63].

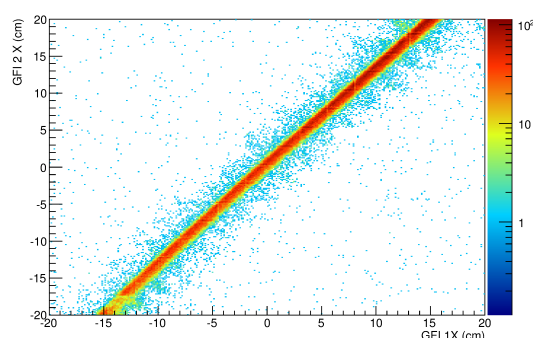


Figure 3.13: Correlation between the two GFI detectors in the experiment that were separated by 150 cm. Good correlation between the GFI 1 and GFI 2 is indicated by a straight line close to 45° and is a signature of good position resolution.

3.7.2 Time-of-Flight-Walls (TFW)

After have run the *clock* and *tcal* codes in order to reach the TCAL level, running the script *phase1* will gainmatch the PMT signals within the paddles and correct the time.

One goal is to synchronize the energy and time within every paddle, gathering an amount of “clean” data, just hitting one paddle in each plane, avoiding ambiguities. The data collected in each paddle is fitted such as the offset is zero in the middle. This produces the gainmatching for the energy and an offset for the time, as well as the speed of light within the paddle that is also needed for the position calculation.

In this kind of detector, there are two layers of scintillators, one to measure the Y direction and a second one the X direction, therefore there will be a small time and energy deviation between X - Y planes. As this difference in energy loss between them is negligible at this beam velocities, we can consider it to be equal. In the same way, the distance between the two layers is 1 cm, thus the time of flight difference is also insignificant in this case. Consequently, the other goal in the calibration is to synchronize the X and Y plane in order to have the same time signal and energy loss, producing a gain for the energy and an offset for the time.

3. Detector calibrations

Once the internal calibration of the detector is finished, correlate the measured energy and time with the real energy loss and the time of flight with the setup. Using such a program like ATIMA [71] it is possible to calculate the time of flight from the target and the energy loss of a chosen isotope upon reaching the TFW. These values are correlated to the mean values from previous steps of the calibration.

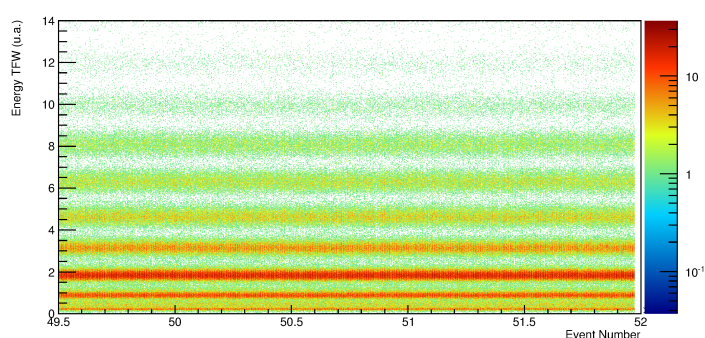


Figure 3.14: Time of flight wall after calibration. The different offsets in the gains of the energies have been match to have a smooth energy distribution over the events.

3.7.3 LAND

Calibrating LAND is very similar to calibrating the TFW, the neutron detector consists on several planes of sandwiched iron with plastic scintillator. Therefore, the procedure is similar, the energy signals within the paddle must be gain-matched as well as the time signals need to be shifted to obtain a zero in the middle of the paddle. This calibration is performed using the script *cosmic1*, which uses cosmic muons like in the Crystal ball proton calibration. The useful events are particles coming from above with such a high energy to go through several scintillator planes. Obviously, is also required to synchronize the signals between the different planes.

In order to synchronize the time stamp of the detector with the time stamp of the full experimental setup, the gammas coming from reactions are used. Gamma rays travel with the same velocity (c), hence a certain peak at higher velocities than anything else can be easily find and used as a reference to complete the calibration (see figure 3.15).

3.8. Tracker

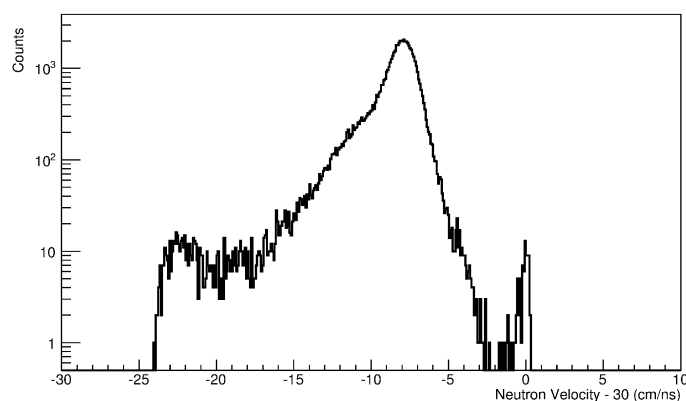


Figure 3.15: The gamma rays peak is at the right-most part of figure. It is already calibrated to a velocity of 30 cm/ns.

3.8 Tracker

In order to complement land02, R.Plug has developed a tool[76] to track the particles, simply named *tracker*. The main objective of this is to have a good determination of the different masses of the isotopes after the reaction. The program uses root files with unpacked data at HIT or TRACK level (see section 3.1), and produces a new root file, similar to the previous but with several new leaves.

The tracker approximates the trajectories of the different isotopes and fragments using several parameters as an input and extracts the masses of this isotopes thanks to the previously mentioned equation 3.4. To calculate the trajectory it is necessary to know the ALADIN magnetic field. There is a mapping that relates the field with the current of the magnet, therefore providing the current used in a certain run allows the tracker to use the right value of B . The velocity is obtained from the Time of Flight (using TFW) and the flightpath with the corresponding energy loss of the fragment in every detector calculated with the Bethe-Bloch equation (equation 2.2). The charge must be specified too. The trajectories are determined using hits in the DSSD, the GFIs in the X direction and the TFW (mainly in the Y direction). The program can work in three different modes: forward tracking which needs two detectors before ALADIN and one after (DSSDs + GFI), backward tracking using two detectors after the magnet and one before (DSSD + GFIs) and mixed mode that uses two detectors in both sides of the setup. The most used method in this analysis was forward tracking. In this approach, the program calculates a track with fixed posi-

3. Detector calibrations

tions in two detectors before the magnet (DSSDs), presuming a mass and an initial velocity, it minimizes the trajectory changing the mass accordingly and correcting the β with the different energy loss.

The position of the detectors must be given and calibrated using empty runs or non-reacting beam, and once certain positions are determined, the ToF from the target to the TFW must be calibrated as well. The calibrations are basically performed by comparing the calculated tracks with the “real tracks”(hit positions) until reaching differences within the detector resolution limits.

The program has additional features, like tracking the protons through the proton branch which has not been used in this analysis. It is capable of tracking the incoming isotopes with the two DSSDs before the target and POS, although this has several problems in the S393 experiment because of the problems with the first silicon. The code tracker also calculates the Doppler correction using the β of the fragment (see section 3.6.2).

**“...no matter how many instances of white swans we may have observed,
this does not justify the conclusion that all swans are white.”**

Karl Popper, The logic of scientific discovery

4 Analysis

In the previous chapters I was explaining the experimental setup used to study the nucleus of interest as well as the methods required to understand the detectors. In this chapter I will explain the techniques used for extracting the physical significance of the dataset from the S393 experiment.

The main goal of this research work is to probe the nuclear structure of the unbound nuclei ^{13}Be using the reaction $^{14}\text{B}(p,2p)^{13}\text{Be}$. The analysis includes several steps. The first one is the identification and separation of the incoming isotope of interest ^{14}B . Secondly to select the right outgoing channel: $^{12}\text{Be} + \text{neutron}$ which is the result of the break up of the unbound nucleus ^{13}Be . Determining the angle between these two components as well as their velocities provides us with the information required to produce a relative energy spectrum which gives insight to the system they composed before: ^{13}Be . Such a spectrum must be interpreted via fitting to Breit-Wigner functions, the basis will be explained in this chapter, whereas the results will be discussed in chapter 5. The fragment ^{12}Be can be emitted with an internal excitation energy, knowing this information will help to know the previous state of the ^{13}Be , therefore looking for gamma rays from ^{12}Be is the third step. The last step is looking for the two protons product of the (p, 2p) reaction to complete the analysis.

4.1 Incoming isotope identification

From the interaction between one nucleus of ^{40}Ar of the primary beam and the production target a broad variety of isotopes can emerge (see section 1.2). The purpose of the fragment separator is to select a certain range of isotopes of interest within the cocktail produced in the reaction with the primary target (see section 2.2.4), nevertheless an extensive variety of nuclei reach Cave C. As explained in the previous chapters, the PSP, S8 and POS are used to select the incoming nuclei.

4. Analysis

The interesting projectile for this work is the nucleus ^{14}B that is present in three different FRS settings of the experiment S393, i.e., optimized to three distinct $\frac{A}{Z}$ ratios. Figure 4.1 is the isotope identification of the summed runs used for this analysis, the useful data is from two settings, the third has too low statistics of ^{14}B .

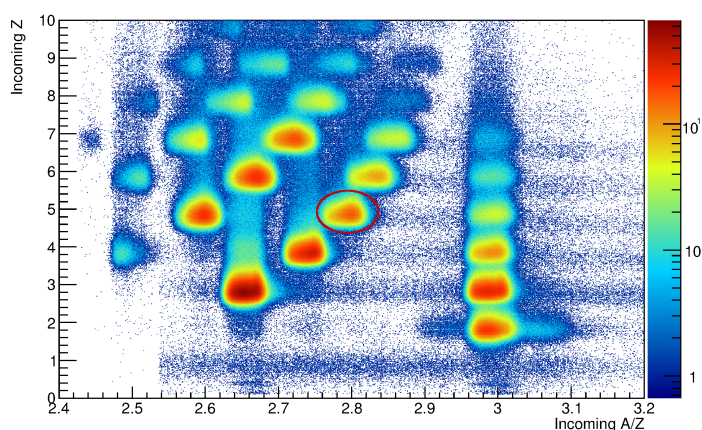


Figure 4.1: Fragment identification of the data files included in this analysis. The Y axis is the charge (Z) of the incoming isotopes whereas the X axis is the mass/charge (A/Z) ratio of them. This plot required TPat 2, i.e., Minimum bias and fragment trigger. The plot includes data from two different settings (4 and 5) which have data of $\frac{A}{Z} \simeq 2.8$ corresponding to the nucleus $^{14}_5\text{B}$, which is the interesting incoming channel for this research work, therefore it must be gated on the corresponding blob, indicated by the red ellipse.

4.2 Detector alignment

In order to obtain the angle between the outgoing particles, all detectors involved have to be properly aligned, as will be explained in section 4.4. DSSD and LAND are the detectors used to measure the incoming and scattering angles of the particles outgoing from the reaction.

4.3. Fragment and neutron selection

At the end of the experiment, photographs of the experimental setup were taken in order to perform a photogrammetric measurement which determine the detector positions very precisely, this provides the data needed for an alignment later on. In order to take pictures inside of the Silicon Box (where the DSSD are located) they have to be taken at close distance by, therefore the accuracy reached for the DSSDs relative position by this method was $400\mu\text{m}$, better than for the other detectors. Further details about the method used can be found in [77].

A good position resolution does not guarantee that the origin of coordinates of the four silicon detectors is well aligned. This was achieved fitting the coordinates of the silicons 2-3-4 to a straight-line, using data from empty runs (unreacted beam). The procedure minimizes the trajectories with three parameters, the coordinate X and Y and a rotation with the beam axis. The first silicon position was corrected by projecting the results to this detector.

Once the DSSDs are fixed to a common origin of coordinates, the alignment with the LAND detector is checked. Although the position of the center of LAND and the target with respect to the beam-axis is known with precision, a certain miss-alignment was found, which was considered as a small angle deviation of the DSSDs target ground plate. This was discovered by projecting the position distribution of incoming nuclei on LAND and comparing with neutron distributions. The deviation was corrected for applying a certain rotation correction reflected in X and Y offsets. A detailed explanation of the procedure is available in [77]. The uncertainty of the method ended up being dominated by the internal resolution of the DSSDs.

4.3 Fragment and neutron selection

^{13}Be is a resonant unbound nucleus and thus its half-life is around 10^{-21} seconds according to [78]. Such a small half-life results in a mean distance traveled before decay of around $D_{decay} = c \cdot \beta \cdot \frac{t_{1/2}}{\ln(2)} \simeq 1.5 \cdot 10^{-11} \text{cm}$, using $\beta \simeq 0.7$. The ^{13}Be will thus not reach any detector, forcing us to look for the ^{12}Be and the emitted neutron.

There are two steps to follow in order to find the fragment $^4_{12}\text{Be}$, to select the charge ($Z=4$) and the mass ($A=12$). The first detectors involved in the charge measurement after the reaction are the Double Sided Silicon Detectors (DSSD), the energy loss in them is directly related to the charge of the fragment. Nevertheless the fragments produced in the reaction are unstable and they have a chance to disintegrate before reaching the end of the fragment branch. In order to guarantee their integrity the selection must be done in coincidence with the energy loss in the Time of Flight Wall (TFW) (see figure 4.2).

4. Analysis

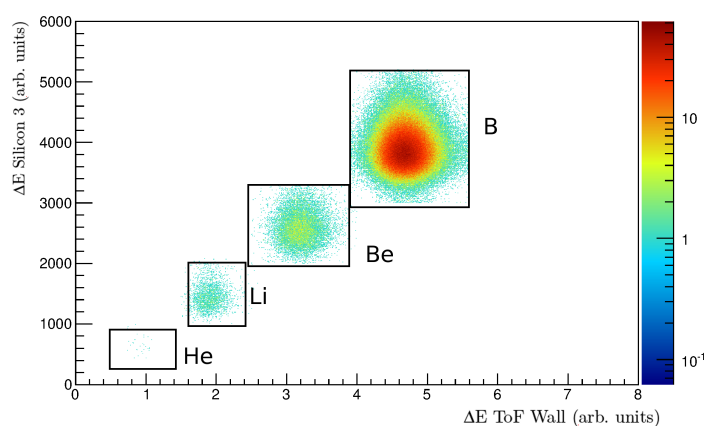


Figure 4.2: Charge identification plot, showing the energy loss in the first silicon after the target against the energy loss in the time of flight wall. The biggest blob is the unreacted beam, i.e. Boron, thus the second blob is the Beryllium, including ${}^4_2\text{Be}$, which is the main interest of this research work.

The second step is to produce a mass spectrum (see figure 4.3), which includes the *tracker* (see section 3.8). Using the forward-tracking mode, the positions of the silicons after the target are fixed and the tracks are minimized using the GFI(x) and the TFW(y) position.

In coincidence with the previous charge and mass selection, one neutron must be detected in LAND. Finding this nucleon is mandatory in order to produce a relative energy spectrum of ${}^{13}\text{Be}$. There exists the option of making the coincidence including events with several neutrons detected, despite these kind of events were not many, it was decided to keep the most restricting option in order to obtain a clean energy spectrum. The neutron velocity was constrained to be between 15 - 25 cm/ns in order to discard from the gamma ray and slow neutron background in LAND (as was showed in section 3.7.3) which are unlikely to come from the ${}^{13}\text{Be}$ production.

4.4. Invariant mass and relative energy

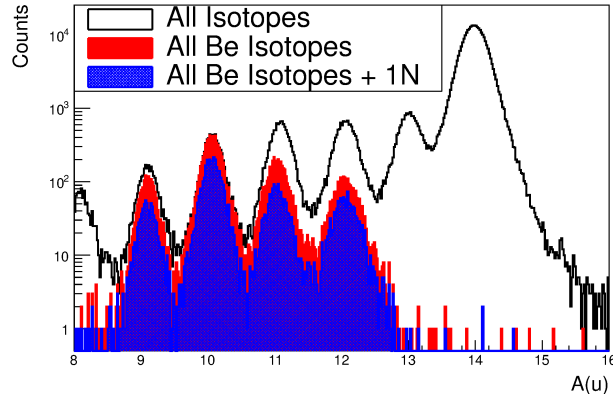


Figure 4.3: Overlap of three different mass spectrum following tracking. *White*: Selection of the incoming beam as ^{14}B . *Red*: Selected ^{14}B as incoming and Be as outgoing. *Blue*: Selected ^{14}B as incoming and Be as outgoing in coincidence with one neutron in LAND. The selection of the charge $Z=4$ makes the masses $A=14,13$ to disappear, which is coherent with the production of Beryllium from Boron in a $(p, 2p)$ reaction and the unbound nature of the ^{13}Be .

4.4 Invariant mass and relative energy

In this work dedicated to the investigation of the nuclear structure of ^{13}Be , we are going to use the invariant mass method [30] to obtain the relative energy spectrum of the ^{12}Be as well as of the outgoing neutron. The invariant mass method has been used before by the R3B Collaboration in several research works like [50] and [79].

This method is founded in the fact that the Minkowski norm of the four-momentum of the physical system is a Lorentz invariant,

$$\mathbf{P} = \begin{pmatrix} P^0 \\ P^1 \\ P^2 \\ P^3 \end{pmatrix} = \begin{pmatrix} \frac{E}{c} \\ p_x \\ p_y \\ p_z \end{pmatrix} \quad (4.1)$$

which is related to the sum of the masses of the system [80] according with:

4. Analysis

$$\|\mathbf{P}\|^2 = \left(\sum_i P_i \right)^2 = M_{inv}^2 \cdot c^2 \quad (4.2)$$

Further development of equation 4.2 leads to 4.3 :

$$M_{inv} = \sqrt{\sum_i m_i^2 + \sum_{i \neq j} \frac{E_i \cdot E_j}{c^4} - \sum_{i \neq j} \frac{p_i \cdot p_j}{c^2} \cdot \cos\theta_{ij}} \quad (4.3)$$

The equations 4.4 and 4.5 are introduced from the Special Relativity to produce the equation 4.6

$$E_i = \gamma_i \cdot m_i \cdot c^2 \quad (4.4)$$

$$p_i = \gamma_i \cdot m_i \cdot \beta_i \cdot c \quad (4.5)$$

$$M_{inv} = \sqrt{\sum_i m_i^2 + \sum_{i \neq j} m_i \cdot m_j \gamma_i \cdot \gamma_j (1 - \beta_i \cdot \beta_j \cdot \cos\theta_{ij})} \quad (4.6)$$

The invariant mass of a system is the sum of the rest masses of the components and the relative energy between them after break up:

$$M_{inv} \cdot c^2 = E_{rel} + \sum_i m_i \cdot c^2 \quad (4.7)$$

Including the previous invariant mass result of equation 4.6 into 4.7 gives equation 4.8,

$$E_{rel} = \left(\sqrt{\sum_i m_i^2 + \sum_{i \neq j} m_i m_j \gamma_i \gamma_j (1 - \beta_i \beta_j \cos\theta_{ij})} - \sum_i m_i \right) c^2 \quad (4.8)$$

If applied to the case of $^{14}\text{B}(p,2p)^{13}\text{Be}$, we get the relative energy expressed as,

$$E_{rel} = \left(\sqrt{m_{^{12}\text{Be}}^2 + m_n^2 + m_{^{12}\text{Be}} m_n \gamma_{^{12}\text{Be}} \gamma_n (1 - \beta_{^{12}\text{Be}} \beta_n \cos\theta_{^{12}\text{Be}+n})} - m_{^{12}\text{Be}} - m_n \right) c^2. \quad (4.9)$$

From equation 4.9 one can deduce the observables to perform the analysis:

4.4. Invariant mass and relative energy

- θ_{12Be+n}

The opening angle between the outgoing fragment ^{12}Be and the neutron. This parameter can be determined combining the data from the DSSDs and LAND respectively. The figure 4.4 shows the angle distribution of the reconstructed ^{13}Be .

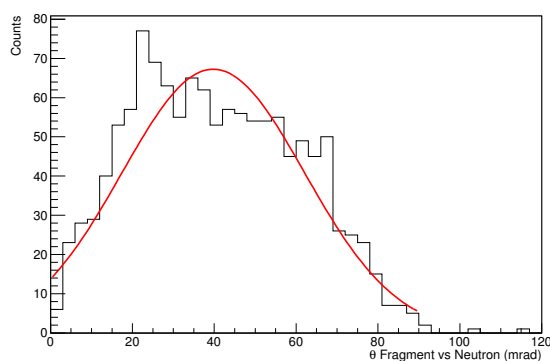


Figure 4.4: The angular distribution between the outgoing neutron and the ^{12}Be . It has been fitted to a Gaussian distribution with a mean value of $\theta_{12Be+n} = 39.76 \pm 0.74$ mrad.

- β & γ

The velocity of the outgoing products (fragment and neutron) is related to the β and γ parameters. These are measured using the TFW and LAND, corrected by the tracker. Both velocity distributions are in figures 4.5 and 4.6, the latter shows that there is an appreciable difference between the distribution of fragment-velocity in each FRS setting.

4. Analysis

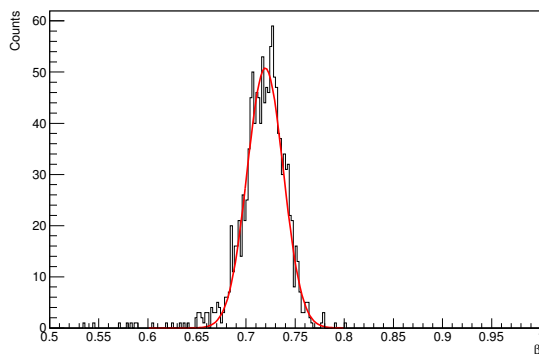


Figure 4.5: β of the outgoing neutron after break up. A fit using a Gaussian distribution has been applied, giving a value of $\beta_n=0.72\pm 0.02$

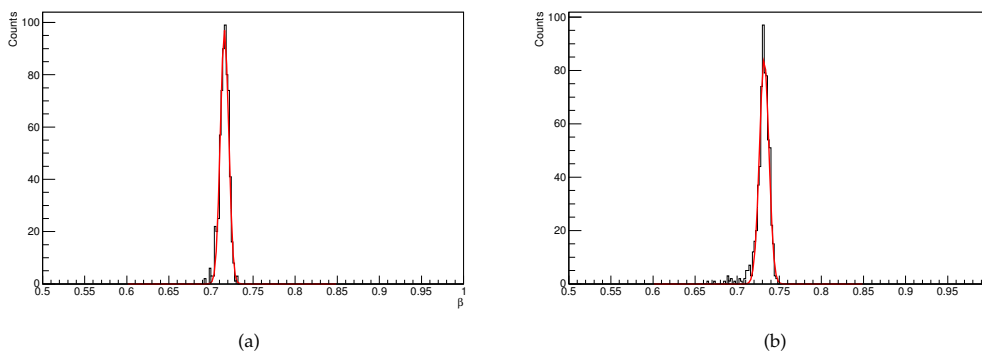


Figure 4.6: β of the outgoing ^{12}Be fragment after break up. Due to the fact that two different fragment separator settings are used for the final analysis, the incoming and outgoing fragment have two different velocities: (a) Data from setting 4, centered at ^{22}O ; (b) Data from setting 5, centered at ^{23}O . A fit using a Gaussian distribution has been applied over the two different datasets, the values obtained are $\beta_{F_{set4}}=0.716\pm 0.005$ and $\beta_{F_{set5}}=0.732\pm 0.005$

4.5. Breit-Wigner fit

The relative energy of the system ^{12}Be and neutron of the events that fulfill the previously explained conditions is displayed in figure 4.7. A total amount of 1257 candidates of ^{12}Be + neutron have been found within the 0-6 MeV range of the Relative energy spectrum.

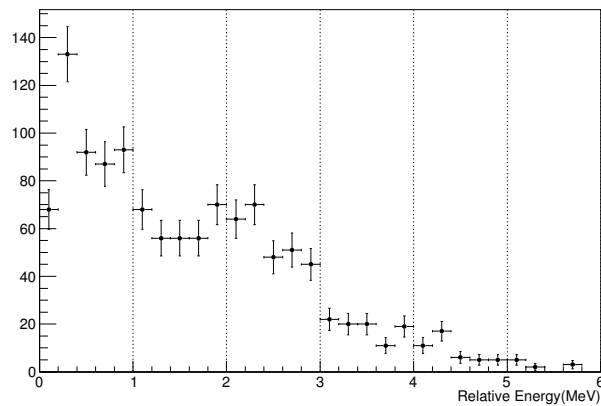


Figure 4.7: Relative energy spectrum of ^{12}Be +neutron. Obtained inserting the observables into equation 4.9. The physical interpretation of this figure will be detailed in chapter 5. Using both data settings, the total statistics after imposing all conditions the total amount of counts is 1257.

4.5 Breit-Wigner fit

The aim of this thesis work is disentangle the spectrum of figure 4.7 and study the structure of the nucleus ^{13}Be . It is an unbound nucleus, therefore even its ground state is unbound, however it displays certain internal structure in the form of resonances or quasi-stationary states. These are almost bound states, with energies not far from the limits determined from the potential. A peak observed in the relative energy spectrum of the system reveals the coincidence with one of these exotic states. These kind of states are described by the Breit-Wigner formula (equation 4.10), which is derived from the R-Matrix theory of nuclear reactions [81][82],

$$\frac{d\sigma}{dE} \sim \frac{\Gamma(E)}{(E_r - E)^2 + \frac{\Gamma(E)^2}{4}} \quad (4.10)$$

4. Analysis

The resonance width $\Gamma(E)$ depends on the reduced width of the resonance γ^2 and the penetrability factor $P_l(\rho, \eta)$, where l is the angular momentum of the resonance and η is the Coulomb field parameter.

$$\Gamma(E) = 2\gamma^2 P_l(\rho, \eta) \quad (4.11)$$

The parameter ρ is proportional to the reduced mass of the system μ , the channel radius R and the energy E .

$$\rho = kR = \frac{\sqrt{2\mu E}R}{\hbar} \quad (4.12)$$

The Penetrability factor for neutrons ($\eta=0$) is an expression only dependent on ρ , but different for each angular momentum.

$$\begin{aligned} P_0(\rho) &= \rho; \\ P_1(\rho) &= \frac{\rho^3}{1 + \rho^2}; \\ P_2(\rho) &= \frac{\rho^5}{9 + 3\rho^2 + \rho^4}; \end{aligned} \quad (4.13)$$

The first conclusion obtained from the Breit-Wigner expression is that there are only two parameters free to be fitted: the reduced width of the resonance γ , and the resonance energy E_r . The channel radius R must be specially pointed out, it can be described as the range of the potential, it has to be chosen to be larger than the boundaries of this potential in order to approximate the wave function to the asymptotic part. The final result for E_r is not very sensitive to the R value variation as will be shown in section 5.1.

The function to be fitted has also to be folded with the detector resolution as will be shown in the section 5.1.1.

4.6. Detection of ^{12}Be gamma rays

4.6 Detection of ^{12}Be gamma rays

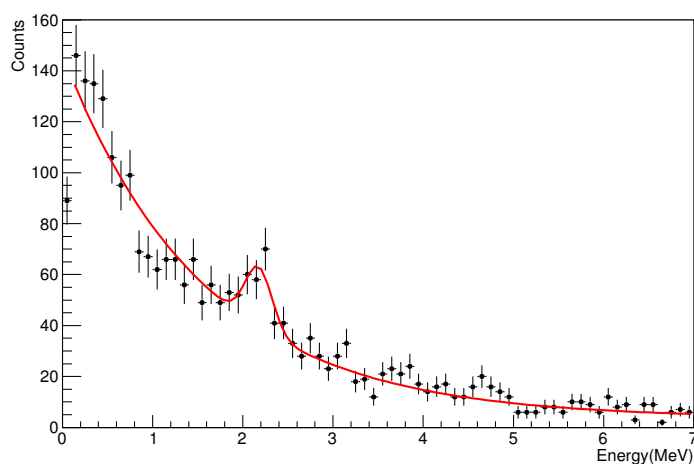


Figure 4.8: ^{13}Be Gamma spectrum detected by Crystal Ball in coincidence with the data of the obtained relative energy spectrum (see figure 4.7). The spectrum has been fitted to an exponential + Gaussian distribution in order to subtract the background. One broad gamma ray peak can be found in the energy range 2-2.4 MeV. The fit sets the gamma ray peak at $E=2.17\pm 0.04$ MeV.

Unfortunately, the invariant mass method has a drawback, it lacks of sensitivity to the energy transferred to the excitation of the decay products, just informs about the energy that has been transformed into kinetic energy. To access the ^{13}Be structure with full confidence, it is necessary to check the possible excited states in ^{12}Be that could be fed in the reaction. The way to do it, is to check for the prompt gamma rays emitted just after the decay with the Crystal Ball detector (section 2.3.2). Figure 4.8 displays the gamma spectrum, including a fit to the background using a negative exponential model and a Gaussian distribution for the broad peak in the energy range 2-2.4 MeV.

The daughter nucleus ^{12}Be has been studied extensively in recent years, thus we know already what we are looking for. Figure 4.9 shows that there are mainly three possible excited states in the ^{12}Be fed by the ^{13}Be break up at 2.1, 2.24 and 2.7 MeV. Although the second one at 2.24 MeV is an isomeric state [83] with too long

4. Analysis

life time ($\tau = 357(22)$ ns [84], $\tau = 331(12)$ ns [85]) for the possibilities of this detector setup. In case of feeding this isomeric state the decay will occur far from any detection chance. It is also worth mentioning that this kind of state will not decay to the ground state by gamma emission because both are 0^+ and such a transition is forbidden. Therefore it only has two ways to decay to the ground state, electron capture or pair production, in this case the nuclei should be fully stripped of electrons, thus the first path should not be available, just the second. The other way of decaying from the 2.24 MeV is emitting one low energy gamma to the 2.1 MeV state from where it could decay again to the ground state.

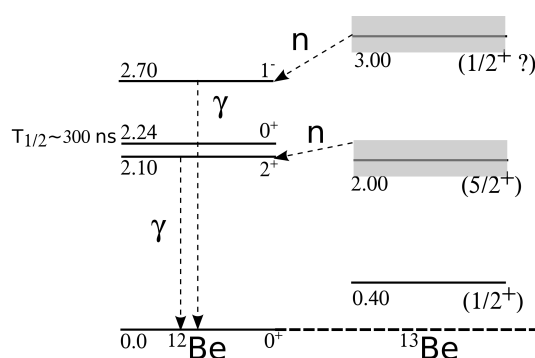


Figure 4.9: ^{12}Be energy level structure with dummy feeding from ^{13}Be . The three possible bound excited states of the ^{12}Be are shown. The state at 2.24 MeV is 0^+ , thus its decay via γ emission to the ground state is forbidden, further explanation in the text. The states included in ^{13}Be are just as a hypothesis to illustrate the decaying via neutron emission that feeds the ^{12}Be states. This level scheme includes the usually accepted states around 0.4 and 2 MeV (this latter only can decay via neutron emission to the 2.10 MeV state from the upper part of the resonance). The state at 3 MeV is a possibility suggested in several papers.

At the gamma spectrum of figure 4.8, the fit to the Gaussian-shaped distribution located the peak at $E=2.17\pm 0.04$ MeV with $\sigma=0.49\pm 0.05$, whereas the background has been subtracted as can be seen in figure 4.10. The result of the subtraction was fit again in the same region, positioning the gamma peak at 2.15 ± 0.02 MeV with $\sigma=0.15\pm 0.02$.

In the only previous ^{13}Be experiment where gamma ray detectors were available [33], not only gammas from the first excited state of ^{12}Be at 2.1 MeV but also from the state at 2.7 MeV were found. The available data of this experiment have not shown a peak that can be correlated to that second state.

4.6. Detection of ^{12}Be gamma rays

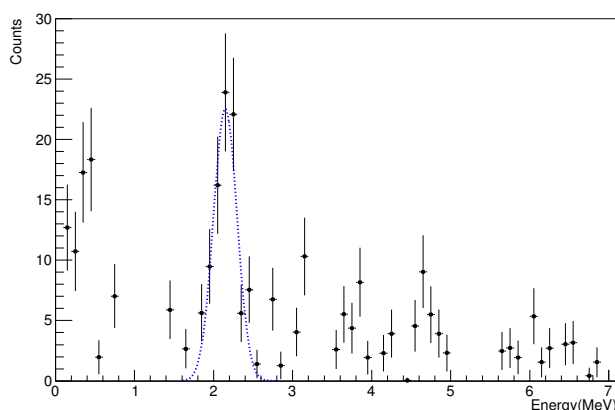


Figure 4.10: The same gamma spectrum of figure 4.8 after subtracting the background. A smoothening of the main bins of the peak has been made in order to be able to fit it to a Gaussian shaped curve. The integral of the peak give 83 counts.

The next step is to find a correlation between the gamma ray and any of the resonances found in the $^{12}\text{Be} + n$ relative energy spectrum (see figure 4.7).

The gamma ray peak has been gated-on (see figure 4.11) but the result is dominated by uncorrelated counts, in order to clean it, the spectrum has been gated off-peak on both sides and with the two resulting spectra a mean has been performed. Later the mean spectrum has been subtracted from figure 4.11, and the outcome is the clean gamma-gated spectrum in figure 4.12. Several other methods to subtract the uncorrelated ^{13}Be events from the relative energy spectrum of the coincidence with the gamma ray at 2.1 MeV have been tried, being the final result rather similar.

Even with the low statistics one can certainly draw a conclusion from figure 4.12. It seems obvious that there is no correlation with any medium or high energy resonance, as the relative energy spectrum seems rather flat above 1 MeV in all the subtraction methods used. However the two bins at 0.3 and 0.7 MeV are obviously favoured after removing the uncorrelated events, although the bin at 0.5 MeV is suppressed. Hence, it can be understood as two possible resonances located around those bins being partially fed by a ^{13}Be state that decays to the 2.1 MeV state in ^{12}Be . However the second bin of the relative energy spectrum at 0.5 MeV is the highest and in figure 4.12 is lower than the fourth, as the total amount of counts in

4. Analysis

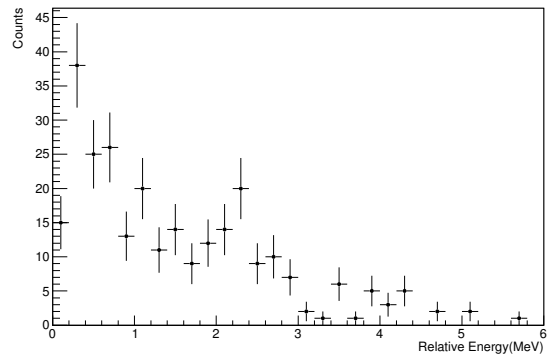


Figure 4.11: ^{13}Be Relative energy spectrum after gating on the gamma ray of 2.1 MeV.

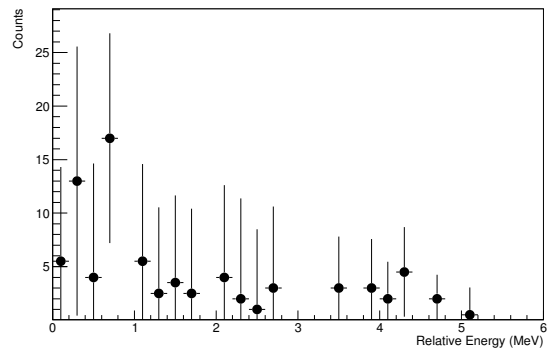


Figure 4.12: ^{13}Be Relative energy spectrum after subtraction of the uncorrelated events. The only bins still favoured are the second and the fourth at 0.3 and 0.7 MeV. The dots have been increased in size for a better visualization.

4.7. Looking at the protons of the (p,2p) reaction

the peak area was higher than the amount subtracted from the off-peak events, thus it is possible that this low-energy resonance is still uncorrelated from the gamma ray. The interpretation of these results in terms of nuclear structure of ^{13}Be will be given in the next chapter.

4.7 Looking at the protons of the (p,2p) reaction

The reaction we are dealing with is $^{14}\text{B}(p, 2p)^{13}\text{Be}$ using a polyethylene CH_2 target, in the analysis so far we have concentrated in looking for the $^{12}\text{Be} + n$ system. Despite that the previous requirements for the outgoing channel are very selective (incoming ^{14}B & $^{12}\text{Be} + n$), observing two outgoing high-energy protons with Quasifree conditions in Crystal Ball would clarify the complete picture of the reaction.

This (p, 2p) Quasifree scattering reaction is characterized by the angular correlation between the two outgoing protons. At non-relativistic velocities the outgoing protons have an average opening angle of 90° , however as shown in section 4.4 in this experiment the nucleus has a $\beta \simeq 0.73$ and thus relativistic considerations must be taken into account. The incident protons (in the ^{14}B) have bigger relativistic mass than the protons at rest in the target, hence the average opening angle between the knocked out protons is smaller, around $82^\circ - 84^\circ$. The equation 4.14 is obtained from the scalar product of the vectors of the two outgoing protons.

$$\Theta_{OpAngle} = \sin\theta_1 \cdot \sin\theta_2 \cdot \cos(\phi_2 - \phi_1) + \cos\theta_1 \cdot \cos\theta_2 \quad (4.14)$$

Additionally, the two particles are emitted back to back in the azimuthal angle $\Delta\phi = 180^\circ$. In order to represent the azimuthal angle difference, whenever the condition $\Delta\phi > 180^\circ$ or $\Delta\phi < 0^\circ$ are fulfilled, the difference is redefined as $\Delta\phi = 360^\circ - \Delta\phi$.

Figures 4.13 and 4.14 display the angular distributions as well as the $\Theta_{OpAngle}$ and $\Delta\phi$, using the same conditions as required in section 4.4 for the relative energy, although for figure 4.14 I have released the one neutron requirement to increase the statistics a factor of almost two (from 487 to 942 counts). The figures display the two clusters with higher energies detected within an event, having at least 30 MeV in order to discard energies coming from gamma rays. It has to be taken into account that the individual crystals of the Crystal Ball are rather big and having an angular uncertainty of $\pm 7.5^\circ$, as every event includes at least two crystals, the uncertainty could be up to 15° . The angle assigned to every Crystal Ball event is coming from the crystal hit in that event, therefore due to the size of the crystal, in order to have a good visualization without large gaps in the angular distributions a randomisation [49] of the nominal value of the crystals angle is added to every proton event.

4. Analysis

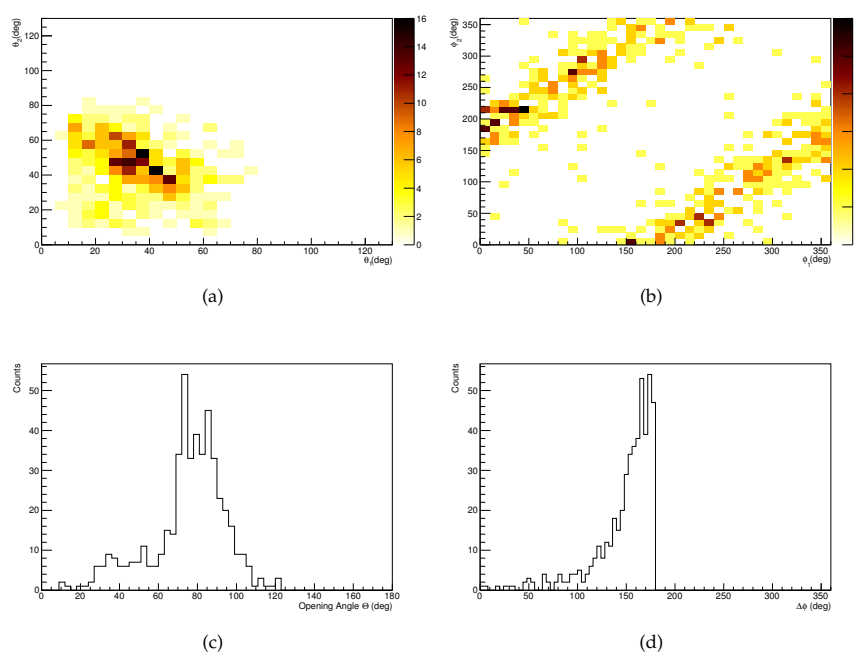


Figure 4.13: Angular distributions of two protons in coincidence with ^{12}Be events from ^{14}B , the full integral has 487 counts: (a) Polar Angle correlation, Quasifree scattering correlation is displayed ; (b) Azimuthal Angle correlation, the two strips of correlation between both angles can be seen; (c) Opening Angle, peaked around 80° ; (d)Azimuthal angle difference, peaked at 180° .

4.7. Looking at the protons of the (p,2p) reaction

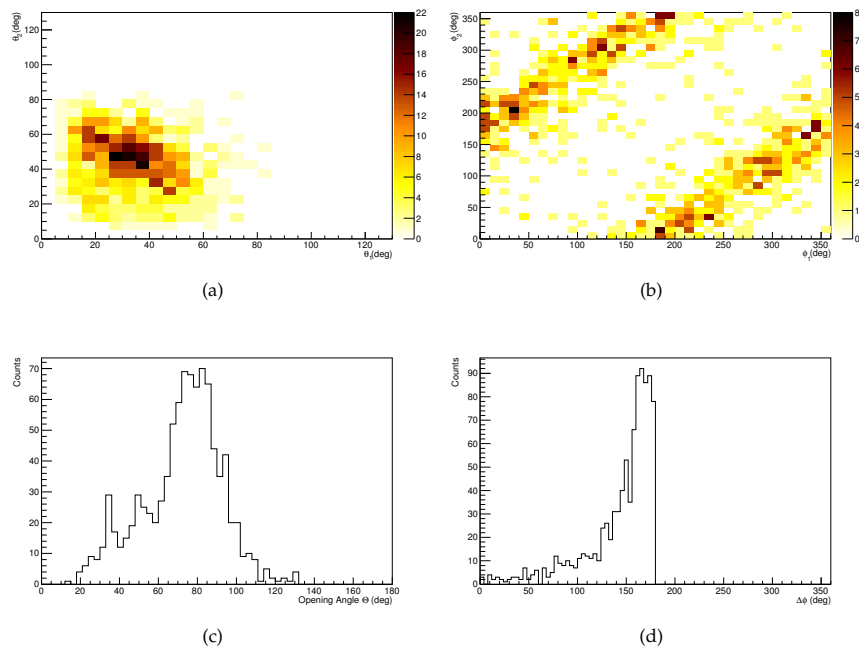


Figure 4.14: Angular distributions of two protons in coincidence with ^{12}Be events from ^{14}B , the full integral has 942 counts: (a) Polar Angle correlation, Quasifree scattering correlation can be seen better than in figure 4.13; (b) Azimuthal Angle correlation, the two strips of correlation between both ϕ angles can be seen better than in figure 4.13; (c) Opening Angle, peaked around 80° ; (d) Azimuthal angle difference, peaked at 180° .

4. Analysis

**“All Bette’s stories have happy endings. That’s because she knows where to stop.
She’s realized the real problem with stories...
if you keep them going long enough, they always end in death. ”**

Neil Gaiman. 24 Hours, The Sandman

5 Results & Discussion

The previous chapter covered the analysis method followed to clean and select the production channel of ^{13}Be and introduced the basis of the fitting procedure to a Breit-Wigner function including the singularities related to unbound nuclei.

This final chapter will show the different results obtained and discuss the possible interpretation in the context of the previous published results.

5.1 Preliminaries

In order to perform the fits a channel radius of $R = 5$ fm has been assumed. This value has to be large enough to be out of the boundaries of the nuclear potential. It has been taken following Kondo et al [33] who used a value of 4.9 fm, and taking into consideration that in [79] it is shown that a variation of 1-2 fm in this value should not represent a significant difference to the result of the fit, the detector resolution has a much bigger influence.

In order to confirm the previous assumption, after getting a good fit with a reasonable set of values, the position of the resonance has been fixed as well as the angular momentum, and a set of new fits has been performed considering different channel radii. The result of that set of fits can be seen in figure 5.1. It is possible to see certain differences on several spots harder to fit, but it can be concluded that the parameter R considered does not make a big difference in the result.

We have followed the χ^2 minimization approach to perform the fits, using the MINUIT tool [86]. Despite the low number of counts in the relative energy spectrum, which is a problem for the physical interpretation, it does not represent a problem to be fitted by the χ^2 method, which, on the other hand, does not work properly with empty or close to empty bins.

5. Results & Discussion

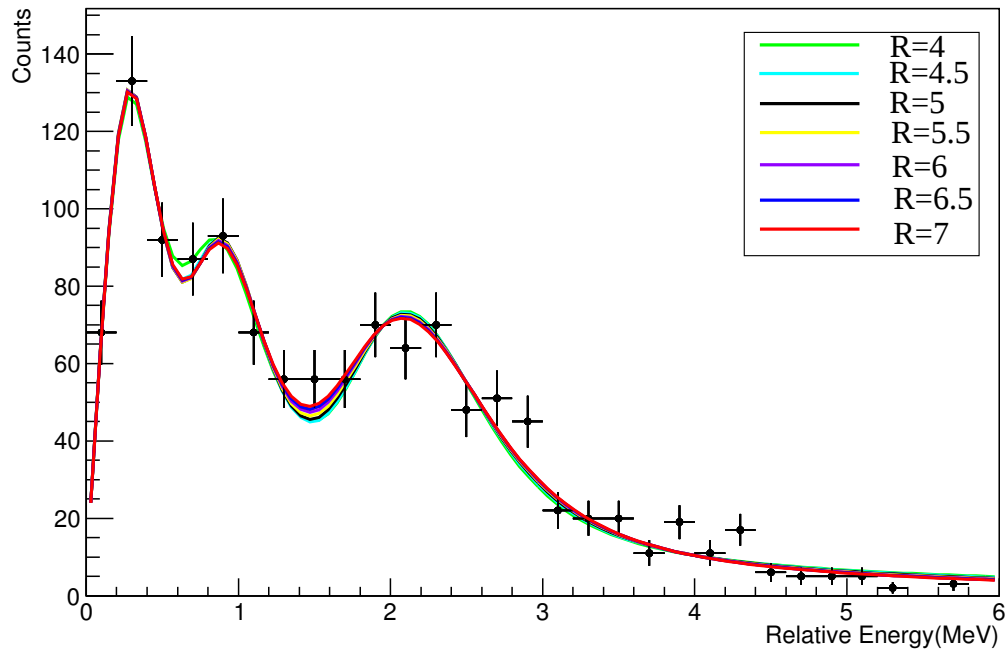


Figure 5.1: Channel Radius comparison. 1-2 fm Changes do not determine a big difference in the final result of the fit.

5.1.1 Folding

In order to compare the relative energy results with the fit to a Breit-Wigner function, it should be folded with the detector resolution, introducing the uncertainty related to the detector response.

The response function is described using a Gaussian shape with a certain standard deviation σ that is defined following the function in figure 5.2 for the relevant energy range. Therefore a Gaussian function with that σ dependence is included into the fit procedure.

5.1. Preliminaries

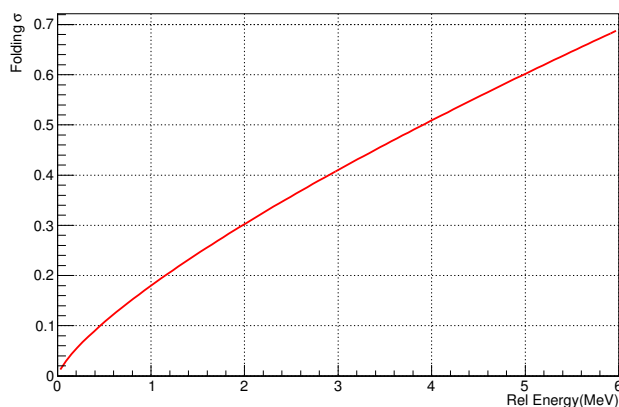


Figure 5.2: Relative energy range against the calculated standard deviation σ used for the folding function.

5.1.2 Non Resonant Background

Despite the reaction channel should be rather clean after the previous selections (see section 4), there might be events within the spectrum that are the result of a wrong identification either from the incoming or outgoing fragment or the neutron detected. In order to take into account such misidentification a Non-resonant Background has been modeled with equation 5.1. The model has a negative exponential function and an Error Function with three parameters: $A_{1,2,3}$.

$$E_{NR} = A_1 \cdot e^{-A_2 E} \cdot erf(A_3 E) \quad (5.1)$$

This addition to the fit, makes the resonances results more chaotic, i.e., more dependent to the initial parameter values as well as the constraints included for them and the three parameters of the background. This situation has made impossible to leave freely the background parameters, not only because they easily adopt non-physical negative values but because they greatly determine changes on the resonances. The shape of the background, which is determined by the parameters $A_{2,3}$ has been approximated as can be seen in figure 5.3. Equation 5.1 was used to fit a relative energy calculated including other tracked fragments (Beryllium masses ranging from $A = 10-14$) whereas the condition of finding one neutron in LAND was fixed.

5. Results & Discussion

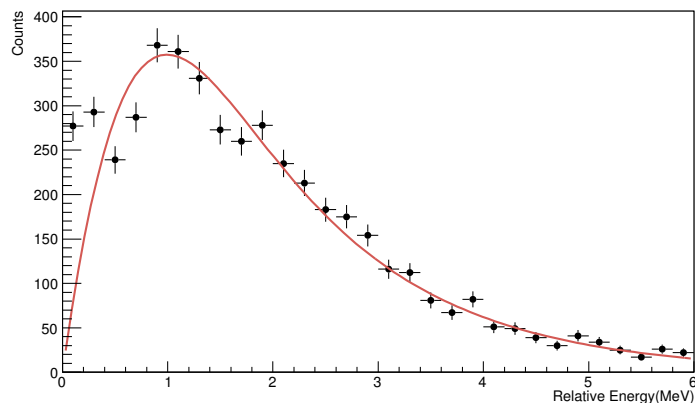


Figure 5.3: Non-Resonant background fitted to get an approximation to the parameters $A_{2,3}$ that defines the shape of the background. The data comes from considering for the relative energy calculation the Beryllium fragments with masses between $A = 10$ and 14 coming out from the ^{14}B reaction with the CH_2 target.

Such a model function has been included in several of the following fits, leaving the first parameter free (the amplitude A_1). The function was just added to the Breit-Wigner global function and fit accordingly. A similar method has been followed in [17].

5.2 Results

5.2.1 Initial parameters

The first approach has been to perform a set of individual fits to the three resonances that can be seen in the relative energy spectrum in order to find a set of reasonable starting values for each parameter to perform later a global fit. The method followed has been to fix the values of the angular momentum l and going through a reasonable range of values for the γ and E_r . Previous publications have found or assumed a low energy virtual state or a ground state with $l=0$, and found another resonance around 2 MeV with $l=2$, thus it has been the basic assumption, even though other values have also been tried.

The structure of the incoming ^{14}B nuclei is known and several publications reports [87][88] that the valence neutrons have $s_{1/2}$ and $d_{5/2}$ character, therefore

5.2. Results

this is the configuration for the momentum of ^{13}Be states that could have been fed in this experiment.

The single fit of each of the three resonances considered are shown in figure 5.4. We have gone through all the values for E_r and γ (reduced width, related with Γ , see section 4.5) in a reasonable range to look for good starting values for the global fit. It is worth to point out that for certain fits the value obtained of $\chi^2/N_{df} \ll 1$, thus the result is overfit and although it is the minimum value, in general it should not be considered as the best result to start working with. In any case, the values obtained fitting one single resonance are just an approximation that does not represent the real values of the resonances.

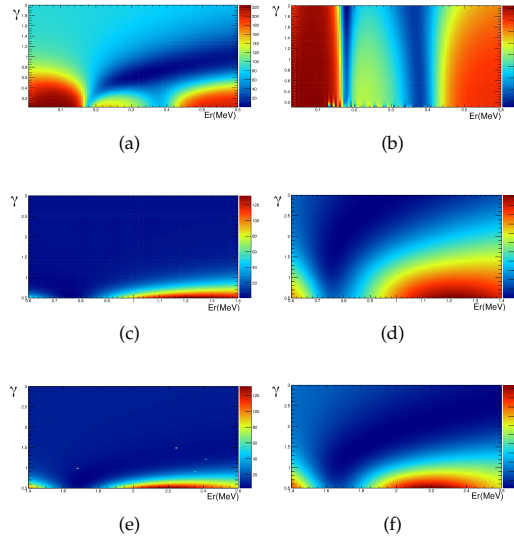


Figure 5.4: The color in the Z coordinate represents the calculated value of χ^2 , whereas γ is the reduced width (related with $\Gamma(E)$) and E_r the mean value of the resonance. (a) And (b) show the first resonance assumed between 0 and 0.6 MeV with a) $l=0$ and b) $l=2$; (c) and (d) show the second resonance assumed between 0.6 and 1.4 MeV with c) $l=0$ and d) $l=2$; (e) and (f) show the third resonance assumed between 1.4 and 2.6 MeV with e) $l=0$ and f) $l=2$

The values obtained for the resonance at low energies with $l=0$ of figure 5.4(a) display an important difference in the χ^2 value between 0.2 MeV and 0.4 MeV specially for small widths. A more careful look at these values using the relative

5. Results & Discussion

energy spectrum shows a strange behaviour close to 0.2 MeV , while the results close to 0.4 MeV are more reasonable. The large size of the bins (0.2 MeV), and the big difference in the number of counts between the first bin at 0.1 MeV and the second at 0.3 MeV is generating this strange behaviour with small widths.

5.2.2 Considering two resonances

Previous studies have determined only two resonances within the range 0-2.5 MeV for the ^{13}Be nucleus. Thus, although the fifth bin of the histogram shows an increment and a significant difference with the sixth bin, we have started considering only two open resonances.

A low energy state with $l=0$ and another one close to 2 MeV with $l=2$ are initially considered. A fit without a non-resonant background has been made, but the result (see figure 5.5) shows that the first Breit-Wigner function alone is not capable to make a good approximation for its range. The $\chi^2/N_{df}=2.24$ indicates the low-quality of this fit (see the result of the fit at table 5.1).

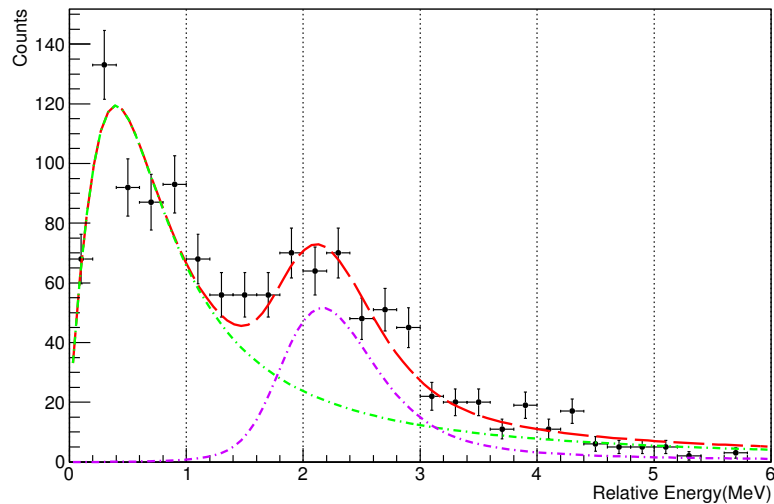


Figure 5.5: Visualization of the fit with two resonances $l=0$ (green), 2 (purple) and without a Non-resonant background. The global fit has a goodness of $\chi^2/N_{df}=2.24$ and it is represented by the red line. Table 5.1 shows the results.

5.2. Results

#	l	$E_r(\text{MeV})$	$\Gamma(\text{MeV})$
1	0	0.54 ± 0.04	1.185 ± 0.002
2	2	2.18 ± 0.06	0.381 ± 0.009
χ^2		49.26	
χ^2/N_{df}		2.24	

Table 5.1: Table of results considering two peaks without Non Resonant Background and $l=0,2$. Figure 5.5 shows the visualization of the fit.

In order to improve the fit, a non-resonant background has been included (see section 5.1.2), the initial values for the mean and width parameters have been the results from the previous fit (table 5.1). The output of the fit had the tendency to produce non-physical values for the resonance widths (lower than 0.1 MeV). To get a result with physical meaning it has been necessary to fix a parameter, the resonance position of the second curve $E_r=2.18 \pm 0.06$ MeV. It was chosen because it is the least affected by the inclusion of the background. The results of the fit can be seen in table 5.2, the value $\chi^2/N_{df}=1.32$ represents a significant improvement with respect to the previous fit. Even though the background gives a better description of the area 0.7-1.7 MeV, it almost skips the count rise in the 0.9 MeV bin, as can be seen in figure 5.6, however the description of the low-energy part of the spectrum has improved.

#	l	$E_r(\text{MeV})$	$\Gamma(\text{MeV})$
1	0	0.287 ± 0.038	0.411 ± 0.008
2	2	2.18(fixed)	0.176 ± 0.034
χ^2		29.04	
χ^2/N_{df}		1.32	

Table 5.2: Table of results considering two resonances with Non Resonant Background and $l=0,2$. Figure 5.6 shows the visualization of the fit.

5. Results & Discussion

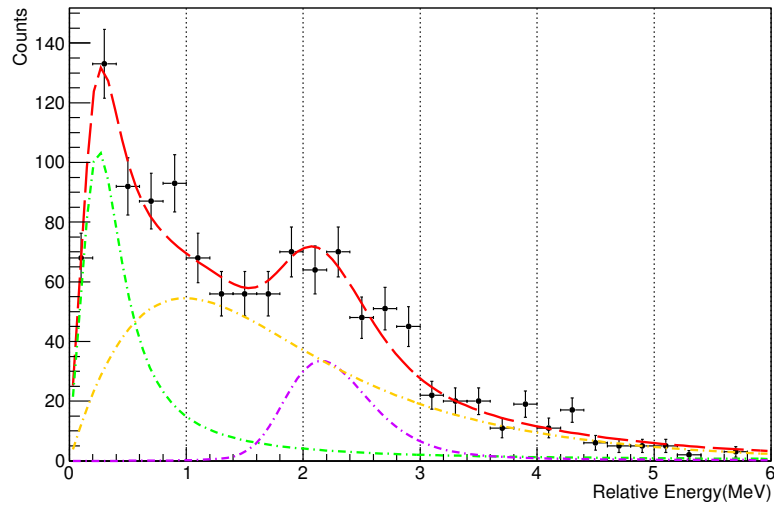


Figure 5.6: Visualization of the fit considering two resonances $l=0$ (green), 2 (purple) with Non resonant background (yellow). The global fit has a goodness of $\chi^2/N_{df}=1.32$ and it is represented by the red line. Table 5.2 shows the results.

5.2.3 Considering three resonances

Previous publications have considered the inclusion of an s-or-d state in the region between the low energy s-state and the d-state at 2 MeV [46]. In order to reproduce the count increment of the fourth and fifth bin (0.7-0.9 MeV), another Breit-Wigner function has been introduced into the fit, within the energy range 0.6 - 1.2 MeV. The two possible orbital momenta $l=0,2$ have been considered.

In this case the results obtained for the χ^2/N_{df} (see tables 5.3 and 5.4) are closer to 1 and the fit seems to be more reliable. Figures 5.7 and 5.8 are similar, both options have the same third resonance (within the errors) whereas the widths of the other two resonances are rather different in each case, even the position of the first resonance changes considerably between the two options.

5.2. Results

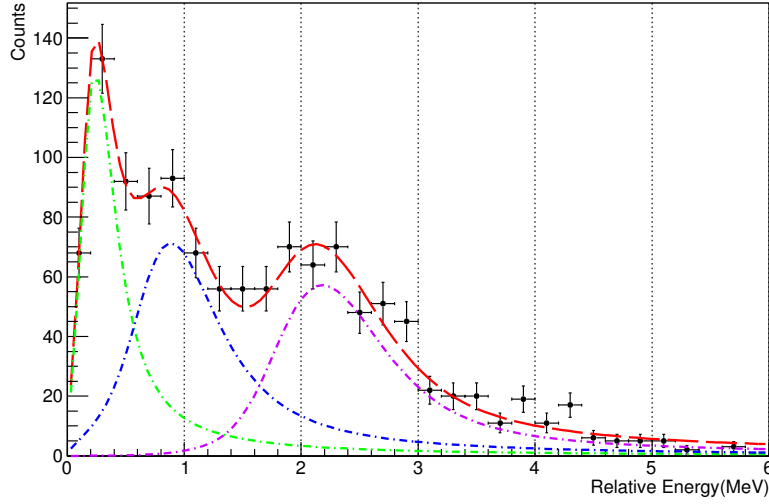


Figure 5.7: Visualization of the fit considering three Breit Wigner functions with $l=0$ for the green line, $l=0$ for the blue line, $l=2$ for the purple line. The global fit has a goodness of $\chi^2/N_{df}=1.27$ and it is represented by the red line. The position of the resonances and the widths obtained are in table 5.3.

#	l	$E_r(\text{MeV})$	$\Gamma(\text{MeV})$
1	0	0.265 ± 0.048	0.319 ± 0.013
2	0	0.929 ± 0.080	0.741 ± 0.029
3	2	2.209 ± 0.064	0.635 ± 0.064
		χ^2	24.12
		χ^2/N_{df}	1.27

Table 5.3: Table of results considering three resonances without Non-Resonant Background and $l=0, 0, 2$. The visualization of it is displayed in figure 5.7.

The non-resonant background has been included in this case as well, despite it seems less necessary than when considering just two resonances. Here it leads to either unphysical widths of the resonances, specially for the second, or that the non-resonant background vanishes, being so small that it is unnoticeable.

5. Results & Discussion

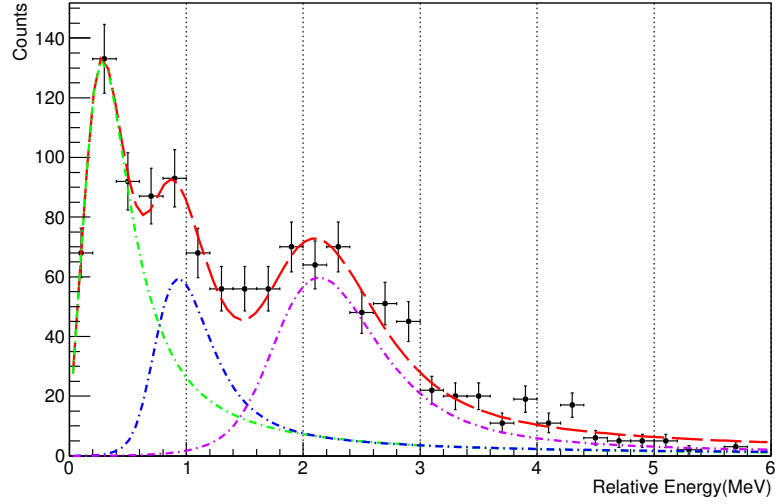


Figure 5.8: Visualization of the fit considering three resonances using three Breit Wigner functions with $l=0$ for the green line, $l=2$ for the blue line, $l=2$ for the purple line. The global fit has a goodness of $\chi^2/N_{df}=1.57$ and it is represented by the red line. The position of the resonances and the widths obtained are in table 5.4.

#	l	$E_r(\text{MeV})$	$\Gamma(\text{MeV})$
1	0	0.333 ± 0.036	0.5196 ± 0.0054
2	2	0.951 ± 0.055	0.29 ± 0.026
3	2	2.157 ± 0.058	0.5845 ± 0.0076
		χ^2	29.9
		χ^2/N_{df}	1.57

Table 5.4: Table of results considering three resonances without Non-Resonant Background and $l=0, 2, 2$. The visualization of the fit is displayed in figure 5.8.

In order to find a physical solution for these two cases the width of the second resonance has been fixed using the values calculated before without the background. The other previously calculated parameters were taken as initial input values. Looking at the values obtained (see tables 5.5 and 5.6), the reliability of both fits

5.2. Results

is high, having a value for $\chi^2/N_{df} \simeq 1.15$ that is almost the same. Again the second resonance is in the same position for both solutions, although there is a noticeable difference in the width. Figures 5.9 and 5.10 show the graphical output of the fit.

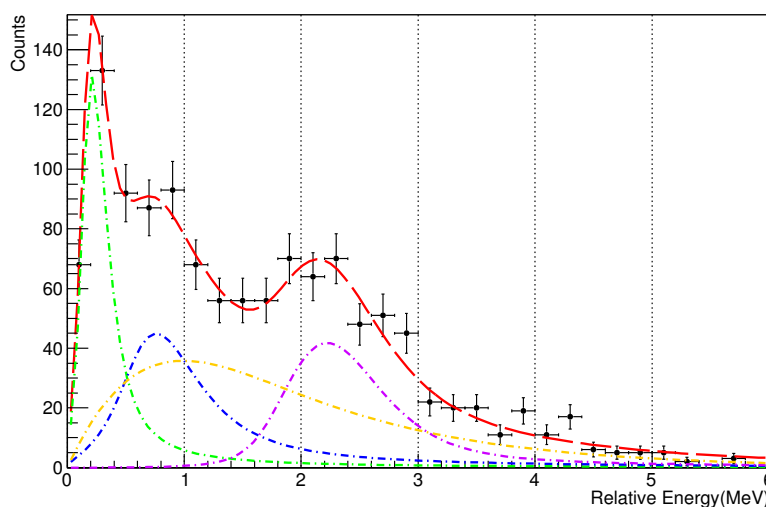


Figure 5.9: Visualization of the fit using three Breit Wigner functions with $l=0$ for the green line, $l=0$ for the blue line, $l=2$ for the purple line. The global fit has a goodness of $\chi^2/N_{df}=1.15$ and it is represented by the red line. The resonance Energies and the widths obtained are in table 5.5.

#	l	E_r (MeV)	Γ (MeV)
1	0	0.226 ± 0.050	0.195 ± 0.034
2	0	0.80 ± 0.16	0.743(fixed)
3	2	2.240 ± 0.072	0.383 ± 0.036
		χ^2	21.89
		χ^2/N_{df}	1.15

Table 5.5: Table of results considering three resonances with Non-Resonant Background and $l=0,0,2$. The visualization of the fit is displayed in figure 5.9.

5. Results & Discussion

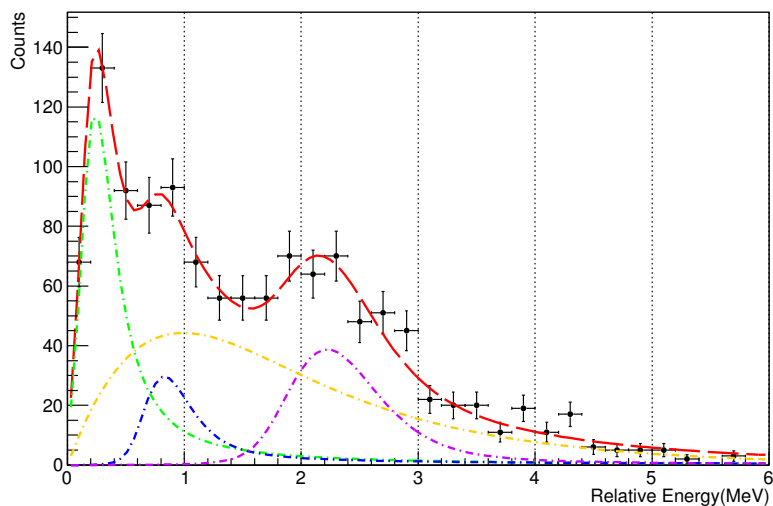


Figure 5.10: Visualization of the fit considering three Breit Wigner functions with $l=0$ for the green line, $l=2$ for the blue line, $l=2$ for the purple line. The global fit has a goodness of $\chi^2/N_{df}=1.18$ and it is represented by the red line. The resonance Energies and widths obtained are in table 5.6.

#	l	$E_r(\text{MeV})$	$\Gamma(\text{MeV})$
1	0	0.262 ± 0.033	0.312 ± 0.007
2	2	0.838 ± 0.085	0.29(fixed)
3	2	2.241 ± 0.077	0.268 ± 0.036
		χ^2	22.43
		χ^2/N_{df}	1.18

Table 5.6: Table of results considering three resonances with Non-Resonant Background and $l=0,2,2$. The visualization of the fit is displayed in figure 5.10.

5.2. Results

5.2.4 Considering Quasifree Scattering

The Quasifree scattering (QFS) reactions are more restrictive, and therefore cleaner than a normal knockout reaction and, moreover, they are capable to excite deeper nucleons of the isotope structure. The Quasifree scattering correlations have been seen in the previous section 4.7, although to make it a requirement of the measurement, certain conditions must be imposed to the knocked out protons from the reaction $^{14}\text{B} (p, 2p) ^{13}\text{Be}$ such as $60^\circ < \Theta_{Op.Angle} < 110^\circ$ and $\Delta\phi > 110^\circ$ (see section 4.7 and in particular figures 4.13 and 4.14). These conditions leave very few counts into the relative energy spectrum (385 counts), but despite the lack of statistics, detailed information can be gained from the spectrum. There are two main features to be pointed out: The resonance around 0.8-0.9 MeV is more evident, which will help to determine a more realistic width for an assigned resonance, and it is also worth to point out the count reduction within the tenth bin at 1.9 MeV, which suggests the possible split of the broad resonance around 2 MeV in two different resonances peaked around 1.6 MeV and 2.2 MeV. However, none of the previous publications have reported two resonances in the area. Thus, in the following this count suppression will be regarded as a statistical phenomenon, and another resonance will not be considered in the fit.

The criterion of considering $l=0,2$ character of the first and last resonance will be followed, as well as the method of testing both angular momentum possibilities for the second resonance.

In order to exclude the influence of the tenth bin at 1.9 MeV the error bars for the tenth bin have been increased. This increment is enough to reach the error limits of the neighbouring bins. Without this change, the resulting fit tends to be unphysical. Such a change is consistent with the assumption of just one resonance in the 2 MeV region and is also supported by comparing with the relative energy spectrum obtained requiring two protons in Crystal Ball.

Studying figures 5.11 and 5.12 it seems evident that the result of the fit is dominated by the lowered tenth bin, specially in the case of $l_2=0$. Considering the results with and without Quasifree scattering conditions, the position of the resonances are the same (within the error of the relative energy) whereas the resonance widths did not change much in the case of the $l_2=2$ (see tables 5.8 and 5.4) but for $l_2=0$ the widths are broader. However the uncertainties are bigger.

5. Results & Discussion

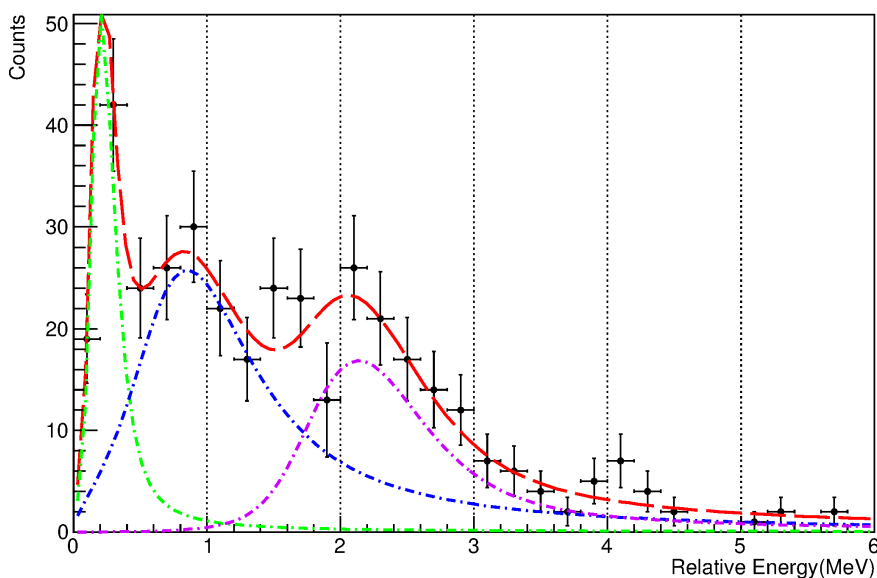


Figure 5.11: Visualization of the fit to a relative energy spectrum in coincidence with QFS scattering, the fit uses three Breit Wigner functions with $l=0$ for the green line, $l=0$ for the blue line, $l=2$ for the purple line. The global fit has a goodness of $\chi^2/N_{df}=0.75$ and it is represented by the red line. The resonance energies and widths obtained are in table 5.7.

#	l	$E_r(\text{MeV})$	$\Gamma(\text{MeV})$
1	0	0.214 ± 0.083	0.12 ± 0.16
2	0	0.92 ± 0.17	1.03 ± 0.24
3	2	2.16 ± 0.21	0.54 ± 0.20
		χ^2	12.85
		χ^2/N_{df}	0.75

Table 5.7: Table of fit results in coincidence with QFS, using in the fit three resonances and $l=0,0,2$. Figure 5.11 displays the visualization of the fit.

It is also worth to consider the goodness of the fits obtained, $\chi^2/N_{df}=0.75$ for $l_2=0$ and 0.82 for $l_2=2$. Both results are good, close to 1.

5.2. Results

In this case, including a non-resonant background has also been tried but the result has been even more chaotic than for the three resonances situation and after fixing certain values the obtained result has not been satisfactory. As was suggested in section 5.1.2, the non-resonant background should not be big due to the clean conditions previously settled, hence in this case after requiring a very restrictive condition such as detecting two protons in coincidence, this background should be even lower and therefore negligible.

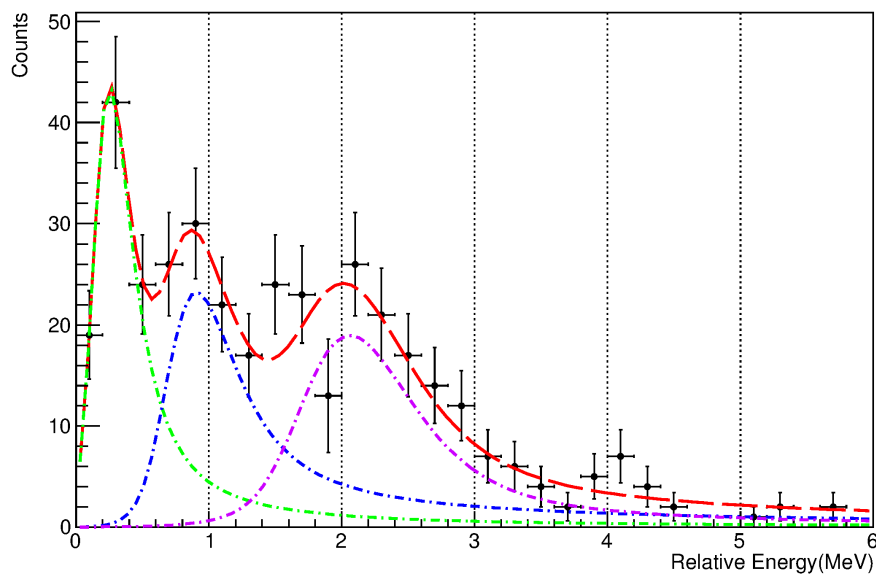


Figure 5.12: Visualization of the fit in coincidence with QFS scattering, it uses three Breit Wigner functions with $l=0$ for the green line, $l=2$ for the blue line, $l= 2$ for the purple line. The global fit has a goodness of $\chi^2/N_{df}=0.82$ and it is represented by the red line. The resonance energies and widths obtained are in table 5.8.

5. Results & Discussion

#	l	$E_r(\text{MeV})$	$\Gamma(\text{MeV})$
1	0	0.279 ± 0.054	0.322 ± 0.015
2	2	0.95 ± 0.16	0.53 ± 0.23
3	2	2.08 ± 0.17	0.547 ± 0.087
χ^2		13.9	
χ^2/N_{df}		0.82	

Table 5.8: Table of results in coincidence with QFS, using three resonances and $l=0,2,2$. Figure 5.12 displays the visualization of the result.

5.3 Discussion

In order to start the discussion it is necessary to remember certain assumptions that have been made for the analysis.

Previous studies of the incoming nucleus or projectile ^{14}B [87][88] have reported the domination of the components $2s_{1/2}$ and $2d_{5/2}$ on the valence neutron configuration that should be intact after the reaction $^{14}\text{B}(p,2p)^{13}\text{Be}$ of this experiment. That is why only s or d states were considered as options for the analysis. It is important to remember as well that ^{13}Be , since it is a neutron-rich unbound nucleus or resonance, in principle should not be able to hold s-states due to their lack of a centrifugal barrier, although as pointed by [41] ^{12}Be is a deformed nucleus without magicity despite having $N=8$, thus the core is not inert and should provide the possibility of emerging s-states. Actually the latest experimental results published by Aksyutina et al [43] and Randisi et al [46] already considered the first low-energy state as a $1/2^+$, in contrast to several previous works like Kondo et al [33] and Simon et al [42] that were including an s-virtual state to describe the first resonance (see figure 5.13).

The case of the $5/2^+$ state around 2 MeV is different, there seems to be a common agreement between the previous works on the existence of this state. However there is not an agreement on the exact position, which ranges between 1.8 and 2.4 MeV, whereas certain theoretical works set it even further, like Fortune [89][90] that places it 2.3 MeV above the first s-state, hence above 2.5 MeV.

The middle-ground resonance between the 0.2-0.5 MeV s-state and the ~ 2 MeV d-state has been less investigated. Although older studies using the missing-mass method or Lecouey et al [41] have reported about a state around ~ 0.8 MeV, this was usually considered as the ground state (which in our structure is around 0.3 MeV). That is why Aksyutina et al [43] conclude that the existence of a state below 1 MeV with $l \neq 0$ character, should not be rejected. At the same time Randisi et al [46] did settle a $5/2^+$ state at 0.85 MeV based on his experimental results and in a theoretical calculation.

5.3. Discussion

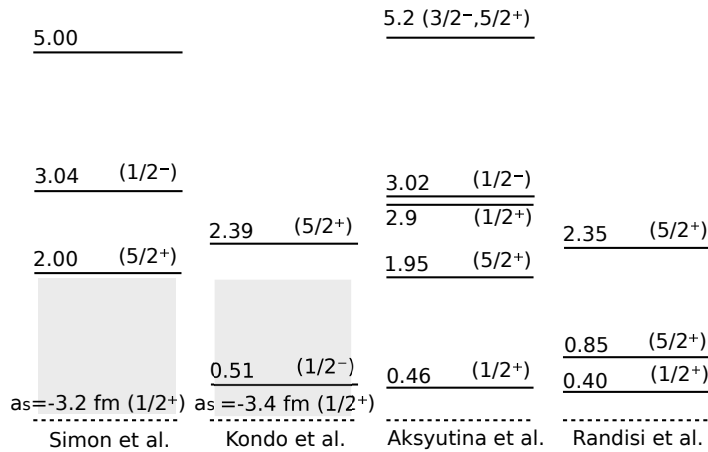


Figure 5.13: Comparison of the last published experimental results on the structure of ^{13}Be [46][43][33][42]. The dashed line represents the ground state of ^{12}Be in the four level schemes. a_s is the scattering length of the virtual s-states, the gray area represents the energy range of these states.

To reach a good interpretation of the present results it also worth to take into account that, except from Lecouey et al [41] and Randisi et al [46] at GANIL, the previous experiments used a different projectile from the ^{14}B used in the S393 experiment. Fortune [90] suggested the existence of two s-states for ^{13}Be , the second around 3 MeV, this idea was followed by Aksyutina to describe their spectrum by fitting it to a model considering interference between these two states, giving good results. The broader low-energy region of the ^{14}B experiments was considered an outcome of a pure s-state.

The relative energy spectrum obtained in our analysis does not show much feature above 2.5 MeV. Although in the previous publications there is an agreement on a state around 5 MeV, whose momentum character is not clear as well as a state close to 3 MeV with 1/2⁻ momentum and therefore not fed by the ^{14}B beam.

The scenarios presented in section 5.2 agree with the previous works in the position of the last resonance ~ 2.15 MeV. However the position of the first resonance in our analysis ranges from 0.214 to 0.54 MeV. The low quality of the first fit (table 5.5) is basically due to the bad representation of the low and middle part of the relative energy spectrum, and thus makes it easy to discard the value at 0.54 MeV, and accept the lower energies.

5. Results & Discussion

A quick look at the spectrum may give the impression that the assumption of a resonance at ~ 0.8 MeV is not realistic, the count increase between the 0.7 MeV and 0.9 MeV bin is clearly within the error bars, although the lowering of the 1.1 MeV bin is noticeable. The fit of figure 5.6, considering a broad non-resonant background describing the middle energy-range is good, although the small width for the d-state would be smaller than the previous measurements, and such a value would not fit to a resonance that is clearly broad in all other measurements. But still there are two main reasons to argue in favour of a middle-range peak:

- Two protons coincidence

The coincidences with two protons in Crystal Ball (and the Quasifree conditions) shows a clear peak in the area, and as stated before, this restrictive condition cleans more the miss-identified events of a non-resonant background.

- Gamma coincidences

Figure 4.12 shows that the bin at 0.7 MeV is favoured in coincidence with the 2.1 MeV gamma ray from the ^{12}Be . This implies the presence of a real peak in that area of the relative energy spectrum. However, in the ^{13}Be structure it would be related to a resonance at ~ 2.1 MeV + 0.95 MeV $\simeq 3.05$ MeV (see figure 5.14). This will be discussed further later in this subsection.

Once the inclusion of a third resonance has been clearly supported, it is worth to aim the discussion at the addition of the non-resonant background. Introducing a non-resonant background clearly complicates the three-resonance fit procedure. As it has been explained in section 5.2, it has not been possible to produce a clean fit without fixing certain parameters of the Breit Wigner function. Constraining the values for the parameter A_1 to have a small or moderate background, led to more reasonable values of the resonance widths. But there has not been a way to set a definitive value for that parameter, and the method followed to find approximate values of the $A_{2,3}$ parameters is too rough.

Considering three resonances, the necessity of a non-resonant background might not be very relevant due to the tendency of the fitting function to minimize the background to very low values, as well as the purity of the ^{13}Be channel with three coincidences needed: Incoming ^{14}B , outgoing ^{12}Be and one neutron selection. The very mentioned Aksyutina paper [43] neither included such a background reporting on a measurement made with the same setup (although lacking a gamma measurement) for the R3B Collaboration in a previous experiment. It is worth to remember as well, the difficulties to add the non resonant background to the fit of the spectrum in coincidence with the protons in Crystal Ball.

One aspect that the fit performed does not clarify is if the l of the second resonance is 0 or 2. Both fits either considering Quasifree scattering coincidence or not

5.3. Discussion

have a good χ^2/N_{df} , although the $l_2=0$ case with $\chi^2/N_{df}=1.27$ has a noticeable difference with the $\chi^2/N_{df} = 1.57$ value for the $l_2=2$ case. In contrast, the energy value for the first resonance is always lower in the $l_2=0$ case, which makes the result far from the last published results which set the energy value ~ 0.4 MeV, at the same time looking at figures 5.9 and 5.11 the low energy resonance seems to be displaced far to the left.

The two latest publications considered the possibility of such a state but both the momentum profile analysis performed by Aksyutina[43][45] and the theoretical calculations performed by Randisi [46] do not permit a $l_2=0$ state. It is also worth considering this state as a mixture of two (further discussion later on this subject).

Although it has been mentioned before, it is important to remark what has been found in the gamma-ray analysis. The obtained result is quite different from the only other work published that has measured gamma rays in coincidence with the ^{12}Be fragment and one neutron, Kondo et al [33]. In our data we have only found one of the two possible gamma rays emitted from the excited states of ^{12}Be : 2.1 MeV whereas Kondo et al claimed to see the 2.7 MeV gamma ray as well. This might in our case be due to the lack of statistics. But this is not the only relevant difference between both measurements. The authors of [33] inform that the 2.1 MeV gamma ray was correlated with events at very low relative energies of ~ 0.2 MeV or less, whereas in this work the same gamma ray has been correlated only with a resonance close to 0.7 MeV (see figure 4.12). The last remark that must be done about the gamma-ray measurement is that the ^{12}Be 2.1 MeV state is a 2^+ , therefore the feeding of this state must origin from an s or d state.

The presence of the coincidence between the 2.1 MeV gamma ray and a peak in the relative energy at 0.7 MeV makes evident that there is a resonance of ^{13}Be that decays to the 2.1 MeV ^{12}Be state. Therefore, despite there is a visible difference in the feeding of the bins at 0.7 MeV and 0.9 MeV in the relative energy coincidence spectrum (figure 4.12), their uncertainties in that area are between 200-250 keV (see Appendix A) and the amount of statistics is quite low. Thus we consider the peak of the relative energy spectrum located at ~ 0.95 MeV as coming from a resonance state at $2.1 \text{ MeV} + 0.95 \text{ MeV} \simeq 3.05 \text{ MeV}$. In order to feed the 2^+ state at 2.1 MeV of ^{12}Be , the neutron of ^{13}Be should be emitted from a state with momentum character $1/2^+$ or $5/2^+$.

A resonance at ~ 3.05 MeV is 0.35 MeV above the 2.7 MeV state 1^- of ^{12}Be and 0.8 MeV above the 2.24 MeV 0^+ isomeric state, thus they are energetically allowed for feeding. However in our relative energy spectrum, we have not found a peak at 0.35 MeV in coincidence with a 2.7 MeV gamma ray and we would not be capable to distinguish a different peak at 0.8 MeV from the one at 0.95 MeV. Assuming $J^p=5/2$ for this resonance at ~ 3.05 MeV would make those states of ^{12}Be almost forbidden. Although previous measurements have reported about a $1/2$ state close to 2.9 MeV [43] [42][38]. Therefore we cannot conclude a definitive momentum between $1/2$ and $5/2$.

5. Results & Discussion

Regardless of the previous argumentation, there exists the possibility that the resonance peak at 0.95 MeV is hiding two real-resonances of ^{13}Be , one at the position determined in the Breit-Wigner fits (0.95 MeV) whose momentum character is not obvious, although it would be consider as $5/2$, as was previously discussed in this section, whereas the other resonance would be located at $0.7\text{ MeV} + 2.1\text{ MeV} \simeq 2.8\text{ MeV}$ and it would have the same open momentum interpretation of the similar proposed state at 3.05 MeV ($1/2$ or $5/2$).

Figure 5.14 represents the structure suggested by this work, supported by our data analysis, the fit results and the discussion. The fit closer to this conclusion is the one displayed in figure 5.12 whose results are in table 5.8. Although the third resonance ($\sim 2.15\text{ MeV}$) has a worse position determination with the Quasifree scattering statistics, therefore its positions has been settled following the fit of table 5.4 and figure 5.8.

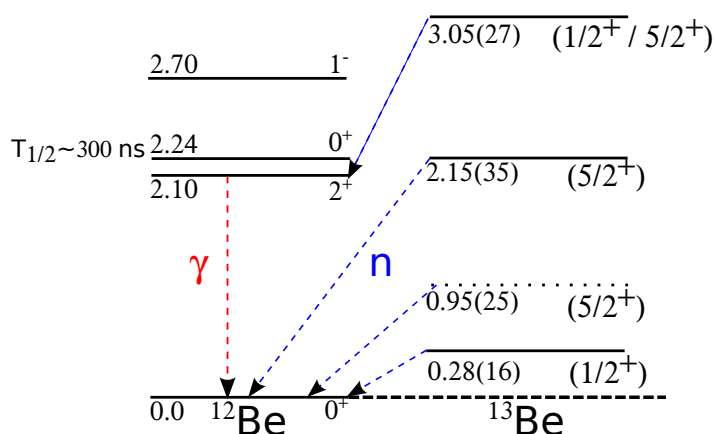


Figure 5.14: ^{13}Be structure proposed by this work. The neutron emissions are indicated in blue, whereas the only gamma ray detected is indicated in red. The dotted line indicates the possible state at 0.95 MeV. The dashed black line indicates the ground state of the ^{12}Be . As explained in the text, the ^{13}Be resonance at 3.05 MeV might be decaying to the 0^+ state at 2.24 MeV of ^{12}Be , however is impossible to confirm with the detector setup of this experiment. The error of the energy resonance positions are calculated by quadratical addition of the statistical error from the fit and the systematic error as explained in the Appendix A.

5.4. Conclusions

5.4 Conclusions

- The work reports on several possible resonant states of the unbound nucleus ^{13}Be and confirms some of the previously measured: One at 0.28 MeV with orbital angular momentum $l=0$ and another resonance with $l=2$ around 2.15 MeV. One feature at 0.95 MeV has also been found, this state must be interpreted in coincidence with the gamma-ray measurement. See figure 5.14 for the proposed ^{13}Be structure. Figure 5.12 and table 5.8 hold the best fit to the proposed values, except for the resonance at 2.15 MeV whose value is taken from table 5.4 and figure 5.8.
- This is the first time that an experiment reports on the measurement of the unbound ^{13}Be nuclear structure using $(p,2p)$ reactions under Quasifree scattering conditions.
- This is the second time that an experiment studying ^{13}Be has included a gamma-ray measurement. The results obtained are different from the previous work [33]. In our work the 2.1 MeV gamma-ray from ^{12}Be has been found in coincidence with a peak at ~ 0.95 MeV of the relative energy of the system $^{12}\text{Be} + \text{neutron}$. This peak is therefore interpreted as a ^{13}Be resonance at 3.05 MeV with a momentum character of $1/2^+$ or $5/2^+$.
- The lack of statistics as well as the broad relative energy resolution, especially above 3 MeV, has made impossible to extract more definitive conclusions. Despite this problems, this work has been capable of confirming previous results and proposing new resonances using the reaction $^{14}\text{B} (p,2p)^{13}\text{Be}$.
- The non-resonant background has not been found necessary in this case.

5.5 Future prospects

- The resonance fit around 0.95 MeV in coincidence with the 2.1 MeV gamma ray might be understood as a combination of a resonance around 0.95 MeV and another one at $2.1 \text{ MeV} + 0.7 \text{ MeV} \sim 2.8 \text{ MeV}$. The state at 0.95 MeV (dashed line in figure 5.14) would be $5/2^+$ as has been settled in previous publications [43][46] whereas the state at 2.8 MeV could be $1/2$ or $5/2$. This possibility should be checked in a future experiment.
- An improvement in every part of the setup used is currently under development for the FAIR facility. The gamma measurement will be improved by the new detector CALIFA. The protons coming out from the reaction will be much easily detected with the Silicon Tracker as well as CALIFA, improving the efficiency and energy resolution. NeuLAND will take care of the neutrons and

5. Results & Discussion

will help to improve the angular resolution which is the main constrain for the relative energy determination. These new detectors in combination with far more intense radioactive beams will help to improve the results obtained.

- Besides the resolution, efficiency and beam intensity improvements already planned, there is no information about the possible feeding to the other 0^+ isomeric state of the ^{12}Be at 2.24 MeV. An experiment capable of measuring a long-lived state after producing ^{13}Be would contribute further to the current knowledge about this exotic nucleus.

A Error calculations

In order to evaluate the uncertainties of the relative energy of the system $^{12}\text{Be} + \text{neutron}$, the error has been propagated in equation A.1 assuming certain uncertainties for the main parameters $\theta_{^{12}\text{Be}-n}$, β_n and $\beta_{^{12}\text{Be}}$.

$$E_{rel} = \left(\sqrt{m_{^{12}\text{Be}}^2 + m_n^2 + m_{^{12}\text{Be}}m_n\gamma_{^{12}\text{Be}}\gamma_n(1 - \beta_{^{12}\text{Be}}\beta_n\cos\theta_{^{12}\text{Be}+n})} - m_{^{12}\text{Be}} - m_n \right) c^2. \quad (\text{A.1})$$

The assumed systematic uncertainties for each parameter were:

- $\theta_{^{12}\text{Be}+n}$

From the silicon positions and angle calculation an error of $\Delta\theta_{^{12}\text{Be}-n} \sim 3 \text{ mrad}$

- β_n

From the velocity measurement of LAND an uncertainty of $\Delta\beta_n \sim 10^{-4}$ has been considered.

- $\beta_{^{12}\text{Be}}$

To calculate this systematic uncertainty, we have considered the error introduced by the energy loss in the target. At first approximation it can be considered that the velocity(β) distribution inside the target is rectangular, such a data distribution follows $\sigma = \frac{D^2}{12}$ (see figure A.1). Therefore considering the uncertainty of β as half of the width of the distribution, $D = 2\Delta\beta_{^{12}\text{Be}}$; we obtain that $\sigma = \frac{\Delta\beta_{^{12}\text{Be}}}{\sqrt{3}}$, considering our ToF resolution for the velocity we get a value for the systematic uncertainty in the distribution of $\Delta\beta_{^{12}\text{Be}} \sim 10^{-4}$

A. Error calculations

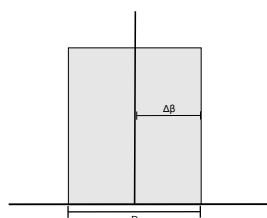


Figure A.1: $\beta_{fragment}$ distribution inside the target

The error propagation of the relative energy calculation is dominated mainly by the error in the angle between the fragment and the neutron. The result of the uncertainty calculation is shown in figure A.2, within the ranges used in this work for the relative energy.

Besides the systematic errors explained above, the statistical errors have been also propagated from the direct measurements ($\sigma = \sqrt{N}$), in the error bars shown in the relative energy in all the figures. The absolute errors given in figure 5.14 for the position of the resonances in ^{13}Be are calculated by quadratical addition including the statistical uncertainties from the fits, which include the error bars, and the systematic uncertainties propagated as explained in this appendix.

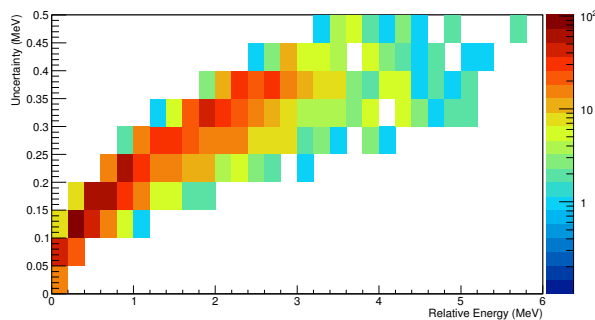


Figure A.2: Calculated uncertainties for all the events used in the results of this work, these goes from 150 - 400 keV in the areas where certain results have been proposed.

B Summary

B.1 Introduction

Light nuclei close to the dripline are weakly bound, thus in general they do not have particle-bound excited states, nevertheless it is possible to feed excitations in the continuum. It is even possible to produce and observe certain combinations of protons and neutron that are beyond the dripline, such systems without bound states are known as unbound nuclei.

At the limit of the dripline, new structures like the halo, Borromean nuclei emerges. The Borromean structure is bound while the two possible subsystems, isotope + nucleon or nucleon + nucleon are unbound. Hence, this produces certain pairs of isotopes where the nucleus with odd number of neutrons is unbound while the nucleus with even number of neutrons is bound. Thus, in order to understand this exotic structure, it is necessary to study these unbound systems.

The theoretical nuclear models, due to the difficulties of the many-body problem, are still not able to describe in a general way the nuclear force. The unbound systems are laboratories to test these theoretical models for the interaction between a core and single neutron above or on the limits of the nuclear force.

The aim of this work is to determine the shell structure of ^{13}Be , a neutron-rich unbound nucleus, using a knockout ($p, 2p$) reaction. This Beryllium isotope has been controversial over the last years, being the target of several studies due to its interest as the middle step between the ^{14}Be Borromean nuclei and its core ^{12}Be . Studying this nucleus has been complicated due to the difficulties to unambiguously determine some of the resonance positions because of the inability of the analysis method (invariant mass) to make a difference between the decays of ^{13}Be to excited states or ground state of ^{12}Be . In order to avoid these ambiguities it is necessary to measure in coincidence the emitted gamma rays from ^{12}Be excited states. The experiment studied in this work includes a gamma ray detector, unlike all previous experiments except one [33].

B. Summary

The reaction channel used to populate the isotope of interest is $^{14}\text{B}(p, 2p)^{13}\text{Be}$, where the Boron beam impinge on a CH_2 target and a proton is knocked out from the beam-isotope and other from the target, producing ^{13}Be . At the high energies used in the experiment (490 MeV/u), the reaction can be considered as Quasifree scattering. In first approximation other kind of interactions do not need to be taken into account and, therefore the two protons are emitted in the same plane with an opening angle of $\sim 82^\circ$ in the laboratory frame whereas the rest of the projectile and the target are not involved in the reaction process, acting as spectators.

Only two experiments have used before ^{14}B as a beam, and none of the previous works have included Quasifree scattering conditions in their reaction.

B.2 Experimental setup

The data used in this thesis were taken during the S393 experiment performed in the late summer of 2010 at GSI Helmholtzzentrum für Schwerionenforschung GmbH by the R3B Collaboration.

At GSI a gas injected into an ion source produces the primary beam which is injected in the linear accelerator (UNILAC) and sent to the synchrotron (SIS18) in order to reach higher energies, for this experiment the primary beam of ^{40}Ar was accelerated to 490 MeV/u. When the beam is extracted from the accelerator it is let to impinge on a light primary target of Beryllium (4.011 g/cm^2) producing a cocktail of particles which go through the Fragment Separator (FRS) that select the species of interest sending them on to the R3B experimental hall: Cave C, where the detectors are placed.

The main feature of this detector setup is that it is capable of making complete kinematic measurements, this means that is able to record all the information including energy, mass and charge from the incoming isotope and outgoing reaction products. The setup can be divided in three different stages following the position and purpose of the detectors: Incoming, around the target and outgoing (see figure B.1 for a schematic view of the setup).

- **Incoming beam detectors**

This part of the setup is responsible of the identification of the different isotopes coming in from the Fragment Separator. The PSP detector is a square plate of silicon which measures the energy loss of the nuclei in order to identify the charge. One scintillator in the last section of the FRS (S8) and another at the entrance of the experimental hall (POS) determines the Time of Flight of the isotopes to distinguish the mass-to-charge ratio. The combination of these measurements allows us to identify the incoming nuclei of the beam that reach the R3B setup. In this stage of the setup there is also a detector to

B.2. Experimental setup

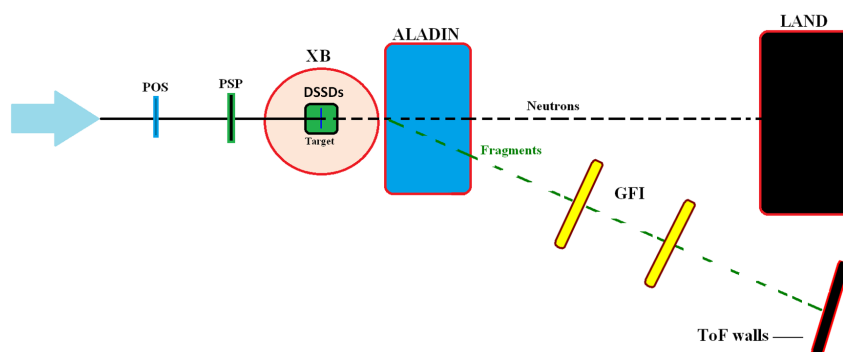


Figure B.1: Simplified schematic view of the S393 experimental setup in Cave C at GSI, the figure 2.5 has a more detailed representation.

constrain the beam size, the ROLU; a combination of four scintillators that can be adjusted to the required beam size, if a particle produces a signal in one of the scintillators, that event is discarded.

- **Around the target detectors**

In the experiment three different targets were used: Carbon (935 mg/cm^2), Lead (2145 mg/cm^2) and the most relevant for this thesis, Polyethylene (CH_2 922 mg/cm^2). These targets are fixed to a wheel which allows their selection online without entering the experimental hall. Close to them, there are four DSSDs, two in front of the target and two behind, with the purpose of measuring the incoming and outgoing angle of interaction with the target. They are also in charge of measuring the energy loss of the outgoing fragments in order to identify the charge. Surrounding the target and the silicons there is Crystal Ball, a spherical detector consisting of 162 NaI scintillators with the purpose of detecting the gamma rays emitted after the reaction, it is also capable of measuring the two protons knocked out in the (p, 2p) reactions.

- **Outgoing fragments detectors**

After the target there is a large electromagnetic dipole called ALADIN that bends the trajectories of the charged particles coming out from the reaction. The nucleus fragments are directed to a pair of fiber detectors (GFI) in order

B. Summary

to track the trajectories and to a scintillator wall (TFW) for measuring the time of flight and the energy loss of each nucleus. The neutron trajectory is not bend by the magnet, therefore they continue straight forward until reaching a bigger scintillator wall (LAND) that measures the time of flight, energy and direction of the neutrons emitted in the reaction.

B.3 Analysis method

In order to extract information about the structure of ^{13}Be we have followed the invariant mass method. The idea behind, is the reconstruction of the energy of the nucleus from the detection of the fragment ^{12}Be and the neutron, however if the ground state mass of those components is subtracted, the relative energy of the compounds is kept which gives information about the different resonances fed of the unbound ^{13}Be .

$$E_{rel} = \sqrt{M_{^{12}\text{Be}}^2 + m_n^2 + 2 \cdot m_n M_{^{12}\text{Be}} \gamma_n \gamma_{^{12}\text{Be}} [1 - \beta_n \beta_{^{12}\text{Be}} \cdot \cos(\theta_{^{12}\text{Be}-n})]} - M_{^{12}\text{Be}} - m_n$$

The equation shows that only three parameters are relevant: the angle between the outgoing fragment (^{12}Be) and the neutron ($\theta_{^{12}\text{Be}-n}$), and the velocity of each ($\beta_n, \beta_{^{12}\text{Be}}$). The procedure to extract those parameters is the following; from the cocktail beam of the FRS the ^{14}B must be selected avoiding contamination from other isotopes. From the reaction products, the $Z=4$ charge (Beryllium) must be found using the DSSDs behind the target and the TFW at the end of the setup. The complete kinematics detection system allows to separate the different masses of the reaction products, thus the $A=12$ mass must be selected as well. Once the fragment has been isolated, the next step is choosing the events with only one neutron in LAND. After this procedure, the reaction channel is cleaned up and the angle and the velocities can be extracted to calculate the relative energy.

The excitation spectrum obtained shows several peaks that can be identified as resonances in ^{13}Be . In order to determine their positions and widths they are fitted using Breit-Wigner functions capable to describe these states,

$$\frac{d\sigma}{dE} \sim \frac{\Gamma(E)}{(E_r - E)^2 + \frac{\Gamma(E)^2}{4}}$$

where,

$$\Gamma(E) = 2\gamma^2 P_i(\rho, \eta).$$

The Breit-Wigner expression has only two free parameters to be fitted: the reduced width of the resonance γ , and the resonance energy E_r . The function obtained has to be folded with the detector resolution.

B.3. Analysis method

The neutron emission of the unbound ^{13}Be can feed several states of the ^{12}Be daughter nucleus. In order to clarify the ^{13}Be structure the invariant mass method is not enough because the relative energy spectrum only shows the energy between the neutron and the fragment, but it cannot distinguish different excitation states of ^{12}Be . Unless the only fed state of the fragment is the ground state, the measurement has to be complemented with gamma-ray detection, otherwise different ^{13}Be resonances decaying to different ^{12}Be states will contribute to the same relative energy peak of the spectrum.

^{12}Be has three possible excited states in the energy range of this analysis, thus two possible gamma rays at 2.1 and 2.7 MeV can be measured. The third state at 2.24 MeV is an isomeric state with a long lifetime and it would escape Crystal Ball before decaying and avoid detection.

A gamma ray peak was found at 2.15 ± 0.02 MeV which corresponds to the 2.1 MeV gamma-ray transition of the excited state of ^{12}Be . The next step is to find a correlation between the gamma ray and any of the resonances found in the $^{12}\text{Be} + n$ relative energy spectrum. The gamma ray peak has been gated-on but the result is dominated by uncorrelated counts, in order to clean it, the spectrum has been gated off-peak on both sides and with the two resulting spectra, a mean has been performed. Later the off-peak mean spectrum has been subtracted from the on-peak gated spectrum, the result (see figure B.2) shows two favoured bins at 0.3 and 0.7 MeV.

Even with the low statistics one can certainly draw a conclusion from figure B.2. It seems obvious that there is no correlation with any medium or high energy resonance, as the relative energy spectrum seems rather flat above 1 MeV. However the two bins at 0.3 and 0.7 MeV are obviously favoured after removing the uncorrelated events, although the bin at 0.5 MeV is suppressed. Hence, it can be understood as two possible resonances located around those bins being partially fed by a ^{13}Be state that decays to the 2.1 MeV state in ^{12}Be . However the second bin of the relative energy spectrum at 0.5 MeV is the highest and in figure B.2 is lower than the fourth, as the total amount of counts in the peak area was higher than the amount subtracted from the off-peak events, thus it is possible that this low-energy resonance is still uncorrelated from the gamma ray.

Despite that the requirements for the outgoing channel are very selective (incoming $^{14}\text{B} +$ outgoing $^{12}\text{Be} + n$), observing two outgoing high-energy protons under Quasifree scattering conditions in Crystal Ball would clarify the complete picture of the reaction. The angular correlations of the Quasifree scattering are found, although the number of counts for the relative energy spectrum is lowered from 1257 to 487 in coincidence with two protons in Crystal Ball.

B. Summary

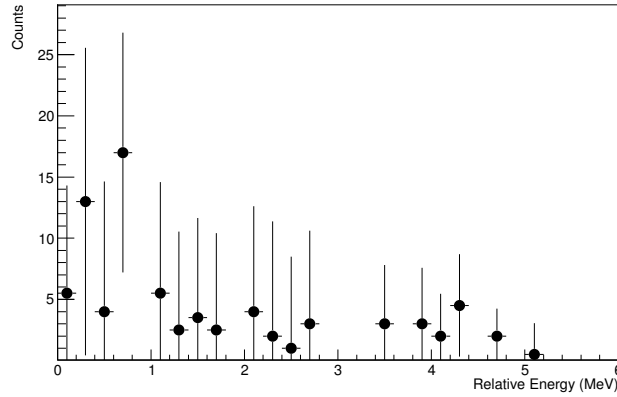


Figure B.2: ^{13}Be Relative energy spectrum after subtraction of the uncorrelated events. The only bins still favoured are the second and the fourth at 0.3 and 0.7 MeV. The dots have been increased in size for a better visualization

B.4 Results

The relative energy of the $^{12}\text{Be} + n$ system has been fitted to several Breit-Wigner functions. We have followed the χ^2 minimization approach to perform the fits, using the MINUIT tool.

Despite the reaction channel should be rather clean after the previous selections, it is likely that there are events within the spectrum that are the result of a wrong identification either from the incoming or outgoing fragment or the neutron detected. In order to take into account such misidentification a Non-resonant Background has been modeled with the following equation. The model has a negative exponential function and an Error Function with three parameters: $A_{1,2,3}$.

$$E_{NR} = A_1 \cdot e^{-A_2 E} \cdot \text{erf}(A_3 E)$$

However the inclusion of this function to the fits makes the results more chaotic and it is not clear that its inclusion made a significant difference to the results.

B.4.1 Considering two resonances

Previous studies have determined only two resonances within the range 0-2.5 MeV for the ^{13}Be nucleus. Thus, although the fifth bin of the histogram shows

B.4. Results

an increment and a significant difference with the sixth bin, we have started considering only two open resonances. A low energy state with $l=0$ and another one close to 2 MeV with $l=2$ are initially considered.

A fit without a non-resonant background has been made, but the result (see figure B.3(a)) shows that the first Breit-Wigner function alone is not capable to make a good approximation for its range. The $\chi^2/N_{df} = 2.24$ indicates the low-quality of this fit.

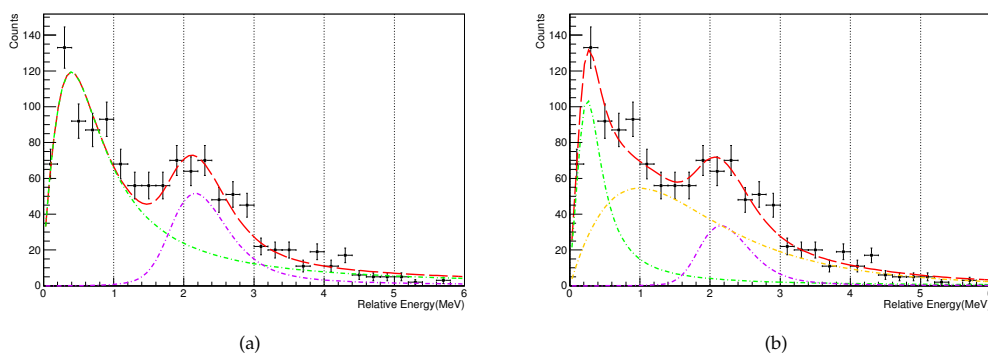


Figure B.3: Visualization of the fits considering two resonances with $l=0$ (green) and 2 (purple). (a): Without including Non-Resonant background.(b): Including Non-Resonant background (yellow). The results of the fit can be seen in table B.1

		Not Including NRB		Including NRB	
#	l	E_r (MeV)	Γ (MeV)	E_r (MeV)	Γ (MeV)
1	0	0.54 ± 0.04	1.185 ± 0.002	0.287 ± 0.038	0.411 ± 0.008
2	2	2.18 ± 0.06	0.381 ± 0.009	2.18(fixed)	0.176 ± 0.034
χ^2		49.26		29.04	
χ^2/N_{df}		2.24		1.32	

Table B.1: Table of results considering two resonances with $l=0,2$. The two cases with and without Non-Resonant Background are included. The visualization of the fit can be seen in figure B.3.

B. Summary

In order to improve the fit, a non-resonant background has been included. To get a result with physical meaning it has been necessary to fix a parameter, the resonance position of the second curve $E_r=2.18\pm 0.06$ MeV. It was chosen because it is the least affected by the inclusion of the background. The results of the fit can be seen in table B.1, the value $\chi^2/N_{df}=1.32$ represents a significant improvement with respect to the previous fit. Even though the background gives a better description of the area 0.7-1.7 MeV, it almost skips the count rise in the 0.9 MeV bin, as can be seen in figure B.3(b), however the description of the low-energy part of the spectrum has improved.

B.4.2 Considering three resonances

Previous publications have considered the inclusion of an s-or-d state in the region between the low energy s-state and the d-state at 2 MeV [46]. In order to reproduce the count increment of the fourth and fifth bin (0.7-0.9 MeV), another Breit-Wigner function has been introduced into the fit, within the energy range 0.6 - 1.2 MeV. The two possible orbital momenta $l=0,2$ have been considered (see figure B.4 and table B.2).

		Not Including NRB		Including NRB	
#	l	E_r (MeV)	Γ (MeV)	E_r (MeV)	Γ (MeV)
1	0	0.265 ± 0.048	0.319 ± 0.013	0.226 ± 0.050	0.195 ± 0.034
2	0	0.929 ± 0.080	0.741 ± 0.029	0.80 ± 0.16	0.743(fixed)
3	2	2.209 ± 0.064	0.635 ± 0.064	2.240 ± 0.072	0.383 ± 0.036
χ^2		24.12		21.89	
χ^2/N_{df}		1.27		1.15	
#	l	E_r (MeV)	Γ (MeV)	E_r (MeV)	Γ (MeV)
1	0	0.333 ± 0.036	0.5196 ± 0.0054	0.262 ± 0.033	0.312 ± 0.007
2	2	0.951 ± 0.055	0.29 ± 0.026	0.838 ± 0.085	0.29(fixed)
3	2	2.157 ± 0.058	0.5845 ± 0.0076	2.241 ± 0.077	0.268 ± 0.036
χ^2		29.9		22.43	
χ^2/N_{df}		1.57		1.18	

Table B.2: Table of results considering three resonances. There are results with two options, considering $l_2=0,2$, as well as including or not the Non-Resonant background. The visualization of the fit can be seen in figure B.4.

The non-resonant background has been included in this case as well, despite it seems less necessary than when considering just two resonances. Here it leads to either unphysical widths of the resonances, specially for the second, or that the non-resonant background vanishes, being so small that it is unnoticeable. In order

B.4. Results

to find a physical solution for these two cases the width of the second resonance has been fixed using the values calculated before without the background.

The result obtained did not lead to significant changes in the resonance positions although there is a noticeable difference in the widths.

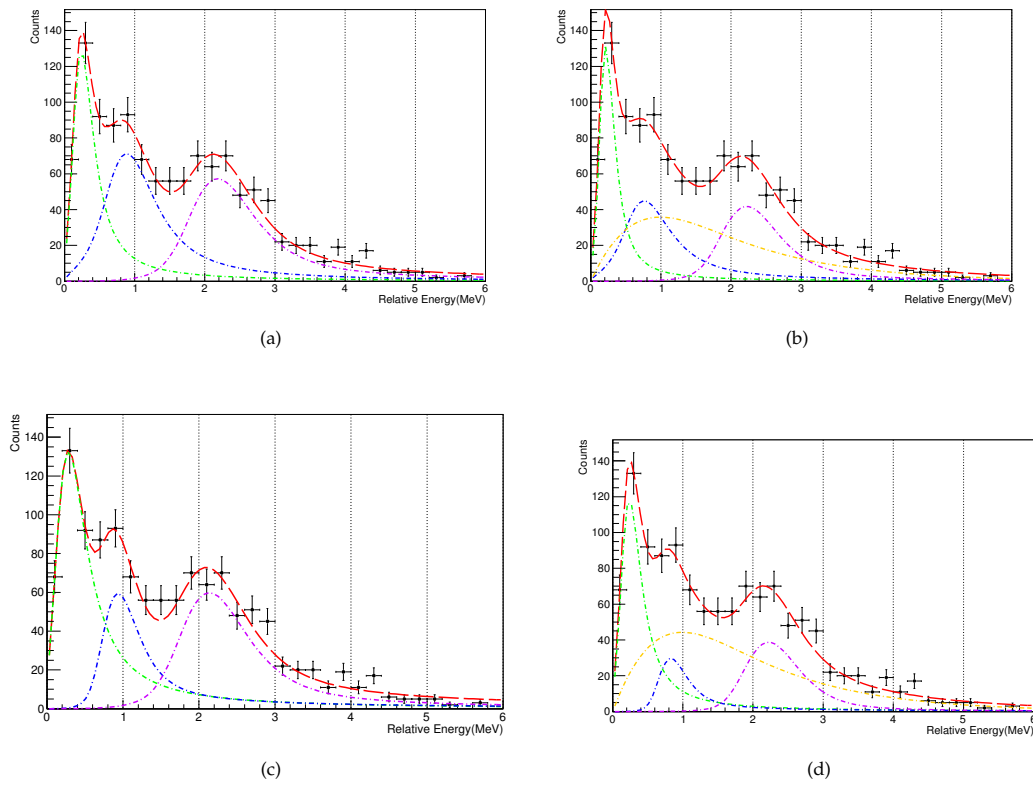


Figure B.4: Visualization of the fits considering three resonances. There are results with two options, considering $l_2=0,2$, as well as including or not the Non-Resonant background. (a): Without including Non-Resonant background and $l=0$ (green), 0 (blue), 2 (purple). (b): Including Non-Resonant background (yellow) and $l=0,0,2$. (c): Without including Non-Resonant background and $l=0,2,2$. (d): Including Non-Resonant background and $l=0,2,2$. The results of the fit can be seen in table B.2.

B. Summary

B.4.3 Considering Quasifree Scattering

Despite the low statistics, the relative energy spectrum of the system $^{12}\text{Be} + \text{neutron}$ imposing Quasifree scattering conditions have also been studied. The angular correlations conditions for the two protons in Crystal Ball has been $60^\circ < \Theta_{Op.Angle} < 110^\circ$ and $\Delta\phi > 110^\circ$, which has lead to a spectrum with 385 counts (see figure B.5 and table B.3).

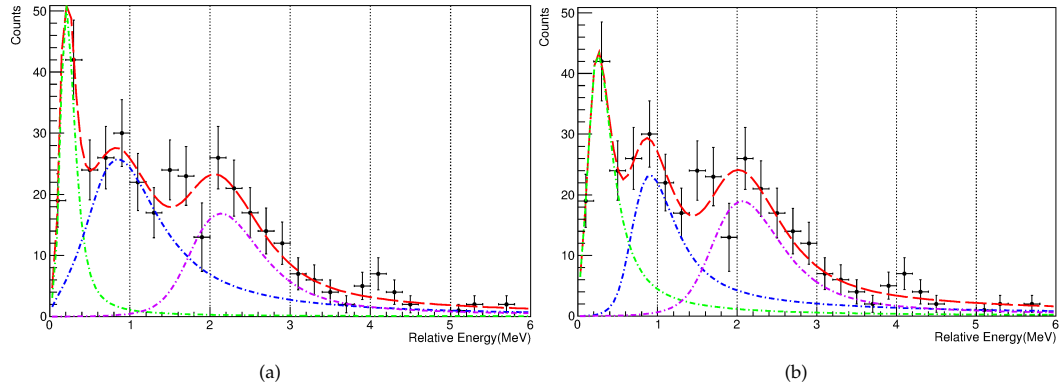


Figure B.5: Visualization of the fits considering three resonances with QFS conditions and considering the two options of $l_2=0,2$. (a):In this case $l=0$ (green), 0 (blue) and 2 (purple). (b):This case considered $l=0,2$ and 2 . The results of the fit can be seen in table B.3

There are two main features to be pointed out: The resonance around 0.8-0.9 MeV is more evident, which will help to determine a more realistic width for an assigned resonance, and it is also worth to point out the count reduction within the tenth bin at 1.9 MeV, which suggests the possible split of the broad resonance around 2 MeV in two different resonances peaked around 1.6 MeV and 2.2 MeV. However, none of the previous publications have reported two resonances in the area. Thus, in the following this count suppression will be regarded as a statistical phenomenon, and another resonance will not be considered in the fit.

In order to exclude the influence of the tenth bin at 1.9 MeV the error bars for the tenth bin have been increased. This increment is enough to reach the error limits of the neighbouring bins. Without this change, the resulting fit tends to be unphysical. Such a change is consistent with the assumption of just one resonance in the 2 MeV region and is also supported by comparing with the relative energy spectrum obtained requiring two protons in Crystal Ball.

B.5. Discussion

#	l	$E_r(\text{MeV})$	$\Gamma(\text{MeV})$
1	0	0.214 ± 0.083	0.12 ± 0.16
2	0	0.92 ± 0.17	1.03 ± 0.24
3	2	2.16 ± 0.21	0.54 ± 0.20
χ^2		12.85	
χ^2/N_{df}		0.75	
#	l	$E_r(\text{MeV})$	$\Gamma(\text{MeV})$
1	0	0.279 ± 0.054	0.322 ± 0.015
2	2	0.95 ± 0.16	0.53 ± 0.23
3	2	2.08 ± 0.17	0.547 ± 0.087
χ^2		13.9	
χ^2/N_{df}		0.82	

Table B.3: Table of results considering three resonances with QFS conditions. There are results with two options, considering $l_2=0,2$. The visualization of the fit is in figure B.5.

In this case, including a non-resonant background has also been tried but the result has been even more chaotic than for the three resonances situation and is likely to be not necessary after requiring the Quasifree scattering conditions.

B.5 Discussion

In order to start the discussion it is necessary to remember certain assumptions that have been made for the analysis.

Previous studies of the incoming nucleus or projectile ^{14}B [87][88] have reported the domination of the components $2s_{1/2}$ and $2d_{5/2}$ on the valence neutron configuration that should be intact after the reaction $^{14}\text{B}(p,2p)^{13}\text{Be}$ of this experiment. That is why only s or d states were considered as options for the analysis.

The resonances at 0.3 MeV and 2 MeV with $1/2^+$ and $5/2^+$ character has been found in several previous publications, that is why two resonances with such angular momentum ($l=0,2$) in those regions have always been considered.

The scenarios presented in the result section are only coincident in the position of the last resonance ~ 2.15 MeV. However the first resonance value ranges from 0.214 to 0.54 MeV but such a higher value is too far from the previous measurements for the first $1/2$ s-state, and therefore is discarded whereas lower values are accepted.

The assumption of a resonance around 0.8-0.9 MeV is clearly supported after imposing the QuasiFree scattering conditions, where a peak in that position is

B. Summary

clearly favoured. The two latest publications considered the possibility of such a state as well, although the momentum profile analysis performed by Aksyutina[43][45] and the theoretical calculations performed by Randisi [46] do not permit a $l_2=0$ state.

At this stage, it is important to remark what has been found in the gamma-ray analysis. The obtained result is quite different from the only other work published that has measured gamma rays in coincidence with the ^{12}Be fragment and one neutron, Kondo et al [33]. In our data we have only found one of the two possible gamma rays emitted from the excited states of ^{12}Be : 2.1 MeV whereas Kondo et al claimed to see the 2.7 MeV gamma ray as well. This might in our case be due to the lack of statistics. But this is not the only relevant difference between both measurements. The authors of [33] inform that the 2.1 MeV gamma ray was correlated with events at very low relative energies of ~ 0.2 MeV or less, whereas in this work the same gamma ray has been correlated only with a resonance close to 0.7 MeV (see figure B.2). The last remark that must be done about the gamma-ray measurement is that the ^{12}Be 2.1 MeV state is a 2^+ , therefore the feeding of this state must origin from an s or d state.

The presence of the coincidence between the 2.1 MeV gamma ray and a peak in the relative energy at 0.7 MeV makes evident that there is a resonance of ^{13}Be that decays to the 2.1 MeV ^{12}Be state. Therefore, despite there is a visible difference in the feeding of the bins at 0.7 MeV and 0.9 MeV in the relative energy coincidence spectrum (figure B.2), their uncertainties in that area are between 200-250 keV (see Appendix A) and the amount of statistics is quite low. Thus we consider the peak of the relative energy spectrum located at ~ 0.95 MeV as coming from a resonance state at $2.1 \text{ MeV} + 0.95 \text{ MeV} \simeq 3.05 \text{ MeV}$. In order to feed the 2^+ state at 2.1 MeV of ^{12}Be , the neutron of ^{13}Be should be emitted from a state with momentum character $1/2^+$ or $5/2^+$.

A resonance at ~ 3.05 MeV is 0.35 MeV above the 2.7 MeV state 1^- of ^{12}Be and 0.8 MeV above the 2.24 MeV 0^+ isomeric state, thus they are energetically allowed for feeding. However in our relative energy spectrum, we have not found a peak at 0.35 MeV in coincidence with a 2.7 MeV gamma ray and we would not be capable to distinguish a different peak at 0.8 MeV from the one at 0.95 MeV. Assuming $J^p=5/2$ for this resonance at ~ 3.05 MeV would make those states of ^{12}Be almost forbidden. Although previous measurements have reported about a $1/2$ state close to 2.9 MeV [43] [42][38]. Therefore we cannot conclude a definitive momentum between $1/2$ and $5/2$.

B.5. Discussion

Regardless of the previous argumentation, there exists the possibility that the resonance peak at 0.95 MeV is hiding two real-resonances of ^{13}Be , one at the position determined in the Breit-Wigner fits (0.95 MeV) whose momentum character is not obvious, although it would be consider as $5/2$, as was previously discussed, whereas the other resonance would be located at $0.7 \text{ MeV} + 2.1 \text{ MeV} \simeq 2.8 \text{ MeV}$ and it would have the same open momentum interpretation of the similar proposed state at 3.05 MeV ($1/2$ or $5/2$).

Figure B.6 represents the structure suggested by this work, supported by our data analysis, the fit results and the discussion. The fit closer to this conclusion is the one displayed in figure B.5(b) whose results are in table B.3. Although the third resonance ($\sim 2.15 \text{ MeV}$) has a worse position determination with the Quasifree scattering statistics, therefore its positions has been settled following the fit of table B.2 and figure B.4(c).

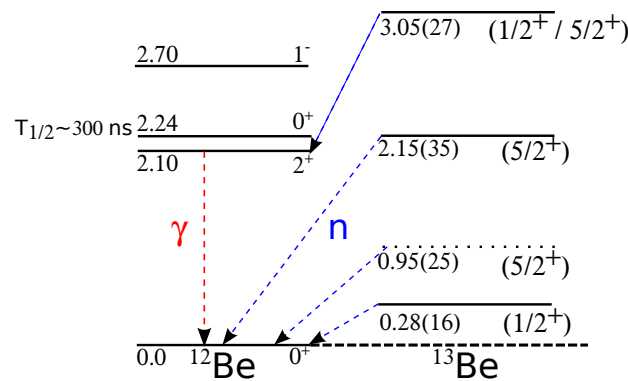


Figure B.6: ^{13}Be structure proposed by this work. The neutron emissions are indicated in blue, whereas the only gamma ray detected is indicated in red. The dotted line indicates the possible state at 0.95 MeV. The dashed black line indicates the ground state of the ^{12}Be . As explained in the text, the ^{13}Be resonance at 3.05 MeV might be decaying to the 0^+ state at 2.24 MeV of ^{12}Be , however is impossible to confirm with the detector setup of this experiment. The error of the energy resonance positions are calculated by quadratical addition of the statistical error from the fit and the systematic error as explained in the Appendix A.

B. Summary

B.6 Conclusions

- The work reports on several possible resonant states of the unbound nucleus ^{13}Be and confirms some of the previously measured: One at 0.28 MeV with orbital angular momentum $l=0$ and another resonance with $l=2$ around 2.15 MeV. One feature at 0.95 MeV has also been found, this state must be interpreted in coincidence with the gamma-ray measurement. See figure B.6 for the proposed ^{13}Be structure. Figure B.5(b) and table B.3 hold the best fit to the proposed values, except for the resonance at 2.15 MeV whose value is taken from table B.2 and figure B.4(c).
- This is the first time that an experiment reports on the measurement of the unbound ^{13}Be nuclear structure using $(p,2p)$ reactions under Quasifree scattering conditions.
- This is the second time that an experiment studying ^{13}Be has included a gamma-ray measurement. The results obtained are different from the previous work [33]. In our work the 2.1 MeV gamma ray from ^{12}Be has been found in coincidence with a peak at ~ 0.95 MeV of the relative energy of the system $^{12}\text{Be} + \text{neutron}$. This peak is therefore interpreted as a ^{13}Be resonance at 3.05 MeV with a momentum character of $1/2^+$ or $5/2^+$.
- The lack of statistics as well as the broad relative energy resolution, especially above 3 MeV, has made impossible to extract more definitive conclusions. Despite this problems, this work has been capable of confirming previous results and proposing new resonances using the reaction $^{14}\text{B} (p,2p)^{13}\text{Be}$.
- The non-resonant background has not been found necessary in this case.

B.7 Future prospects

- The resonance fit around 0.95 MeV in coincidence with the 2.1 MeV gamma ray might be understood as a combination of a resonance around 0.95 MeV and another one at $2.1 \text{ MeV} + 0.7 \text{ MeV} \sim 2.8 \text{ MeV}$. The state at 0.95 MeV (dashed line in figure B.6) would be $5/2^+$ as has been settled in previous publications [43][46] whereas the state at 2.8 MeV could be $1/2$ or $5/2$. This possibility should be checked in a future experiment.
- An improvement in every part of the setup used is currently under development for the FAIR facility. The gamma measurement will be improved by the new detector CALIFA. The protons coming out from the reaction will be much easily detected with the Silicon Tracker as well as CALIFA, improving the efficiency and energy resolution. NeuLAND will take care of the neutrons and

B.7. Future prospects

will help to improve the angular resolution which is the main constrain for the relative energy determination. These new detectors in combination with far more intense radioactive beams will help to improve the results obtained.

- Besides the resolution, efficiency and beam intensity improvements already planned, there is no information about the possible feeding to the other 0^+ isomeric state of the ^{12}Be at 2.24 MeV. An experiment capable of measuring a long-lived state after producing ^{13}Be would contribute further to the current knowledge about this exotic nucleus.

B. Summary

C Resumen en castellano

C.1 Introducción

Los núcleos ligeros cerca de la línea de goteo están muy debilmente ligados, por tanto, por lo general no tienen estados ligados excitados, sin embargo si que es posible poblar excitaciones en el continuo. Incluso es posible producir y observar ciertas combinaciones de protones y neutrones que están más allá de la línea de goteo, tales sistemas que carecen de estados ligados son conocidos como núcleos no-ligados.

En los límites de la línea de goteo, aparecen otras estructuras como los núcleos halo Borromeos. Esta estructura es ligada mientras que los dos subsistemas que lo forman, isótopo + nucleón o nucleón + nucleón son no-ligados. Esto produce determinados pares de isótopos donde el que tiene un número impar de neutrones no está ligado, mientras que el que tiene un número par, si lo está. Por lo tanto, para entender este tipo de estructuras exóticas es necesario estudiar los sistemas no-ligados.

Los modelos teóricos nucleares, debido a las dificultades que entraña el problema de muchos-cuerpos, todavía no son capaces de describir de forma general la fuerza nuclear. Los sistemas no-ligados son laboratorios donde probar los modelos teóricos para la interacción entre un núcleo y un solo neutrón en los límites de la fuerza nuclear.

El objetivo de este trabajo es el estudio de la estructura de capas del ^{13}Be , un núcleo no-ligado rico en neutrones, utilizando una reacción $(p,2p)$ de *knockout*. Este isótopo de Berilio ha sido controvertido a lo largo de los últimos años, lo que le ha convertido en el objetivo de varios estudios, debido a su interés como paso intermedio entre el núcleo Borromeo ^{14}Be y el ^{12}Be . Estudiar este núcleo se ha complicado debido a la dificultad de determinar inequívocamente algunas de las posiciones de sus resonancias, por la incapacidad del método de análisis (masa invariante) de diferenciar entre decaimientos del ^{13}Be a estados excitados o al estado

C. Resumen en castellano

fundamental del ^{12}Be . Para evitar estas ambigüedades es necesario medir en coincidencia los rayos gamma de los estados excitados del ^{12}Be . El experimento que se estudia en este trabajo incluye un detector de rayos gamma, a diferencia de todos los experimentos previos excepto uno [33].

El canal de reacción utilizado para poblar el isótopo de interés es $^{14}\text{B}(p, 2p)^{13}\text{Be}$, donde el haz de Boro se hace incidir sobre un blanco de polietileno CH_2 , provocando la pérdida de un proton en el haz y produciendo ^{13}Be . A las altas energías utilizadas en el experimento (490 MeV/u), la reacción se puede considerar como dispersión *cuasi-libre*. En primera aproximación, no es necesario tener en cuenta otro tipo de interacciones y por lo tanto, los dos protones son emitidos en el mismo plano con un ángulo de apertura de $\sim 82^\circ$ en el sistema de referencia del laboratorio, mientras que el resto del proyectil y el blanco no están involucrados, actuando como espectadores.

Sólo dos experimentos han utilizado ^{14}B como haz y ninguno de los trabajos previos ha incluido condiciones de dispersión *cuasi-libre* en su reacción.

C.2 Montaje experimental

Los datos utilizados en esta tesis se tomaron durante el experimento S393 realizado a finales del verano de 2010 en la instalación GSI Helmholtzzentrum für Schwerionen-Forschung GmbH por la colaboración R3B.

En GSI un gas inyectado en una fuente de iones produce el haz primario que comienza a acelerarse en el acelerador lineal (UNILAC), tras eso es enviado a un sincrotrón (SIS18) con el fin de llegar a energías más altas, para el experimento S393 el haz primario era de ^{40}Ar con energías de 490 MeV/u. Al extraer el haz del acelerador, este incide sobre un blanco ligero de Berilio de 4.011 g/cm^2 , produciéndose un cóctel de partículas que pasa a través del separador de fragmentos (FRS) donde las distintas especies son separadas y seleccionadas antes de enviarlas al área experimental de R3B: Cave C, donde los detectores están preparados.

La característica principal de este montaje experimental es que es capaz de hacer mediciones de cinemática completa, lo que significa que puede registrar toda la información, incluyendo energía, masa y carga del isótopo entrante y los productos de reacción salientes. Los detectores pueden dividirse en tres etapas distintas según su posición y propósito: Detectores de entrada, alrededor del blanco y a la salida (la figura C.1 muestra un esquema del montaje experimental).

- **Detectores de entrada**

Esta parte del montaje es responsable de la identificación de los diferentes isótopos que llegan desde el separador de fragmentos. El detector PSP es una placa cuadrada de silicio que se encarga de medir la pérdida de energía de los núcleos para identificar su carga. Un centelleador en la última sección del

C.2. Montaje experimental

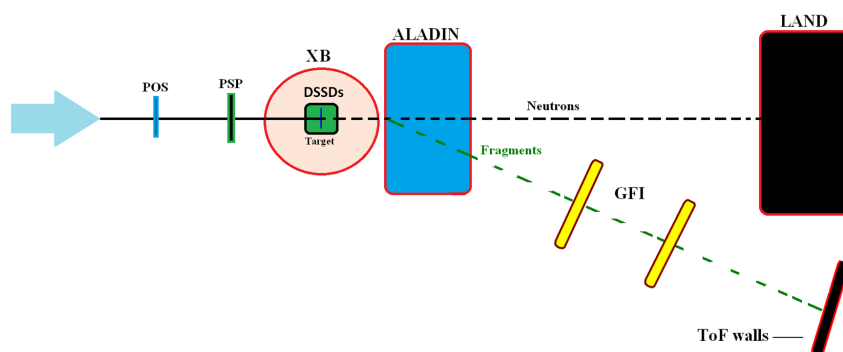


Figure C.1: Esquema simplificado del montaje experimental del experimento S393 en la Cave C de GSI, la figura 2.5 tiene una representación más detallada.

FRS (S8) y otro a la entrada del area experimental (POS) se encargan de medir el Tiempo de Vuelo de los isótopos para distinguir la relación de carga-masa. La combinación de ambas mediciones nos permite identificar los núcleos entrantes del haz que alcanzan el montaje de R3B. En esta etapa también existe un detector encargado de restringir el tamaño del haz, el ROLU; una combinación de cuatro centelleadores que se pueden ajustar al tamaño requerido del haz, de forma que si una partícula produce señal en uno de los centelleadores, el evento es descartado.

- **Alrededor del blanco**

En el experimento se utilizaron tres blancos distintos: Carbono (935 mg/cm^2), Plomo (2145 mg/cm^2) y el más relevante para esta tesis, Polietileno (CH_2 con 922 mg/cm^2). Los blancos están fijados a una placa circular que permite escogerlos electrónicamente, sin necesidad de entrar en el area experimental. Cerca de los blancos, hay cuatro detectores de silicio de doble cara (DSSDs), dos delante de los blancos y dos detrás, cuyo propósito es medir el ángulo de de entrada y salida de interacción de las partículas con el blanco. También se encargan de medir la pérdida de energía de los fragmentos salientes para identificar su carga. Alrededor del blanco y los detectores de silicio, está Crystal Ball, un detector esférico consistente en 162 centelleadores de NaI, con el propósito de detectar los rayos gamma emitidos tras la reacción, también es capaz de medir los protones salientes de las reacciones (p, 2p).

C. Resumen en castellano

- **Detectores de salida**

Tras el blanco hay un gran dipolo magnético llamado ALADIN, que se encarga de curvar las trayectorias de las partículas cargadas que son producto de la reacción. Los fragmentos son dirigidos por el imán a través de un par de detectores de fibras (GFI) para medir dicha trayectoria, al final alcanzan un muro de centelleadores llamado TFW que se encarga de medir el tiempo de vuelo desde el blanco y la pérdida de energía de cada núcleo, permitiendo también identificación de carga. La trayectoria de los neutrones no se curva y continúan en línea recta hasta alcanzar otro muro de centelleadores, LAND, que también mide tiempo de vuelo, energía y la dirección seguida por los neutrones.

C.3 Métodos de análisis

Con el fin de extraer información sobre la estructura de ^{13}Be se ha seguido el método de masa invariante. La idea es la reconstrucción de la energía de los núcleos a partir de la detección del fragmento de ^{12}Be y el neutrón perdido. Sin embargo, si a la energía que llevan se le resta la masa en reposo del fragmento y el neutrón, la resultante es un espectro de energía relativa que da información de las resonancias del núcleo no-ligado ^{13}Be .

$$E_{rel} = \sqrt{M_{12\text{Be}}^2 + m_n^2 + 2 \cdot m_n M_{12\text{Be}} \gamma_n \gamma_{12\text{Be}} [1 - \beta_n \beta_{12\text{Be}} \cdot \cos(\theta_{12\text{Be}-n})]} - M_{12\text{Be}} - m_n$$

La ecuación muestra que sólo tres parámetros son relevantes; el ángulo entre el fragmento saliente (^{12}Be) y el neutrón ($\theta_{12\text{Be}-n}$), y la velocidad de cada uno ($\beta_{12\text{Be}}, \beta_n$). El procedimiento para obtener dichos parámetros es el siguiente: Del haz entrante del FRS debe ser seleccionado el núcleo de ^{14}B , evitando contaminantes de otros isótopos. De los productos de reacción se debe seleccionar la carga $Z=4$ (Berilio) mediante los silicios DSSDs que hay detrás del blanco y el TFW al final del montaje. Utilizando el sistema de detectores de cinemática completa es posible separar los fragmentos salientes de reacción según sus masas y de esta forma se debe seleccionar las masas $A=12$. Una vez el fragmento ha sido aislado debemos escoger los eventos que incluyan un sólo neutrón en LAND y por lo tanto el canal de interés estará limpio y podremos extraer el ángulo y las velocidades de cada componentes para calcular la energía relativa.

El espectro de energía relativa que hemos calculado muestra un conjunto de picos que pueden ser identificados como resonancias del ^{13}Be . Para poder fijar sus posiciones y anchuras, estas son ajustadas mediante funciones Breit-Wigner, que son capaces de describir estos estados,

C.3. Métodos de análisis

$$\frac{d\sigma}{dE} \sim \frac{\Gamma(E)}{(E_r - E)^2 + \frac{\Gamma(E)^2}{4}}$$

donde,

$$\Gamma(E) = 2\gamma^2 P_l(\rho, \eta).$$

La función Breit-Wigner sólo tiene dos parámetros libres para ajustar; la anchura reducida de la resonancia γ y la energía de la resonancia E_r . La función obtenida tiene que introducir también la resolución de los detectores.

La emisión de neutrones del núcleo no-ligado ^{13}Be puede poblar varios estados del núcleo hijo ^{13}Be . Para aclarar la estructura del ^{13}Be , el método de la masa invariante no es suficiente, porque el espectro solo muestra la energía entre el fragmento y el neutrón, pero no puede distinguir las excitaciones del ^{12}Be . A menos que sólo se haya poblado el estado fundamental del fragmento, la medida debe ser complementada con detección de rayos gamma, sino algunas de las resonancias del ^{13}Be que decaigan a distintos estados del ^{12}Be contribuirán al mismo pico del espectro de energía relativa y se confundirán.

^{12}Be tiene tres estados excitados posibles en el rango de energía de este análisis, por tanto se pueden medir dos rayos gamma a 2.1 y 2.7 MeV. El tercer estado a 2.24 MeV es isomérico y tiene una vida-media larga, por lo que escapará de Crystal Ball antes de su decaimiento y no podrá ser detectado.

Se ha encontrado un rayo gamma a 2.15 ± 0.02 MeV, que corresponde con el rayo gamma de 2.1 MeV de la transición del estado excitado del ^{12}Be . El siguiente paso es encontrar una correlación entre dicho rayo gamma y cualquiera de las resonancias del espectro de energía relativa de $^{12}\text{Be} + n$. Abriendo una ventana alrededor del rayo gamma en coincidencia con el espectro de energía relativa, el resultado producido está dominado por las cuentas no-correlacionadas presentes. Para poder limpiarlo, se han abierto ventanas de coincidencia a ambos lados del rayo gamma y se ha hecho una media de los espectros de energía relativa que les corresponden, dicha media se ha sustraído de la energía relativa dentro de la ventana de coincidencia con el rayo gamma a 2.1 MeV. El resultado (ver figura C.2) muestra dos divisiones del histograma favorecidas a 0.3 y 0.7 MeV.

Incluso con la baja estadística, se pueden extraer conclusiones de la figura C.2. Parece obvio que no hay correlación con ninguna resonancia a energías altas o medias, puesto que el espectro de energía relativa parece bastante plano por encima de 1 MeV. Sin embargo, las dos divisiones a 0.3 y 0.7 MeV están favorecidas, tras eliminar los eventos no-correlacionados, mientras que la división a 0.5 MeV está suprimida. Por lo tanto, se puede entender que las dos resonancias localizadas en esas divisiones están parcialmente pobladas por alguna resonancia del ^{13}Be que decae al estado a 2.1 MeV del ^{12}Be . Sin embargo, la segunda división del espectro de energías relativas a 0.5 MeV es la más alta y en la figura C.2 es menor que la

C. Resumen en castellano

cuarta división, dado que la cantidad total de cuentas dentro de la ventana de coincidencia con el rayo gamma era mayor que las ventanas a los lados es posible que esta resonancia a baja energía todavía esté descorrelacionada con el rayo gamma medido.

A pesar de que los requisitos previos para el canal de salida son muy selectivos (^{14}B entrante + ^{12}Be saliente + n), observar dos protones salientes de alta energía con condiciones de dispersión cuasi-libre en Crystal Ball, clarificarían la reacción completamente. La correlación angular de dispersión cuasi-libre se ha encontrado, aunque el número de cuentas del espectro de energía relativa ha bajado desde 1257 a 487 cuentas en coincidencia con dos protones en Crystal Ball.

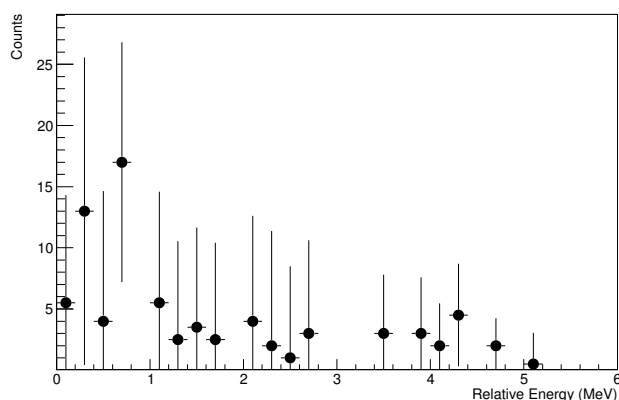


Figure C.2: :Espectro de energía relativa del ^{13}Be tras sustracción de los eventos no correlacionados con el rayo gamma. Las únicas divisiones que aún están favorecidas son la segunda y la cuarta a 0.3 y 0.7 MeV. Los puntos se han aumentado de tamaño para facilitar la visualización.

C.4 Resultados

El espectro de energía relativa del sistema $^{12}\text{Be} + n$ se ha ajustado a a varias funciones Breit-Wigner usando minimización χ^2 con la herramienta MINUIT.

A pesar de que el canal de reacción debería estar bastante limpio tras las condiciones impuestas, es probable que existan eventos en el espectro que sean el resultado de identificaciones incorrectas, tanto del núcleo de entrada como del fragmento de salida o el neutrón. Para tener en cuenta dichas identificaciones erróneas se ha modelizado un fondo no-resonante usando la siguiente ecuación. El modelo tiene una función exponencial y una función Error con tres parámetros: $A_{1,2,3}$.

$$E_{NR} = A_1 \cdot e^{-A_2 E} \cdot erf(A_3 E)$$

Sin embargo la inclusión de esta función a los ajustes ha resultado en ajustes más caóticos y no está claro que su inclusión produzca una diferencia significativa en los resultados.

C.4.1 Considerando dos resonancias

Estudios previos han determinado sólo dos resonancias en el rango de 0-2.5 MeV para el núcleo de ^{13}Be . Por tanto, aunque la quinta división del histograma muestra un incremento y una diferencia significativa con la sexta división, hemos empezado considerando sólo dos resonancias. Un estado a baja energía con $l=0$ y otro cerca de 2 MeV con $l=2$ son considerados inicialmente.

Se ha hecho un ajuste sin el fondo no-resonante pero el resultado (ver la figura C.3(a)) muestra que la primera función Breit-Wigner sola no puede hacer una buena aproximación en su rango. El $\chi^2/N_{df} = 2.24$ indica la baja calidad de este ajuste.

Para mejorar el ajuste, se ha incluido el fondo no-resonante, para conseguir un resultado con significado físico ha sido necesario fijar un parámetro, la posición de la segunda resonancia $E_r = 2.18 \pm 0.06$ MeV. Esta ha sido escogida porque es la menos afectada por la inclusión del fondo. Los resultados del ajuste están en la tabla C.1, donde se puede ver que el valor $\chi^2/N_{df} = 1.32$ ha mejorado significativamente. A pesar de que el fondo da una mejor descripción de la zona entre 0.7-1.7 MeV, este casi ignora el incremento de cuentas de la división de 0.9 MeV, como puede verse en la figura C.3(b), sin embargo la descripción de la parte de baja energía del espectro ha mejorado.

C. Resumen en castellano

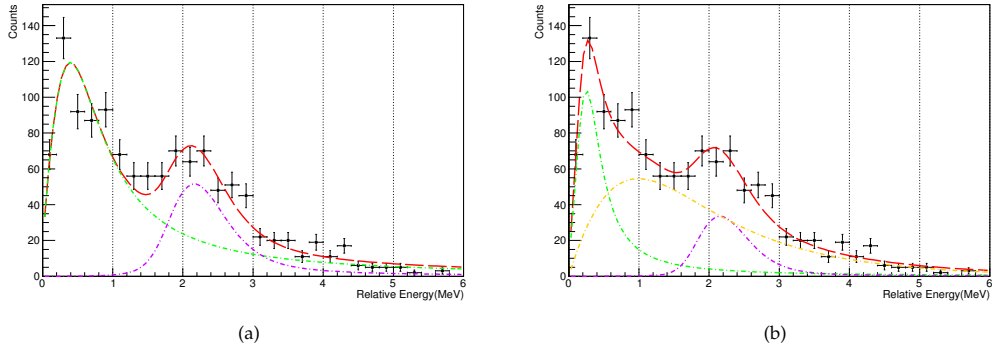


Figure C.3: Visualización del ajuste considerando dos resonancias con $l=0$ (verde), 2 (púrpura). (a): Sin considerar fondo no-resonante. (b): Incluyendo fondo no-resonante (amarillo). El resultado de los ajustes se puede ver en la tabla C.1

		Sin incluir FNR		Incluyendo FNR	
#	l	$E_r(\text{MeV})$	$\Gamma(\text{MeV})$	$E_r(\text{MeV})$	$\Gamma(\text{MeV})$
1	0	0.54 ± 0.04	1.185 ± 0.002	0.287 ± 0.038	0.411 ± 0.008
2	2	2.18 ± 0.06	0.381 ± 0.009	2.18(fijado)	0.176 ± 0.034
χ^2		49.26		29.04	
χ^2/N_{df}		2.24		1.32	

Table C.1: Tabla con los resultados del ajuste considerando dos resonancias con $l=0,2$. Se incluyen los dos casos con y sin fondo no-resonante. La visualización está en la figura C.3.

C.4.2 Considerando tres resonancias

Publicaciones previas han considerado la inclusión de un estado s o d en la región entre el estado s de baja energía y el estado d alrededor de 2 MeV [46]. Para reproducir el incremento de cuentas de la cuarta y quinta división (0.7-0.9 MeV), se ha introducido otra función Breit-Wigner en el ajuste, en el rango de energías de 0.6-1.2 MeV. Se han considerado los dos momentos orbitales posibles $l=0,2$ (mirar la figura C.4 y la tabla C.2).

El fondo no-resonante se ha incluido también en este caso, a pesar de que parece menos necesario que cuando se han considerado dos resonancias. En estos casos, conduce a anchuras no-físicas de las resonancias, especialmente en la segunda

C.4. Resultados

o bien a que el fondo no-resonante desaparece, siendo tan pequeño que es inapreciable. Para ser capaz de encontrar una solución con significado físico para estos dos casos, se ha fijado el valor de la anchura de la segunda resonancia, usando los valores obtenidos sin el fondo no-resonante.

Los resultados obtenidos no han conducido a cambios significativos en la posición de las resonancias, aunque las anchuras si que tienen cambios apreciables.

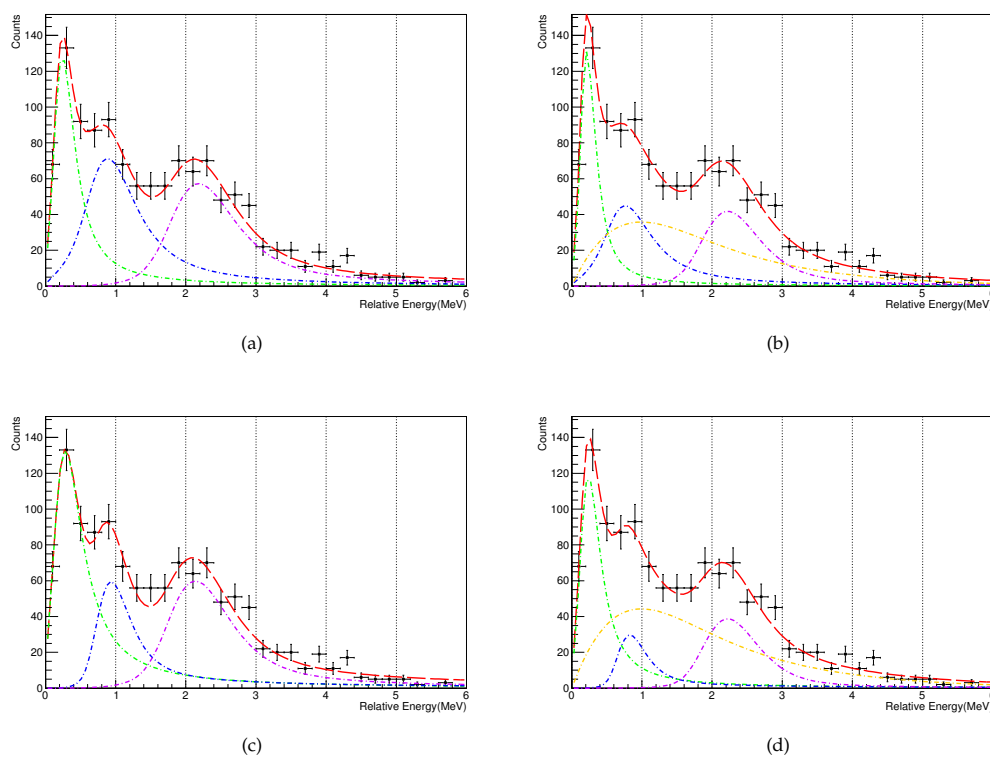


Figure C.4: Visualización del ajuste considerando tres resonancias. Hay resultados con dos opciones, considerando $l_2=0,2$, así como incluyendo o no el fondo no-resonante. (a): Sin incluir fondo no-resonante y $l=0$ (verde), 0 (azul), 2 (púrpura). (b): Incluyendo un fondo no-resonante (amarillo) y $l=0,0,2$. (c): Sin incluir fondo no-resonante y $l=0,2,2$. (d): Incluyendo un fondo no-resonante y $l=0,2,2$. Los resultados del ajuste pueden encontrarse en la tabla C.2.

C. Resumen en castellano

		Sin incluir FNR		Incluyendo FNR	
#	l	$E_r(\text{MeV})$	$\Gamma(\text{MeV})$	$E_r(\text{MeV})$	$\Gamma(\text{MeV})$
1	0	0.265 ± 0.048	0.319 ± 0.013	0.226 ± 0.050	0.195 ± 0.034
2	0	0.929 ± 0.080	0.741 ± 0.029	0.80 ± 0.16	0.743(fijado)
3	2	2.209 ± 0.064	0.635 ± 0.064	2.240 ± 0.072	0.383 ± 0.036
χ^2		24.12		21.89	
χ^2/N_{df}		1.27		1.15	
#	l	$E_r(\text{MeV})$	$\Gamma(\text{MeV})$	$E_r(\text{MeV})$	$\Gamma(\text{MeV})$
1	0	0.333 ± 0.036	0.5196 ± 0.0054	0.262 ± 0.033	0.312 ± 0.007
2	2	0.951 ± 0.055	0.29 ± 0.026	0.838 ± 0.085	0.29(fijado)
3	2	2.157 ± 0.058	0.5845 ± 0.0076	2.241 ± 0.077	0.268 ± 0.036
χ^2		29.9		22.43	
χ^2/N_{df}		1.57		1.18	

Table C.2: Tabla de resultados del ajuste considerando tres resonancias. Hay resultados con las dos opciones, considerando $l_2=0,2$, así como incluyendo o no un fondo no-resonante. La visualización gráfica del ajuste se puede ver en la figura C.4.

C.4.3 Considerando reacción (p,2p) de dispersión cuasi-libre

A pesar del bajo número de cuentas, el espectro de energía relative del sistema $^{12}\text{Be} + \text{neutron}$ imponiendo condiciones de dispersión cuasi-libre (DCL) también ha sido estudiado. Las condiciones que se han impuesto en las correlaciones angulares de dos protones en Crystal Ball han sido: $60^\circ < \Theta_{Op.Angle} < 110^\circ$ y $\Delta\phi > 110^\circ$, conduciendonos a un espectro de de tan solo 385 cuentas (ver la figura C.5 y la tabla C.3).

Hay dos rasgos principales a destacar: La resonancia alrededor de 0.8-0.9 MeV es más evidente, lo que puede ayudar a determinar una anchura más realista para una resonancia en esa posición. También merece la pena mencionar la reducción de cuentas en la décima división a 1.9 MeV, lo que sugiere la posibilidad de dividir la resonancia ancha cerca de 2 MeV en dos resonancias diferentes centradas alrededor de 1.6 MeV y 2.2 MeV. Sin embargo, ninguna de las publicaciones previas han informado acerca de dos resonancias en esa zona. Por lo tanto, a partir de aquí, esta supresión de cuentas será entendido como un fenómeno estadístico y no se considerará otra resonancia en la función de ajuste.

Para excluir la influencia de la décima división a 1.9 MeV, las barras de error de dicha división han sido incrementadas. Este incremento es suficiente para alcanzar los límites de los errores de las divisiones vecinas. Sin este cambio, el resultado del ajuste tiende a ser no-físico Este cambio es consistente con asumir solamente una resonancia en la región de 2 MeV y también está respaldada si se compara con

C.5. Discusión

el espectro de energías relativas que se obtiene al requerir dos protones en Crystal Ball.

En este caso, incluir un fondo no-resonante ha sido probado también pero el resultado ha sido incluso más caótico y es probable que este no sea necesario tras requerir las condiciones de dispersión cuasi-libre.

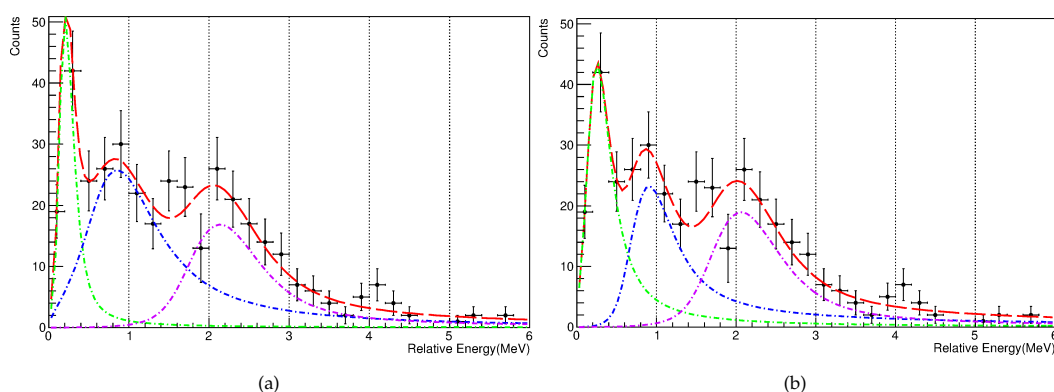


Figure C.5: Visualización del ajuste considerando tres resonancias con condiciones DCL y considerando las dos opciones de $l_2=0, 2$. (a): En este caso $l=0$ (verde), 0 (azul), 2 (púrpura). (b): En este caso se considera $l=0,2,2$. Los resultados del ajuste se pueden encontrar en la tabla C.3

C.5 Discusión

Para comenzar la discusión es necesario recordar ciertas cosas que se han asumido para el análisis.

Los estudios previos del núcleo ^{14}B [87][88] han informado del dominio del componente $2s_{1/2}$ y $2d_{5/2}$ en la configuración de los neutrones de valencia, que debería estar intacto tras la reacción $^{14}\text{B}(p,2p)^{13}\text{Be}$ de este experimento. Esta es la razón por la que sólo se han considerado estados s o d como opciones para el análisis.

Las resonancias alrededor de 0.4 MeV y 2 MeV con carácter $1/2^+$ y $5/2^+$ se han encontrado también en varias publicaciones previas, por ello siempre se han considerado dos resonancias con momento angular $l=0, 2$ en esas regiones de energía.

Todos los escenarios presentados en la sección de resultados sólo coinciden en la posición de la última resonancia ~ 2.15 MeV. Sin embargo el valor de la primera

C. Resumen en castellano

#	l	$E_r(\text{MeV})$	$\Gamma(\text{MeV})$
1	0	0.214 ± 0.083	0.12 ± 0.16
2	0	0.92 ± 0.17	1.03 ± 0.24
3	2	2.16 ± 0.21	0.54 ± 0.20
χ^2		12.85	
χ^2/N_{df}		0.75	
#	l	$E_r(\text{MeV})$	$\Gamma(\text{MeV})$
1	0	0.279 ± 0.054	0.322 ± 0.015
2	2	0.95 ± 0.16	0.53 ± 0.23
3	2	2.08 ± 0.17	0.547 ± 0.087
χ^2		13.9	
χ^2/N_{df}		0.82	

Table C.3: Tabla de resultados considerando tres resonancias con condiciones DCL. Hay resultados con dos opciones, considerando $l_2=0,2$. La visualización del ajuste puede encontrarse en la figura C.5.

resonancia oscila desde 0.214 a 0.54 MeV, pero el valor más alto está lejos de las medidas previas para el primer estado s, por lo tanto se descarta, mientras que los valores menores se aceptan.

Asumir una resonancia alrededor de 0.8-0.9 MeV está claramente respaldado tras imponer las condiciones de dispersión cuasi-libre, puesto que un pico en esa zona es mucho más evidente. Las dos últimas publicaciones consideran la posibilidad de un estado en esa región, pero tanto el análisis de perfil de momento realizado por Aksyutina et al [43][45] como el cálculo teórico realizado por Randisi et al [46] no permiten un estado con $l_2=0$.

En este punto, es importante destacar lo que se ha encontrado en el análisis de los rayos gamma. El resultado obtenido es muy distinto respecto al único trabajo publicado que ha medido rayos gamma en coincidencia con el fragmento de ^{12}Be y un neutrón, Kondo et al [33]. En nuestros datos sólo hemos encontrado uno de los posibles rayos gamma emitidos desde los estados excitados del ^{12}Be : 2.1 MeV mientras Kondo et al afirman ver también el rayo gamma de 2.7 MeV. En nuestro caso, esto se puede deber a la falta de estadística. Pero esta no es la única diferencia relevante entre las dos medidas. Los autores de [33] informan de que el rayo gamma de 2.1 MeV estaba correlacionado con los eventos a muy baja energía relativa de ~ 0.2 MeV o menos, mientras que en este trabajo el mismo rayo gamma se ha correlacionado principalmente con la segunda resonancia cercana a 0.7 MeV (ver figura C.2). Lo último que se debe destacar sobre la medida de rayos gamma es que el estado a 2.1 MeV del ^{12}Be es un 2^+ , por lo tanto este estado debe ser poblado desde un estado s o d.

C.5. Discusión

La presencia de la coincidencia entre el rayo gamma de 2.1 MeV y un pico en la energía relativa a 0.7 MeV, hace evidente la existencia de una resonancia del ^{13}Be que decae al estado de 2.1 MeV del ^{12}Be . Por consiguiente, a pesar de la visible diferencia de población de las divisiones de 0.7 y 0.9 MeV del espectro de coincidencia de energía relativa (figura C.2), las incertidumbres en esa región son 200-250 keV (ver apéndice A) y la estadística es bastante baja. Por lo tanto, consideramos que el pico del espectro de energía relativa localizado a ~ 0.95 MeV proviene de un estado resonante a $2.1 \text{ MeV} + 0.95 \text{ MeV} \simeq 3.05 \text{ MeV}$. Para poblar el estado 2^+ a 2.1 MeV del ^{12}Be , el neutrón del ^{13}Be debe ser emitido desde un estado con momento orbital $1/2^+$ or $5/2^+$.

Una resonancia a ~ 3.05 MeV está 0.35 MeV por encima del estado 1^- a 2.7 MeV del ^{12}Be y 0.8 MeV por encima del estado isomérico 0^+ a 2.24 MeV, por lo tanto son estados permitidos energéticamente. Sin embargo en nuestro espectro de energía relativa, no hemos encontrado un pico a 0.35 MeV en coincidencia con un rayo gamma de 2.7 MeV y no seríamos capaces de distinguir un pico a 0.8 MeV diferente del de 0.95 MeV. Asumiendo $J^p=5/2$ para esta resonancia a ~ 3.05 MeV haría que estos estados del ^{12}Be estuvieran casi prohibidos. No obstante algunas medidas previas han informado sobre un estado $1/2$ cerca de 2.9 MeV [43] [42][38]. Por lo tanto, no podemos concluir un momento angular definitivo entre $1/2$ y $5/2$.

A pesar de la argumentación previa, existe la posibilidad de que el pico a 0.95 MeV esté escondiendo dos resonancias reales del ^{13}Be , una en la posición determinada por los ajustes Breit-Wigner (0.95 MeV), cuyo momento orbital no es obvio, aunque sería considerado $5/2$ como ha sido discutido previamente, mientras que la otra resonancia estaría localizada a $0.7 \text{ MeV} + 2.1 \text{ MeV} \simeq 2.8 \text{ MeV}$ y tendría la misma interpretación abierta del momento propuesta para el estado a 3.05 MeV ($1/2$ o $5/2$).

La figura C.6 representa la estructura sugerida por este trabajo, respaldada por nuestro análisis de los datos, los resultados de los ajustes y la discusión. El ajuste más cercano a esta conclusión es el mostrado en la figura C.5(b) cuyos resultados están en la tabla C.3. No obstante, la tercera resonancia (~ 2.15 MeV) está peor determinada con las estadísticas de dispersión cuasi-libre, por lo tanto su posición ha sido fijada siguiendo el ajuste de la tabla C.2 y la figura C.4(c).

C. Resumen en castellano

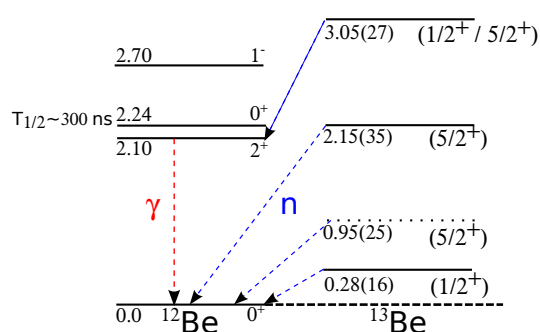


Figure C.6: Estructura del ^{13}Be propuesta por este trabajo. La emisión de neutrones está indicada en azul, mientras que el único rayo gamma detectado se resalta en rojo. La línea punteada indica el posible estado a 0.95 MeV. La línea negra discontinua indica el estado fundamental del ^{12}Be . Como se ha explicado en el texto, la resonancia del ^{13}Be a 3.05 MeV podría decaer al estado 0^+ a 2.24 MeV del ^{12}Be , sin embargo es imposible confirmarlo con los detectores de este experimento. El error de las posiciones energéticas de las resonancias están calculados por suma cuadrática de los errores estadísticos de los ajustes y el error sistemático, como se explica en el apéndice A.

C.6 Conclusiones

- Este trabajo informa sobre varios posibles estados-resonancia del núcleo no-ligado ^{13}Be , confirmando algunos de los que habían sido medidos previamente: Uno a 0.28 MeV con momento angular orbital $l=0$ y otra resonancia con $l=2$ cerca de 2.15 MeV. También se ha encontrado un pico 0.95 MeV, este estado debe ser interpretado en coincidencia con la medida de rayos gamma. En la figura C.6 está la estructura propuesta del ^{13}Be . La figura C.5 y la tabla C.3 tiene el mejor ajuste al resultado propuesto, excepto para la tercera resonancia a 2.15 MeV cuyo valor está tomado de la tabla C.2 y la figura C.4(c).
- Esta es la primera vez que un experimento obtiene medidas de la estructura del núcleo no-ligado ^{13}Be utilizando una reacción $(p, 2p)$ bajo condiciones de dispersión cuasi-libre.
- Esta es la segunda vez que un experimento estudia ^{13}Be incluyendo medida de rayos gamma. Los resultados obtenidos son diferentes a los previos [33]. En nuestro trabajo, el rayo gamma de 2.1 MeV del ^{12}Be ha sido encontrado en coincidencia con un pico a ~ 0.95 MeV de la energía relativa del sistema

C.7. Desarrollos futuros

^{12}Be + neutrón. Por lo tanto, este pico es interpretado como una resonancia del ^{13}Be a 3.05 MeV con momento orbital de $1/2^+$ o $5/2^+$.

- La baja estadística y la ancha resolución de energía relativa, especialmente por encima de 3 MeV, ha hecho imposible extraer conclusiones más definitivas. A pesar de estos problemas, este trabajo ha sido capaz de confirmar resultados previos y proponer nuevas resonancias utilizando la reacción $^{14}\text{B}(p,2p)^{13}\text{Be}$.
- En este caso, no se ha encontrado necesario incluir el fondo no-resonante.

C.7 Desarrollos futuros

- La posición de la resonancia alrededor de 0.95 MeV en coincidencia con el rayo gamma de 2.1 MeV puede entenderse como una combinación de una resonancia a 0.95 MeV y otra a 2.1 MeV + 0.7 MeV \sim 2.8 MeV. El estado a 0.95 MeV (la línea discontinua de la figura C.6) sería $5/2^+$ tal y como ha sido establecido en otras publicaciones previas[43][46], mientras que el estado a 2.8 MeV podría ser $1/2$ o $5/2$. Esta posibilidad debería ser comprobada en otro experimento.
- Actualmente se están desarrollando mejoras en todas las partes del montaje experimental para la futura instalación FAIR. La medida de rayos-gamma será mejorada con el nuevo detector CALIFA. Los protones emitidos en la reacción serán detectados mucho más fácilmente utilizando el Silicon Tracker así como CALIFA, mejorando la eficiencia y la resolución energética. NeuLAND se ocupará de los neutrones y ayudará a mejorar la resolución angular, que es la mayor limitación para la determinación de la energía relativa. La combinación de todos estos detectores con haces radioactivos mucho más intensos facilitará la mejora de los resultados conseguidos.
- Además de la mejora en la resolución, eficiencia e intensidad del haz, que ya han sido planeadas, no hay información sobre la posibilidad de poblar el estado 0^+ isomérico del ^{12}Be a 2.24 MeV. Un experimento capaz de medir un estado de una vida media larga tras producir ^{13}Be contribuiría a conocer mejor este núcleo exótico.

C. Resumen en castellano

Bibliography

- [1] Udias Vallina, A. *Historia de la Fisica*. Editorial Sintesis (2004).
- [2] Rutherford, E. *Phil. Mag.*, **47**, 284, (1899), 109–163.
- [3] Rutherford, E. *Phil. Mag.*, **5**, 26, (1903), 177–187.
- [4] Rutherford, E. *Phil. Mag.*, **16**, (1908), 313–317.
- [5] Magill, J., Pfenning, G., Dreher, R., and Soti, Z. *Chart of Nuclides*. Nucleonica GmbH (2012).
- [6] Geiger, H. and Marsden, E. *Phil. Mag.*, **25**, (1913), 604.
- [7] Symons, T. J. M., Viyogi, Y. P., Westfall, G. D., et al. *Observation of New Neutron-Rich Isotopes by Fragmentation of 205-MeV/Nucleon ^{40}Ar ions*. *Phys. Rev. Lett.*, **42**, 1, (1979), 40–43.
- [8] Westfall, G. D., Symons, T. J. M., Greiner, D. E., et al. *Production of Neutron-Rich Nuclides by Fragmentation of 212-MeV/u ^{48}Ca* . *Phys. Rev. Lett.*, **43**, 25, (1979), 1859–1862.
- [9] Thoennessen, M. *Reaching the limits of nuclear stability*. *Reports Prog. Phys.*, **67**, 7, (2004), 1187–1232. doi:10.1088/0034-4885/67/7/R04. URL <http://stacks.iop.org/0034-4885/67/i=7/a=R04?key=crossref.97cd88746048c7f282afda2cdd36205b>.
- [10] Jonson, B. *Light dripline nuclei*. *Phys. Rep.*, **389**, (2004), 1–59. doi:10.1016/j.physrep.2003.07.004. URL <http://linkinghub.elsevier.com/retrieve/pii/S0370157303003259>.

BIBLIOGRAPHY

- [11] Hansen, P. and Tostevin, J. *Direct Reactions with Exotic Nuclei*. *Annu. Rev. Nucl. Part. Sci.*, **53**, 1, (2003), 219–261. doi:10.1146/annurev.nucl.53.041002.110406. URL <http://www.annualreviews.org/doi/abs/10.1146/annurev.nucl.53.041002.110406>.
- [12] Mueller, A. C. and Sherrill, B. M. *Nuclei at the limits of particle stability*. *Annu. Rev. Nucl. Part. Sci.*, **43**, (1993), 529–583.
- [13] Simon, H. *Halo nuclei, stepping stones across the drip-lines*. *Phys. Scr.*, **T152**, 014024, (2013), 1–13. doi:10.1088/0031-8949/2013/T152/014024. URL <http://stacks.iop.org/1402-4896/2013/i=T152/a=014024?key=crossref.d92b55911899c8393bbcfe80e0798a8b>.
- [14] Thoennessen, M., Mosby, S., Badger, N., et al. *Observation of a low-lying neutron-unbound state in ^{19}C* . *Nucl. Phys. A*, **912**, (2013), 1–6. doi:10.1016/j.nuclphysa.2013.05.001. URL <http://linkinghub.elsevier.com/retrieve/pii/S0375947413005095>.
- [15] Wamers, F., Marganec, J., Aksouh, F., et al. *First observation of the unbound nucleus ^{15}Ne* . *Phys. Rev. Lett.*, **112**, 132502, (2014), 1–5. doi:10.1103/PhysRevLett.112.132502. URL <http://journals.aps.org/prl/abstract/10.1103/PhysRevLett.112.132502>.
- [16] Marganec, J., Wamers, F., Aksouh, F., et al. *Studies of continuum states in ^{16}Ne using three-body correlation techniques*. *Eur. Phys. J. A*, **51**, 1, (2015), 1–9. doi:10.1140/epja/i2015-15009-0. URL <http://link.springer.com/10.1140/epja/i2015-15009-0>.
- [17] Caesar, C., Simonis, J., Adachi, T., et al. *Beyond the neutron drip line: The unbound oxygen isotopes ^{25}O and ^{26}O* . *Phys. Rev. C*, **88**, 034313, (2013), 1–8. doi:10.1103/PhysRevC.88.034313. URL <http://link.aps.org/doi/10.1103/PhysRevC.88.034313>.
- [18] Hoffman, C. R., Baumann, T., Brown, J., et al. *Observation of a two-neutron cascade from a resonance in ^{24}O* . *Phys. Rev. C*, **83**, 031303, (2011), 1–5. doi:10.1103/PhysRevC.83.031303. URL <http://link.aps.org/doi/10.1103/PhysRevC.83.031303>.
- [19] Tanihata, I., Hamagaki, H., Hashimoto, O., et al. *Measurements of interaction cross sections and radii of He isotopes*. *Phys. Lett. B*, **160**, 6, (1985), 380–384. doi:10.1016/0370-2693(85)90005-X.
- [20] Tanihata, I., Hamagaki, H., Hashimoto, O., et al. *Measurements of Interaction Cross Sections and Nuclear Radii in the Light p-Shell Region*. *Phys. Rev. Lett.*, **55**, 24, (1985), 2676–2679.

BIBLIOGRAPHY

- [21] Tanihata, I., Kobayashi, T., Yamakawa, O., et al. *Measurement of Interaction Cross Sections using isotope beams of Be and B and isospin dependence of the nuclear radii.* Phys. Lett. B, **206**, 4, (1988), 4–8.
- [22] Aumann, T. *Reactions with fast radioactive beams of neutron-rich nuclei.* Eur. Phys. J. A, **26**, 3, (2005), 441–478. doi:10.1140/epja/i2005-10173-4. URL <http://www.springerlink.com/index/10.1140/epja/i2005-10173-4>.
- [23] Hansen, P. and Jonson, B. *The Neutron Halo of Extremely Neutron-Rich Nuclei.* Europhys. Lett., pages 409–414.
- [24] Riisager, K. *Halos and related structures.* Phys. Scr., **T152**, 014001, (2013), 1–13. doi:10.1088/0031-8949/2013/T152/014001. URL <http://stacks.iop.org/1402-4896/2013/i=T152/a=014001?key=crossref.500f83ab0f70260a97dfff273b9462b7>.
- [25] Zhukov, M., Danilin, B., Fedorov, D., et al. *Bound state properties of Borromean halo nuclei: ${}^6\text{He}$ and ${}^{11}\text{Li}$.* Phys. Rep., **231**, 4, (1993), 151–199. doi:10.1016/0370-1573(93)90141-Y.
- [26] Group, I. T. W. Pure Appl. Chem., **83**, (1991), 879.
- [27] Williams, J. H., Shepherd, W. G., and Haxby, R. O. *Evidence for the instability of ${}^5\text{He}$.* Physical Review, **51**, (1937), 888–889. doi:<http://dx.doi.org/10.1103/PhysRev.51.888>.
- [28] Haddock, R. P., Salter, R. M., Zeller, M., Czirr, J. B., and Nygren, D. R. *Measurement of the neutron-neutron s-wave scattering length from the reaction $\pi^- + d \rightarrow 2n + \gamma$.* Physical Review Letters, **14**, (1965), 318–323. doi:<http://dx.doi.org/10.1103/PhysRevLett.14.318>.
- [29] Tanihata, I., Savajols, H., and Kanungo, R. *Recent experimental progress in nuclear halo structure studies.* Prog. Part. Nucl. Phys., **68**, (2013), 215–313. doi:10.1016/j.pnpnp.2012.07.001. URL <http://dx.doi.org/10.1016/j.pnpnp.2012.07.001>.
- [30] Baumann, T., Spyrou, A., and Thoennessen, M. Reports Prog. Phys., , 036301, , 1–21. doi:10.1088/0034-4885/75/3/036301.
- [31] Johansson, H. T., Aksyutina, Y., Aumann, T., et al. *The unbound isotopes ${}^9\text{--}{}^{10}\text{He}$.* Nuclear Physics A, **842**, 1-4, (2010), 15–32. doi:10.1016/j.nuclphysa.2010.04.006. URL <http://dx.doi.org/10.1016/j.nuclphysa.2010.04.006>.
- [32] Johansson, H., Aksyutina, Y., Aumann, T., et al. *Three-body correlations in the decay of ${}^{10}\text{He}$ and ${}^{13}\text{Li}$.* Nucl. Phys. A, **847**, 1-2, (2010), 66–88. doi:10.1016/j.nuclphysa.2010.07.002. URL <http://linkinghub.elsevier.com/retrieve/pii/S0375947410006044>.

BIBLIOGRAPHY

- [33] Kondo, Y., Nakamura, T., Satou, Y., et al. *Low-lying intruder state of the unbound nucleus ^{13}Be* . Phys. Lett. B, **690**, (2010), 245–249. doi:10.1016/j.physletb.2010.05.031. URL <http://linkinghub.elsevier.com/retrieve/pii/S0370269310006234>.
- [34] Aleksandrov, D. V., Ganza, E. A., Glukhov, Y. A., et al. *Observation ^{13}Be in the reaction $^{14}\text{C}(^7\text{Li},^8\text{B})$* . Sov. J. Nucl. Phys., **37**, (1983), 474–475.
- [35] Ostrowski, A. N., Bohlen, H. G., Demyanova, A. S., et al. *Mass spectroscopy of ^{13}Be* . Zeitschrift für Phys. A, **343**, (1992), 489–490.
- [36] Korshennikov, A., Nikolskii, E., Kobayashi, T., et al. *Spectroscopy of ^{12}Be and ^{13}Be using a ^{12}Be radioactive beam*. Physics Letters B, **343**, (1995), 53–58. doi:10.1016/0370-2693(94)01435-F.
- [37] von Oertzen, W., Bohlen, H., Gebauer, B., et al. *Nuclear structure studies of very neutron-rich isotopes of ^{7-10}He , ^{9-11}Li and $^{12-14}\text{Be}$ via two-body reactions*. Nuclear Physics A, **588**, (1995), 129c–134c. doi:10.1016/0375-9474(95)00111-D.
- [38] Belozyorov, A. V., Kalpakchieva, R., Penionzhkevich, Y. E., et al. *Spectroscopy of ^{13}Be* . Nucl. Phys. A, **636**, (1998), 419–426.
- [39] Thoennessen, M., Yokoyama, S., and Hansen, P. *First evidence for low lying s-wave strength in ^{13}Be* . Phys. Rev. C, **63**, 014308, (2000), 1–3. doi:10.1103/PhysRevC.63.014308. URL <http://link.aps.org/doi/10.1103/PhysRevC.63.014308>.
- [40] Simon, H., Aumann, T., Borge, M., et al. *Two- and three-body correlations: breakup of halo nuclei*. Nuclear Physics A, **734**, (2004), 323–326. doi:10.1016/j.nuclphysa.2004.01.058.
- [41] Lecouey, J. L. *Experimental Studies of Unbound Neutron-Rich Nuclei*. Few-Body-Systems, **34**, (2004), 21–26. doi:10.1007/s00601-004-0029-3. URL <http://link.springer.com/10.1007/s00601-004-0029-3>.
- [42] Simon, H., Meister, M., Aumann, T., et al. *Systematic investigation of the drip-line nuclei ^{11}Li and ^{14}Be and their unbound subsystems ^{10}Li and ^{13}Be* . Nucl. Phys. A, **791**, (2007), 267–302. doi:10.1016/j.nuclphysa.2007.04.021. URL <http://linkinghub.elsevier.com/retrieve/pii/S037594740700509X>.
- [43] Aksyutina, Y., Aumann, T., Boretzky, K., et al. *Structure of the unbound nucleus ^{13}Be : One-neutron knockout reaction data from ^{14}Be analyzed in a holistic approach*. Phys. Rev. C, **87**, 064316, (2013), 1–12. doi:10.1103/PhysRevC.87.064316. URL <http://link.aps.org/doi/10.1103/PhysRevC.87.064316>.

BIBLIOGRAPHY

- [44] Guimaraes, V., Kolata, J. J., Bazin, D., et al. *Spectroscopy of ^{13}B , ^{14}B via the one-neutron knockout reaction*. *Physical Review C*, **61**, 064609, (2000), 1–7. doi:10.1103/PhysRevC.61.064609. URL <http://arxiv.org/abs/nucl-ex/0001010>.
- [45] Aksyutina, Y., Aumann, T., Boretzky, K., et al. *Momentum profile analysis in one-neutron knockout from Borromean nuclei*. *Phys. Lett. B*, **718**, (2013), 1309–1313. doi:10.1016/j.physletb.2012.12.028. URL <http://linkinghub.elsevier.com/retrieve/pii/S0370269312012816>.
- [46] Randisi, G., Leprince, A., Al Falou, H., et al. *Structure of ^{13}Be probed via secondary-beam reactions*. *Phys. Rev. C*, **89**, 034320, (2014), 1–13. doi:10.1103/PhysRevC.89.034320. URL <http://link.aps.org/doi/10.1103/PhysRevC.89.034320>.
- [47] Bertulani, C. A. *Nuclear Physics in a Nutshell*. Princeton University Press (2007).
- [48] Satchler, G. R. *Introduction to Nuclear Reactions*. The Macmillan press LTD (1980).
- [49] Wamers, F. *Quasi-free-scattering and one-proton-removal reactions with the proton-dripline nucleus ^{17}Ne at relativistic beam energies*. Ph.D. thesis, Technische Universität Darmstadt (2011).
- [50] Panin, V. *Fully exclusive measurements of quasi-free single-nucleon knockout reactions in inverse kinematics*. Ph.D. thesis, Technische Universität Darmstadt (2012).
- [51] Holl, M. *Quasi-free scattering from relativistic neutron-deficient carbon isotopes*. Ph.D. thesis, Technische Universität Darmstadt (2014).
- [52] Díaz, P. *An investigation into quasi-free scattering of light neutron-rich nuclei around $N = 14$* . Ph.D. thesis, Universidade de Santiago de Compostela (2013).
- [53] Aumann, T., Bertulani, C., and Ryckebusch, J. *Quasifree $(p,2p)$ and (p,pn) reactions with unstable nuclei*. *Phys. Rev. C*, **88**, 064610, (2013), 1–15. doi:10.1103/PhysRevC.88.064610. URL <http://link.aps.org/doi/10.1103/PhysRevC.88.064610>.
- [54] R3B Collaboration, GSI. *S393 Experimental Proposal* (2010).
- [55] *S393 Experiment Elog*. URL <https://elog.gsi.de/S393/>.
- [56] *Exp. Analysis Elog*. URL <https://elog.gsi.de/r3b-analysis/>.
- [57] *GSI Facility Webpage*. URL <https://www.gsi.de/en.htm/>.

BIBLIOGRAPHY

- [58] Barth, W., Bayer, W., Dahl, L., et al. *Upgrade program of the high current heavy ion UNILAC as an injector for FAIR*. Nucl. Instruments Methods Phys. Res. Sect. A Accel. Spectrometers, Detect. Assoc. Equip., **577**, 1-2, (2007), 211–214. doi:10.1016/j.nima.2007.02.054. URL <http://linkinghub.elsevier.com/retrieve/pii/S0168900207003518>.
- [59] Geissel, H., Armbruster, P., Behr, K. H., et al. *The GSI projectile fragment separator (FRS): a versatile magnetic system for relativistic heavy ions*. Nucl. Instruments Methods Phys. Res. Sect. B Beam Interact. with Mater. Atoms, **70**, (1992), 286–2897.
- [60] GSI. *Relativistic beams on exotic nuclei: A powerful tool for nuclear structure physics*. GSI-Nachrichten, pages 13–16 (1997).
- [61] Altstadt, S. $^{13,14}\text{B} (n,\gamma)$ via coulomb dissociation to constrain the astrophysical r -process. Ph.D. thesis, Goethe Universität Frankfurt (2014).
- [62] Thies, R. *Prototype tests and pilot experiments for the R3B scintillator-based detection systems*. Master Thesis, Chalmers University of Technology (2011).
- [63] Mahata, K., Johansson, H., Paschalis, S., Simon, H., and Aumann, T. *Position reconstruction in large-area scintillating fibre detectors*. Nucl. Instruments Methods Phys. Res. Sect. A Accel. Spectrometers, Detect. Assoc. Equip., **608**, 2, (2009), 331–335. doi:10.1016/j.nima.2009.07.012. URL <http://linkinghub.elsevier.com/retrieve/pii/S0168900209014296>.
- [64] Johansson, H. T. *Hunting tools beyond the driplines, performing large-scale nuclear physics experiments*. Ph.D. thesis, Chalmers University of Technology (2010).
- [65] Blaich, T., Elze, T., Emling, H., et al. *A large area detector for high-energy neutrons*. Nucl. Instruments Methods Phys. Res. Sect. A Accel. Spectrometers, Detect. Assoc. Equip., **314**, 1, (1992), 136–154. doi:10.1016/0168-9002(92)90507-Z. URL <http://linkinghub.elsevier.com/retrieve/pii/016890029290507Z>.
- [66] GSI MBS Webpage. URL https://www.gsi.de/work/organisation/wissenschaftlich_technologische_abteilungen/experiment_elektronik/datenverarbeitung/datenerfassung/mbs.htm/.
- [67] Plag, R. and Johansson, H. T. *Land02 the unofficial guide*. URL <http://www-linux.gsi.de/~rplag/land02/>.
- [68] ROOT official Webpage. URL <http://root.cern.ch/>.
- [69] Rossi, D. M. *Investigation of the dipole response of nickel isotopes in the presence of a high-frequency electromagnetic field*. Ph.D. thesis, Johannes Gutenberg-Universität Mainz (2009).

BIBLIOGRAPHY

- [70] Paschalis, S. *Relativistic one-nucleon removal reactions*. Ph.D. thesis, University of Liverpool (2008).
- [71] *ATIMA Webpage*. URL <https://web-docs.gsi.de/~weick/atima/>.
- [72] *SHARP Calculator Webpage*. URL <http://www-w2k.gsi.de/frs-setup/Sharp%20Calculator.htm>.
- [73] Ribeiro Jiménez, G. *Exotic Nuclei and the neutron-dripline limits: S393 Experiment for the R3B collaboration and energy calibration of Crystal Ball*. Master Thesis, Universidad Complutense de Madrid (2011).
- [74] Lindeberg, S. *Optimised Use of Detector Systems for Relativistic Radioactive Beams*. Master Thesis in Fundamental Physics, Chalmers University of Technology (2013).
- [75] Thies, R. *Across the drip-line and back: examining ^{16}B* . Thesis for Licentiate of Engineering, Chalmers University of Technology (2014).
- [76] Plag, R. *Some documentation on Ralf's tracker*. URL <http://ralfplag.de/tracker/>.
- [77] Heine, M. *Measurement of (n, γ) -rates of light neutron-rich nuclei for the r-process nucleosynthesis*. Ph.D. thesis, Technische Universität Darmstadt (2014).
- [78] *National Nuclear Data Center Webpage*. URL <http://www.nndc.bnl.gov/>.
- [79] Caesar, C. *Beyond the neutron drip-line: Superheavy oxygen isotopes*. Ph.D. thesis, Technische Universität Darmstadt (2012).
- [80] Landau, L. D. and Lifshitz, E. M. *The Classical Theory of Fields*. Spanish Edition, Editorial Reverté (1981).
- [81] Lane, A. and Thomas, R. *R-Matrix Theory of Nuclear Reactions*. *Rev. Mod. Phys.*, **30**, 2, (1958), 257. doi:10.1103/RevModPhys.30.257.
- [82] Bohr, A. and Mottelson, B. R. *Nuclear Structure vol 1: Single Particle Motion*. World Scientific Publishing (1969).
- [83] Shimoura, S., Saito, A., Minemura, T., et al. *Isomeric 0^+ state in ^{12}Be* . *Phys. Lett. B*, **560**, 1-2, (2003), 31–36. doi:10.1016/S0370-2693(03)00341-1. URL <http://linkinghub.elsevier.com/retrieve/pii/S0370269303003411>.
- [84] Johansen, J. G., Bildstein, V., Borge, M. J. G., et al. *Experimental study of bound states in ^{12}Be through low-energy $^{11}\text{Be}(d,p)$ -transfer reactions*. *Phys. Rev. C*, **88**, 044619, (2013), 1–10. doi:10.1103/PhysRevC.88.044619. URL <http://link.aps.org/doi/10.1103/PhysRevC.88.044619>.

BIBLIOGRAPHY

- [85] Shimoura, S., Ota, S., Demichi, K., et al. *Lifetime of the isomeric 0^+ state in ^{12}Be* . Phys. Lett. B, **654**, 3-4, (2007), 87–91. doi:10.1016/j.physletb.2007.08.053. URL <http://linkinghub.elsevier.com/retrieve/pii/S0370269307010131>.
- [86] CERN Minuit Homepage. URL <http://seal.web.cern.ch/seal/snapshot/work-packages/mathlibs/minuit/>.
- [87] Sauvan, E., Carstoiu, F., Orr, N. a., et al. *One-neutron removal reactions on light neutron-rich nuclei*. Phys. Rev. C - Nucl. Phys., **69**, 044603, (2004), 18–25. doi:10.1103/PhysRevC.69.044603.
- [88] Bedoor, S., Wuosmaa, a. H., Lighthall, J. C., et al. *Structure of ^{14}B and the evolution of $N=9$ single-neutron isotones*. Phys. Rev. C - Nucl. Phys., **88**, 011304, (2013), 1–5. doi:10.1103/PhysRevC.88.011304.
- [89] Fortune, H. T. *$^{14}\text{Be}(g.s.)$ and single-particle energies in ^{13}Be* . Phys. Rev. C, **90**, 064305, (2014), 1–2. doi:10.1103/PhysRevC.90.064305. URL <http://link.aps.org/doi/10.1103/PhysRevC.90.064305>.
- [90] Fortune, H. T. *Unraveling the structure of ^{13}Be* . Phys. Rev. C, **87**, 014305, (2013), 1–4. doi:10.1103/PhysRevC.87.014305. URL <http://link.aps.org/doi/10.1103/PhysRevC.87.014305>.